

Experimental Studies of a Small Scale Horizontal Axis Tidal Turbine

by

Italo Franchini

B.Sc., Catholic University of Chile, 2012

A Thesis Submitted in Partial Fulfillment of the
Requirements for the Degree of

MASTER OF APPLIED SCIENCES

in the Department of Mechanical Engineering



© Italo Franchini, 2016
University of Victoria

All rights reserved. This dissertation may not be reproduced in whole or in part, by photocopying or other means, without the permission of the author.

Experimental Studies of a Small Scale Horizontal Axis Tidal Turbine

by

Italo Franchini

B.Sc., Catholic University of Chile, 2012

Supervisory Committee

Dr. Curran Crawford, Supervisor
(Department of Mechanical Engineering)

Dr. Brad Buckham, Departmental Member
(Department of Same As Candidate)

Dr. Sue Molloy, Outside Member
(Department of Mechanical Engineering, Dalhousie University)

Supervisory Committee

Dr. Curran Crawford, Supervisor
(Department of Mechanical Engineering)

Dr. Brad Buckham, Departmental Member
(Department of Same As Candidate)

Dr. Sue Molloy, Outside Member
(Department of Mechanical Engineering, Dalhousie University)

ABSTRACT

The research in this thesis focuses on the investigation of tidal turbines using a small scale horizontal axis tidal turbine and a 2D hydrofoil testing rig, combining experiments with simulations to provide comprehensive results and to better understand some of the variables that affect their performance. The experimental campaigns were carried out at the University of Victoria fluids research lab and the Sustainable Systems Design Lab (SSDL). The experimental testing rigs were re-designed by the author and are now fully automated, including a friendly graphical user interface for easy implementation. Particle image velocimetry (PIV) technique was used as the quantitative flow visualization method to obtain the time-averaged flow fields.

This thesis presents three investigations. The first study aims to quantify the impacts of channel blockage, free surface effects and foundations on hydrokinetic turbine performance, using porous discs and an axial flow rotor. The results were used to cross-validate computational fluid dynamics (CFD) simulations. It was found that as wall blockage increases, thrust and power are incremented with and without the inclusion of free surface deformation. Discrepancies between simulations and experimental results on free surface effects compared to a slip wall were obtained and hence further research is recommended and the author gives some advice on how to proceed in this investigation.

The second study determines the performance of four hydrofoil candidates over a range of low Reynolds number (Re), delivering useful information that can be applied to low Re energy conversion systems and, specifically in this case, to improve

the performance of the small scale tidal turbine at the SSDL lab. The study combines the 2D hydrofoil test rig along with PIV measurements in order to experimentally obtain lift and drag coefficients. The experiments were carried out in the recirculating flume tank over the range of low Re expected for the small scale rotor rig, in order to provide more accurate results to improve rotor blade design. In addition, numerical simulations using XFOIL, a viscid-inviscid coupled method, were introduced to the study. These results were analysed against experiments to find the most suitable parameters for reliable performance prediction. The final results suggested that adding a numerical trip at a certain chordwise distance produced more reliable results.

Finally, an experimental study on turbine rotor performance and tip vortex behavior was performed using again the rotor rig and PIV. Blade design and rotor performance were assessed, showing good agreement with Blade Element Momentum (BEM) simulations, particularly at predicting the tip speed ratio corresponding to the maximum power coefficient point. Regarding the wake structure, tip vortex locations (shed from the blade tips) were captured using PIV in the near wake region, showing evidence of wake expansion. The velocity and vorticity fields are also provided to contribute to the development and validation of CFD and potential flow codes.

Contents

Supervisory Committee	ii
Abstract	iii
Table of Contents	v
List of Tables	viii
List of Figures	ix
Nomenclature	xiii
Acknowledgements	xv
Dedication	xvi
1 Introduction	1
1.1 Horizontal Axis Tidal Turbines	2
1.2 Additional Concerns in Tidal Power Extraction	4
1.3 Key Contributions	5
1.4 Thesis Outline	6
2 Impact of channel blockage, free surface proximity and foundations on the performance of tidal and river energy converters	7
2.1 Abstract	7
2.2 Introduction	8
2.3 Experimental Method	9
2.3.1 Closed top experiments	10
2.3.2 False top experiments	13
2.3.3 Open flume experiments	13

2.3.4	Experimental Error	14
2.3.5	Experimental Results	15
2.4	CFD Simulations of Porous Disc	15
2.4.1	Porous Disc Model	15
2.4.2	Influence of Rotor Scale	18
2.4.3	Model Boundary Conditions	20
2.4.4	Simulation Matrix	22
2.4.5	Impact of Modeling the Free-Surface on Channel Blockage	22
2.4.6	Impact of Foundations on Channel Blockage with Inclusion of Free Surface	23
2.5	CFD Simulations of an Axial Flow Rotor	25
2.5.1	Background and preparation	27
2.5.2	CFD Set-up	29
2.5.3	CFD Rotor Simulation Results	31
2.6	Comparison of Experiments to CFD Simulations	38
2.6.1	Porous Disc vs CFD	38
2.6.2	Axial Rotor Experiments vs CFD	41
2.6.3	Porous Disc vs Axial Rotor	43
2.7	Conclusions	45
3	PIV/Flume-Tank Experimental Study of 2D Hydrofoil Coefficients at Low Re	47
3.1	Abstract	47
3.2	Introduction	48
3.3	Candidate Foils	50
3.4	XF0IL and Optimization method	50
3.5	Experimental Method	54
3.5.1	FDM Airfoil Fabrication	55
3.5.2	Water tunnel	55
3.5.3	2D Airfoil Test Rig	56
3.5.4	PIV Setup	57
3.5.5	Data Reduction Method	58
3.5.6	Predictions Considerations	61
3.6	Results and Discussion	62
3.6.1	NACA 2415 SSDL vs UIUC	62

3.6.2	NACA 2415 and SD8020 15% XFoil Predictions	65
3.6.3	SSDL Hydrofoil performance	67
3.7	Conclusions	72
4	An experimental study of small scale horizontal axis turbine rotor performance and tip vortex behavior	73
4.1	Abstract	73
4.2	Introduction	74
4.3	Axial Rotor Rig	75
4.4	Blade Design	76
4.5	Experimental Method	80
4.5.1	Water tunnel	80
4.5.2	Particle Image Velocimetry	82
4.5.3	Blade Performance	82
4.5.4	Wake structure	84
4.6	Results and Discussion	85
4.6.1	Rotor Performance	85
4.6.2	Near-and-Far Wake Regions	87
4.7	Conclusions	93
5	Conclusions	94
5.1	Future Work	95
A	Appendices	103
A.1	Rotor rig modifications	103
A.2	Instrumentation Modifications	103

List of Tables

Table 2.1	Froude numbers of potential Canadian turbine sites	21
Table 2.2	Froude numbers of free surface CFD simulations	21
Table 2.3	Investigation into free surface effects	22
Table 2.4	Investigation into influence of foundations	22
Table 2.5	Axial rotor CFD simulation matrix, where the inlet velocity $U_\infty = 1.261$ m/s and tank width=0.45 m were kept constant throughout the simulations	31
Table 2.6	Peak performance values based on steady state simulation results	35
Table 2.7	Peak performance values based on transient simulation results	35
Table 2.8	Comparison of C_T and C_P for a 21.9 cm rotor and disc	44
Table 2.9	Comparison of C_T and C_P for a 21.9 cm rotor and disc on a percentage change basis	44
Table 3.1	Objective function evaluation between selected hydrofoils	67

List of Figures

Figure 1.1	Caption for LOF	3
Figure 2.1	Porous Discs	10
Figure 2.2	Location of the porous disc in the flume tank	11
Figure 2.3	Schematic of the testing rig(left) and physical rig(right)	12
Figure 2.4	Height measurement points along the flume.	14
Figure 2.5	C_T obtained for both porous discs under a range of inflow speeds	16
Figure 2.6	C_T for the 3 Blockage ratios using disc with $\phi = 150$ mm	17
Figure 2.7	CFD Validation of Porous Disc Model, showing the comparison of $\% \Delta C_T$ (top) and $\% \Delta C_P$ (bottom) between UVic, Clean Current and MAVI results	19
Figure 2.8	CFD model with inclusion of free surface	20
Figure 2.9	CFD results between Slip-Wall and free-surface simulations, showing the impact on C_T (top) and C_P (bottom) when simulation settings are kept constant, irrespective of BR	24
Figure 2.10	CFD results showing water elevation contour plots at three different BR, for free-surface simulation cases	25
Figure 2.11	CFD results between Slip-Wall and free-surface simulations, showing the impact on C_T (top) and C_P (bottom) when simulation settings are tuned to operate at MPP	26
Figure 2.12	Porous disc model with monopole foundation	27
Figure 2.13	Use of gravity foundations for porous disc model	27
Figure 2.14	Impact of foundations on blockage effects	28
Figure 2.15	CFD model of rotor and foundations	29
Figure 2.16	Top: Side view of the turbine in the virtual flume tank. Flow is from left to right. Bottom: Frontal view for BR = 18.6%, 11.6% and 8.7%. Cylindrical region around the blade corresponds to the rotational domain.	29

Figure 2.17	Mesh topologies for CFD simulations	30
Figure 2.18	CFD model with applied boundary conditions: Single arrows indicate the normal inlet velocity, whereas double arrows show the opening boundary condition at the outlet of the domain	31
Figure 2.19	$y+$ values on the blades. Left: Upstream (high pressure) side. Right: Downstream (low pressure) side.	32
Figure 2.20	Steady-state (SS) and Transient (T) results showing the effect of BR on λ for C_T and C_Q	33
Figure 2.21	Steady-state (SS) and Transient (T) results showing the effect of BR on λ for C_P and VR.	34
Figure 2.22	Effect on BR on relative λ and VR at peak performance point	36
Figure 2.23	Effect on BR on relative C_Q , C_T and VR^2 at peak performance point	37
Figure 2.24	Effect on BR on relative C_P and VR^3 at peak performance point	38
Figure 2.25	Comparison between CFD and experiments showing the free surface deformation for (a) BR=8.7%, (b) BR=11.6% and (c) BR=17.5%	40
Figure 2.26	Comparison of experiments and porous disc CFD results, showing how the C_T varies with increasing blockage, for slip wall (top) and free surface (bottom) cases	41
Figure 2.27	Experimental and CFD results for axial rotor	43
Figure 3.1	Final airfoil selection	51
Figure 3.2	SD8020 airfoil data taken from UIUC	52
Figure 3.3	NACA2415 airfoil data taken from UIUC	53
Figure 3.4	Optimized airfoil shapes	54
Figure 3.5	2D Airfoil Test Rig as viewed from upstream	56
Figure 3.6	Laser double sheet for PIV	58
Figure 3.7	5-point stencil	60
Figure 3.8	Example of a post-processed PIV result showing the time-averaged velocity field (a) and the obtained pressure field (b) for the NACA2415-SSDL at $\alpha = 10^\circ$	63
Figure 3.9	NACA2415 PIV v/s UIUC results	64

Figure 3.10	Sensitivity analysis of NACA2415 XF0IL predictions using $N_{crit} = 9$ for a range of x_{tr}	66
Figure 3.11	Sensitivity analysis of SD8020 15tk XF0IL predictions using $N_{crit} = 9$ for a range of x_{tr}	69
Figure 3.12	Final results for NACA 2415 and NACA 2415-SSDL for $Re=6 \times 10^4$	70
Figure 3.13	Final results for SD8020 15% and SD8020-SSDL for $Re=6 \times 10^4$	71
Figure 4.1	Rotor rig final design	76
Figure 4.2	SD8020 hydrofoil	77
Figure 4.3	BEM results showing the blade parameter distribution to be used for the final design	78
Figure 4.4	Blade set Re operational range	79
Figure 4.5	Final blade design	80
Figure 4.6	Rotor rig sketch inside flume tank showing principal dimensions	81
Figure 4.7	Blade deflection FEM analysis (left) and Experimental result (right). The maximum experimental deflection was found to be $\delta_{max} = 1.2 \text{ mm}$	86
Figure 4.8	Rotor performance over a range of inflow speeds for BR=19.7%	87
Figure 4.9	Rotor performance for $U_{\infty} = 1.233 \text{ m/s}$, showing the bounded, unbounded (corrected) and BEM predictions.	88
Figure 4.10	Contours of axial velocity at the blade tip when $\varphi = 0^{\circ}$ (top) and a phase-locked average of the wake considering all the azimuth planes (bottom)	89
Figure 4.11	Vortical structures shed from the blade tip in the near wake at maximum power performance, showing contours of non-dimensional tangential vorticity for azimuth planes of $\varphi = 0^{\circ}$ (top), $\varphi = 40^{\circ}$ (middle) and $\varphi = 80^{\circ}$ (bottom)	90
Figure 4.12	Vortical structures shed from the blade tip in the near wake, showing contours of non-dimensional tangential vorticity for azimuth planes of $\varphi = 120^{\circ}$ (top), $\varphi = 160^{\circ}$ (middle) and $\varphi = 200^{\circ}$ (bottom)	90

Figure 4.13	Vortical structures shed from the blade tip in the near wake, showing contours of non-dimensional tangential vorticity for azimuth planes of $\varphi = 240^\circ$ (top), $\varphi = 280^\circ$ (middle) and $\varphi = 320^\circ$ (bottom)	91
Figure 4.14	Tip vortex behind near wake region	92
Figure 4.15	Normalized velocity field showing the wake development for the entire test section. The rotor plane and sting have been masked out.	93
Figure A.1	Top assembly modifications. Original design (left) and new design (right)	104
Figure A.2	Hub modifications. Original design (left) and new stainless steel welded hub design (right)	104
Figure A.3	Original axial rotor design (left) and full rotor rig new appearance (right)	105
Figure A.4	Original 2D Hydrofoil test rig (left) and new design (right)	105
Figure A.5	New instrumentation panel appearance	105
Figure A.6	Rotor rig control interface developed in LabView 2012	106
Figure A.7	2D Hydrofoil test rig control interface developed in LabView 2012	106

Nomenclature

Acronyms

BR	Blockage Ratio
CFD	Computational Fluid Dynamics
CO ₂	Carbon Dioxide
FDM	Fused Deposition Modeling
HATT	Horizontal Axis Tidal Turbine
LMADT	Linear Momentum Actuator Disc Theory
MPP	Maximum Power Point
RANS	Reynolds-Averaged Navier Stokes
SSDL	Sustainable Systems Design Lab
UVic	University of Victoria

Symbols

Δp	Pressure difference
λ	Tip speed ratio
μ	Dynamic viscosity
ω	Rotational speed
$\overline{u_{x-disc}}$	x -direction velocity averaged over volume of disc
ϕ	Diameter
ρ	Water density
A_{disc}	Cross sectional area of the porous disc
C_P	Power coefficient
C_Q	Torque coefficient
C_T	Thrust coefficient
$C_{P,calculated}$	Calculated power coefficient
$C_{P,inf. channel}$	Theoretical maximum power coefficient
$C_{T,calculated}$	Calculated thrust coefficient

$C_{T,inf. channel}$	Theoretical maximum thrust coefficient
Fr	Froude number
g	Gravitational acceleration
h	Water tunnel depth
$k - \omega$	Turbulence model
P	Power
R	Rotor radius
R	Torque
T	Experimental disc thrust force
U_∞	Free-stream velocity
v	Velocity through the disc
y^+	Non-dimensional wall distance
Re	Reynolds number
VR	Velocity ratio

ACKNOWLEDGEMENTS

I would like to sincerely thank *Dr. Curran Crawford*, who helped me and believed in my work in a very difficult and challenging moment of my life, for being a constant support and for his outstanding knowledge on the field. I would like to extend my gratitude to *Michael Shives*, *Rodney Katz* and *Mostafa Rahimpour*, who became essential in the completion of this research.

In addition, I would like to mention my sister *Francisca*, *my family* and *friends*, who provided me with me constant strength, support and unconditional love.

DEDICATION

Para mi hijo Diego: Eres la razón de mi felicidad!.

Chapter 1

Introduction

There is undeniable scientific evidence [1]–[3] that the Earth’s climate system is warming at rates unseen over tens of thousands of years. The human-made carbon dioxide (CO₂) being released into the atmosphere has increased the greenhouse effects, leading to a sustained rise of the global mean surface temperature. The excess of CO₂ comes mainly from the burning of fossil fuels, which have been drastically increasing since the beginning of the industrial revolution. Recently, the 2015 United Nations Climate Change Conference (COP21) negotiated the Paris Agreement between 195 countries, which contemplates a first-ever global action plan to avoid climate change by limiting global warming to well below 2°C.

It is in this context where renewable energies have grown at rates faster than any other time in history. Amongst the available options, tidal power is starting to make its way into the energy market due to many recent technological developments and improvements. The main advantages of tidal energy, e.g. over solar and wind power generation, is the high predictability of this resource and high energy density. Tidal current is independent of weather conditions, such as rain, clouds and wind, and is only governed by the gravitational pull of the moon (principally) and the sun on the Earth’s oceans. The most frequent form of tidal energy extraction is using tidal barrages, which have a detrimental environmental impact, affecting the nearby marine life and increasing silt deposits in the basin. In addition, the high speed operational range of the turbines can kill wildlife that passes through them [4], [5]. These limitations promoted the research of kinetic energy extraction devices, which attempt to harness the available kinetic energy stored in tidal flows for energy generation. Kinetic turbines are the leading technology in this field, which basically operate according to similar principles to conventional wind turbines. However, in-

trinsic differences between fluid properties and deployment sites must be taken into account with comprehensive studies and experimental work in order to improve both design and validation tools.

The present study is focused on experimental research regarding Horizontal Axis Tidal Turbines (HATTs), described in section 1.1, using a small-scale version designed at the Sustainable Systems Design Lab (SSDL). This paper-based thesis covers three investigations:

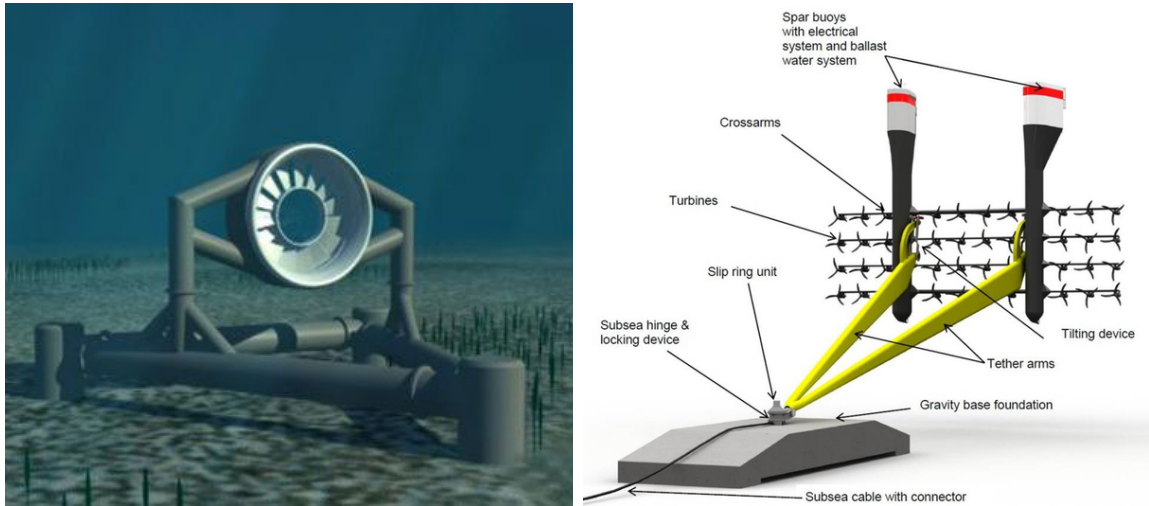
- Impact of Channel Blockage, Free Surface Proximity and Foundations on the Performance of Tidal and River Energy Converters (Chapter 2)
- PIV/Flume-Tank Experimental Study of 2D Hydrofoil Coefficients at Low Re (Chapter 3)
- Blade Design, Rotor Performance and Near-Wake Tip Vortex Analysis Using a Small-Scale Horizontal Axis Tidal Turbine (Chapter 4)

1.1 Horizontal Axis Tidal Turbines

The dominant design among tidal turbines corresponds to the axial flow turbines or HATTs, in which the flow direction is parallel to the turbine’s rotational axis. Years of wind turbines studies [6]–[9] have determined that horizontal axis turbines exhibit higher efficiency in extracting energy from the flow compared to cross-flow turbines. Most large-scale projects are, consequently, using HATTs as the dominant marine hydrokinetic turbine design.

The biggest tidal energy projects can be found today in the Bay of Fundy, Nova Scotia, specifically in Minas Passage. The creation of the Fundy Ocean Research Centre for Energy (FORCE) in 2009 rapidly boosted project developments in the area. Cape Sharp Tidal, an OpenHydro and Emera company, is about to deploy two 2 MW turbines, shown in figure 1.1a. These turbines have a unique open-centre design and will be mounted on the sea floor. Black Rock Tidal Power will be the next company to deploy another unique design concept, using a TRITON semi-submerged structure designed by TidalStream, as presented in figure 1.1b. It employs small tidal turbines made by Schottel Hydro and is expected to produce 2.5 MW of electrical power. Atlantis Resources will also test its AR1500 three-bladed tidal turbine, which has a rated capacity of 1.5 MW production at $U_\infty = 3$ m/s, as presented in figure

1.1c. The level of intrigue among the scientific community is high and the results will have a huge value to determine which designs show competitive advantages over the remaining ones.



(a) OpenHydro ducted design, expected to produce 2 MW (b) TRITON platform using Schottel Hydro turbines



(c) Three-bladed 1.5 MW Atlantis AR1500

Figure 1.1: Current tidal turbine designs to be tested at the Bay of Fundy, Nova Scotia ¹

¹Figures taken from capesharptidal.com, blackrocktidalpower.com and atlantisresourcesltd.com

1.2 Additional Concerns in Tidal Power Extraction

Although most of the theoretical background for tidal turbine analysis and design was adapted from wind turbines, there are important differences that directly impacts the power extracted by these devices.

Blockage effects play an important role when simulating/operating a turbine bounded by lateral walls, the ocean floor and water surface. The ratio of the rotor swept area to the channel sectional area defines the non-dimensional parameter to account for blockage effects on power performance. As wall blockage increases, the velocity around the rotor increments, modifying the maximum power extractable by the device. Glauert [10], Mikkelsen and Sorensen [11] and Bahaj *et. al* [12] developed correction methods to account for this wall blockage. Recently, Lártiga [13] followed up on this methods and presented a correlation that uses the axial induction factor instead of thrust measurements. This approach turns out to be very helpful given the current experimental setup available, since no thrust measurements are reliable on such a small scale.

Free surface effects can produce considerable differences in power extraction, as studied by Whelan *et. al* [14]. Free surface deformation due to an operating tidal turbine can affect both effective blockage ratio and wake characteristics, thus directly impacting on the final power output.

Due to the large number of novel designs, another important factor that arises relates to the *foundations* on which the turbines are installed. The choice for a specific foundation depends on several factors, going from environmental constraints (e.g. seabed type and water depth) to the high installation costs. Among the most common foundation types are the monopiles, gravity foundations, floating structures, tripods with buckets and suction buckets. The foundation type mainly affects the stability and performance of these devices

Cavitation can occur on tidal turbines, reducing the efficiency and damaging the rotor blades. Cavitation occurs when the static pressure of the water falls below the vapour pressure (p_v), causing bubbles that collapse at the back of the rotor's blade, where the low pressure region is located. However, with an appropriate hydrofoil selection, suitable design and turbine operation, this problem can be avoided, as studied by Batten *et. al* [15]. Unfortunately, the work in this thesis does not cover cavitation studies on hydrofoils.

Ecological impacts are certainly a key point to investigate in order to safely deploy new projects. The study presented by Frid *et. al* [16] reviewed the environmental impacts of tidal stream farms on surrounding habitat, noise, electromagnetic fields emissions from cables and turbulence generation.

1.3 Key Contributions

The different studies presented in this work are intended to contribute to improving design and simulation tools. Among the key points:

- Re-design of the small-scale rotor rig [17] and 2D airfoil test rig [18] for experimental campaigns. Complete automation, synchronization and graphical user interface of the mentioned devices to work with PIV, delivering very reliable and satisfactory performances.
- Experimental work studying the impact on channel blockage in turbines power performance, using both porous discs and an axial rotor rig. The results were complemented using simulation predictions performed by MAVI and Clean Current, showing good agreement with previous studies [12], [14], [19], [20].
- Investigation of free surface impacts on rotor performance, using porous discs and the rotor rig. The results showed discrepancies between experiments and CFD, mainly due to the simulation parameters considered. Nevertheless, this key contribution encourages better CFD methodology and points out the assumptions that explain this behaviour that need additional investigation.
- Improving the existing experimental instrumentation to obtain experimental 2D hydrofoil coefficients at low Reynolds numbers, using Marcangeli [21], Root [18] and Shives 3 data reduction method. The approach and results are equally applicable to air and water tunnels.
- Improve numerical hydrofoil predictions using open source code XFOIL [22] for data obtained at UVic's flume tank, obtaining reliable *-a priori-* foil performance.
- Customized blade design, combining the previous study from chapter 3 results with Blade Element Momentum code [23], obtaining great rotor performance that will allow several future experiments to be completed.

- Novel approach using the small scale tidal turbine to capture the tip vortex in the near-wake region, using different azimuth planes and PIV, confirming the wake expansion and vorticity field found in previous studies related to wind turbines [24]–[27]. No similar study was found regarding HATTs.

1.4 Thesis Outline

This research follows up on the work done by Catalina Lártiga [17], who initially designed and built the first version of the 3D rotor rig, and Peter Root [18], following up on his research to experimentally determine hydrodynamic performance of low Re hydrofoils. Important modifications were developed by the author in order to obtain a fully controllable system for experimental research, as detailed in appendix A.

The thesis is a collection of papers outlined as follows: Chapter 2 presents the first experimental campaign, aimed to quantify the impact of channel blockage, free surface effects and foundations on turbine performance. Computational simulations and experimental testing were used to cross-validate and help interpret the results. The second study is presented in chapter 3, where the goal was to experimentally determine the performance of four hydrofoils, obtained from literature and through optimization routines. Those results are then used to improve performance predictions using an viscid-inviscid coupled method [22], [28]. Chapter 4 summarizes the investigation using the 3D rotor rig, which involved blade design, rotor performance and near-and-far wake structure characterization. Finally, chapter 5 summarizes the conclusions obtained from the different studies and presents some suggestions for possible future work experiments.

Chapter 2

Impact of channel blockage, free surface proximity and foundations on the performance of tidal and river energy converters

Primary Author: Italo Franchini¹

Authors: Michael Shives¹, Curran Crawford¹, Voytek Klaptocz², Timothy Waung², Mete Sireli³

¹ Dept. of Mechanical Engineering, University of Victoria, BC

² MAVI Innovations Inc.

³ Clean Current Power Systems Inc.

To be submitted

The full version of this study can be found in [29]. The author of this thesis contributed with the experimental work related to this research.

2.1 Abstract

This project aimed to quantify the impact of channel blockage, free surface effects, and foundations on hydrokinetic turbine performance using both porous disc analogs and an axial flow rotor. A combination of computer simulations (CFD) and experimental testing in a flume tank at the University of Victoria was used to cross-validate

the work and help interpret the results. Both experiments and CFD simulations show an increase on thrust and power as blockage increases, with and without the inclusion of free surface effects. However, discrepancies in experimental and simulation results were found when the free surface effects are considered for the highest blockage scenario. In addition, CFD simulations showed that a turbine foundation can have a significant impact on turbine performance. Two foundations types were considered for this project: a streamlined monopole installed downstream of the rotor, and a heavier gravity type foundation placed in the plane of the rotor. The first foundation type had a negligible effect on power production while the second increased power production substantially. The impact of the turbine foundation was therefore shown to be directly coupled to the shape of the structure and its interaction with the turbine. Results from CFD simulations and experiments on an axial rotor were in good agreement in terms of predicting the peak power point. Overall, the CFD predicted higher overall performance values with the largest discrepancy occurring at tip speed ratios (λ) lower than the peak performance point. CFD simulations were subsequently used to derive performance values for a range of blockage ratios, since this was not possible with the current experimental set-up. These results showed that both thrust and power for the axial rotor were less affected by channel blockage compared to the porous disc or predictions made using actuator disc theory. This outcome leads to the conclusion that the increase in thrust and power derived using actuator disc theory (and porous discs) for increasingly constrained channels likely represents an upper bound for real rotors. The actual boost in power for a physical turbine placed in a blocked channel will vary depending on the turbine's design and foundation.

2.2 Introduction

To date, turbine performance studies [12], [14], [19], [20] have shown that channel blockage can have a substantial impact on turbine power output. Nishino and Willden [19], [30] completed a series of studies using 3D computational fluid dynamics (CFD) simulations to investigate the effect of Blockage Ratio (BR) on turbine power output. In their 2012 paper [19], 3D CFD simulations were run where turbines were modeled as porous discs, and both BR and aspect ratio were varied. The results from this study with CFD data compared to 1D linear momentum actuator disc theory (LMADT) show good agreement between the CFD simulations and LMADT.

Nashino and Willden published a second study [30] looking into the effect of channel blockage for turbine arrays. The turbine array consisted of multiple turbines positioned side by side along a line perpendicular to the flow direction. The parameters that were varied were overall channel blockage and the spacing between turbines. It was found that for low channel BRs there was an optimal spacing between turbines. For high channel BRs, however, it was found that the array power is maximized when the space between turbines is zero.

Most studies to date have focused on modeling a range of turbine BRs and array configurations, but have neglected the effect of the water free surface or turbine foundations. An analysis by Whelan *et al.* [14] did use a modified 1D actuator disc type analysis method to predict how the presence of the surface would affect turbine power output. Comparison of this model to experiments showed good agreement and concluded that the extractable turbine power is further increased when the turbine is placed in proximity of the water surface. Porous plates spanning the width of the channel were used for the experiments, while the CFD modeling was done in 2D.

A recent study published by Kolekar and Banerjee [20] investigated turbine performance in an open water channel under wall blockage. They varied the immersion depth and performed coupled experimental and computational studies, finding that the turbine performance increased as it was moved away from the channel bottom, until it reached approximately half radius distance below the free surface, after which a reduction in performance was observed.

The present study combines experiments with 3D modeling CFD using both porous discs and a small-scale horizontal axis tidal turbine (HATT) developed at the Sustainable Systems Design Lab (SSDL) [17]. Porous discs are tested at three different BR of 8.7%, 11.6% and 17.5%, using an open and closed flume, eliminating free surface effects. 3D modeling CFD served for simulating the turbines performance and comparing them with experiments using the HATT, which is tested for only one blockage ratio of 18.6%, given the available set-up. The goal is to compare how performance changes as BR increases and using those results to compare them with porous discs results.

2.3 Experimental Method

All experiments were completed in the Fluids Research Lab at the University of Victoria (UVic), using a flume tank with a cross section of 0.45 m \times 0.45 m and

measuring 2.5 m length. The top of the test section can be opened for tests involving a free surface (air-water surface), or can be closed off using acrylic lids. With the lids installed, the effects of free surface deformation are no longer present. The turbines were represented by porous discs for the first set of experiments. A separate three-bladed axial rotor was used in order to obtain a characteristic curve that describes the performance of the blades.

2.3.1 Closed top experiments

This set of experiments were carried out using the acrylic lids and the tank completely full to avoid free surface effects. The water level in the inflow ducting is actually set higher than the lid height to ensure complete filling of the test section while the tunnel is in operation.

Porous discs

It was first intended to study free surface effects and the impact on both Thrust coefficient (C_T) and water height along the flume. The porous discs were designed using the commercial CAD tool Solidworks and fabricated from polycarbonate using a Fused Deposition Modeling (FDM) machine, as shown in Figure 2.1. Two different discs diameters were printed, $\phi = 150 \text{ mm}$ and $\phi = 219 \text{ mm}$. The smaller disc was used for the experiments studying the effects of the free surface. The larger diameter disc was designed to match the axial rotor's diameter and to obtain C_T over a range of velocities to be used for CFD analysis. Both discs were built using 50% porosity and a regularly spaced grid of square pores.

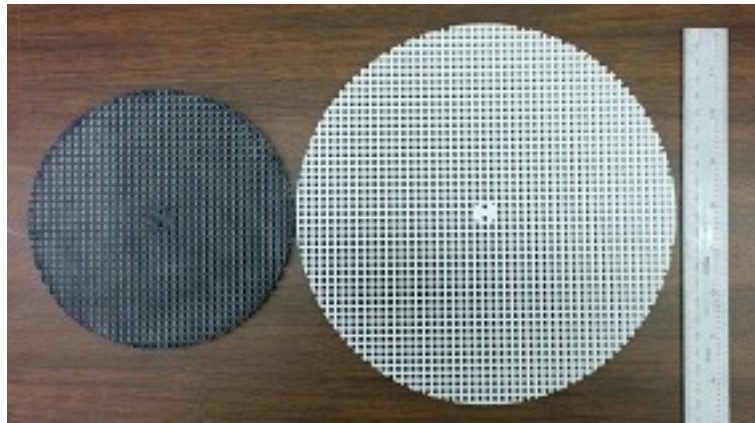


Figure 2.1: Porous Discs

A load cell was used to measure the drag force on the disc. The load cell was housed in a watertight enclosure that connected the disc to the mounting sting. This set-up allowed the disc drag to be measured directly, without interference from tower drag.

To provide a characterization for the 2 porous discs that are being studied, the C_T was determined over a range of inflow speeds in order to check for Reynolds dependency. The porous disc is located at 0.985 m from the inlet. The disc has been aligned so it is perpendicular with the flow direction (zero yaw) and right at the center of the cross section plane. A schematic of the experimental set-up is shown in Figure 2.2.

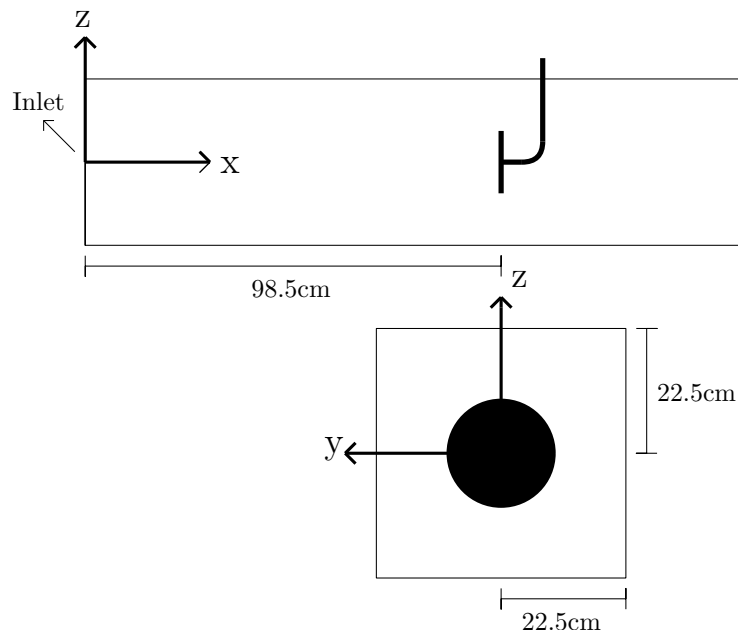


Figure 2.2: Location of the porous disc in the flume tank

The C_T was calculated using equation 2.1, where T is the experimental disc thrust force, A_{disc} corresponds to the cross sectional area of the porous disc, U_∞ is the inlet velocity of the water tunnel which was determined using Particle Image Velocimetry (PIV) and ρ is the water density.

$$C_T = \frac{T}{\frac{1}{2}\rho U_\infty^2 A_{disc}} \quad (2.1)$$

Axial Rotor

The testing rig was initially designed by Lártiga [17] and finished by Franchini [31]. It basically consists of a three-bladed rotor attached to a main horizontal shaft that drives the rotor, driven by a belt carried up through a vertical support tube to a servo motor. The horizontal and vertical tubes that compose the support-structure are made of aluminium tubing and are submerged in the water tunnel, thus resulting in a monopole foundation for the rotor rig. The motor and instruments of the system are placed above the water, on top of the cover of the water tunnel, as shown in Figure 2.3.

The rotor blades have been optimized to maximize its performance for low Reynolds numbers, given the characteristics of the experiments carried out at UVic’s flume tank. The blades are manufactured using the FDM machine at the SSDL lab. The total rotor diameter is 219 mm. More details about the new rotor design can be found on [31].

A torque cell is attached to the motor allowing the system to read torque values that will be used to obtain the performance curve of the blades.

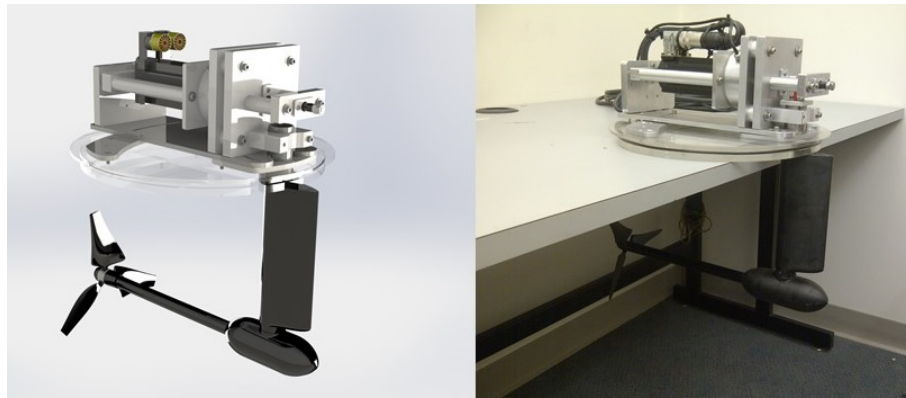


Figure 2.3: Schematic of the testing rig(left) and physical rig(right)

To obtain the characteristic curve mentioned above, the power coefficient (C_P) was computed for a range of tip speed ratios (λ) defined as:

$$\lambda = \frac{\omega R}{U_\infty} \quad (2.2)$$

where ω is the rotor rotational speed, R is the rotor radius and U_∞ corresponds to the velocity of the flow. The inflow speed was kept constant at 1.261 m/s¹ and

¹This value corresponds to the average inlet velocity when the pump frequency is set to 35 Hz.

ω was controlled accordingly to obtain different λ . Subsequently, C_P was calculated using the following relation:

$$C_P = \frac{P}{\frac{1}{2}\rho U_0^3 A_{disc}} \quad (2.3)$$

Where P refers to the power extracted by the turbine, calculated using $P = Q\omega$, where Q refers to the torque captured with the torque cell.

2.3.2 False top experiments

The second phase of the experiments involved measuring the drag force on the 150 mm porous disc for 3 different BR's. The BR is defined as the ratio of the model-frontal area to the test-section area. Since the model area corresponds to the surface of the porous disc, the flume cross sectional area needs to be modified in order to achieve different BR. The current lids of the flume tank are fixed and cannot be used for modifying the cross sectional area. Therefore a 'false top' was design and built in order to meet the requirements of this project.

The false top is made out of two 114.3 x 44.8 cm high-density polyethylene (HDPE) rectangular pieces, coupled by two standard aluminum rectangular tubes of 220 cm length. It is intended to be able to adjust the height of the false top with respect to the bottom of the water tunnel.

The drag force on the disc was measured for BRs of 8.7%, 11.6% and 17.5%, i.e. the false top was placed inside the water tunnel at 3 different heights, measured from the bottom of the flume tank, at 45, 33.8 and 22.5 cm respectively. For each case, the water tunnel was filled 7 cm above the false top, making sure that when the experiments were conducted there was no free surface effects happening on the wake region. U_∞ was set to 0.77 m/s since it was determined to be the minimum value for which it is possible to obtain clean force readings. Higher velocity values will also have an impact on Froude number (see section 2.4.3), which is also necessary to be kept within the typical values where tidal turbines can be deployed.

2.3.3 Open flume experiments

To study the free surface effects two variables were measured: the C_T for the same BR's used in the previous set-up and the water height along the centerline of the

It was decided based on the conclusions on blade deflection and performance from chapter 4

flume. Data were collected keeping U_∞ at 0.77 m/s and at different time frames, ensuring repeatability of the measurements. The BR in this case was calculated using the inlet's water height, which is the most reliable parameter that can be set.

To obtain the water height, the centreline of the flume was discretized into 16 different points, 7 before the disc and 9 after it. The height was measured by placing an adjustable rod on top of the centreline and carefully positioning it until it touched the surface. This method was more reliable than any ultrasonic-based sensor, since the maximum error was subjected only to 1 lead of the thread, which in this case was ≤ 1.27 mm. A schematic of this set-up is presented in Figure 2.4. The position of the disc remained undisturbed at 0.985 m from the inlet.

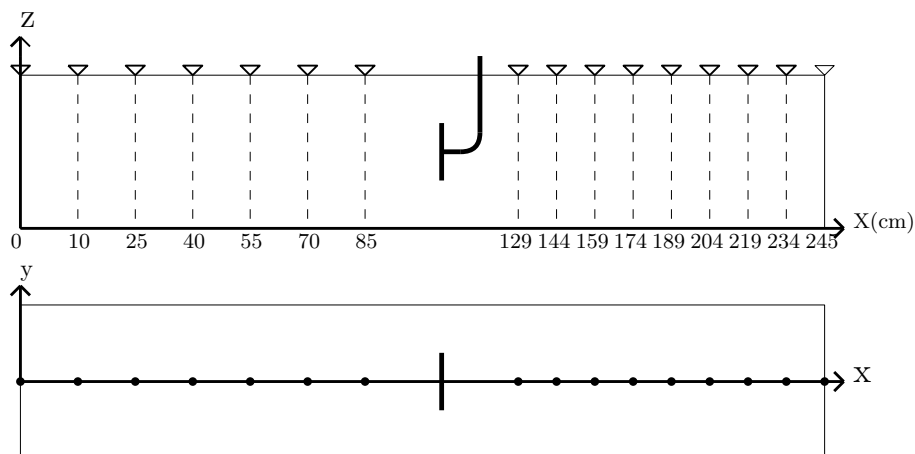


Figure 2.4: Height measurement points along the flume.

2.3.4 Experimental Error

Errors in experiments [32] generally fall into two categories: systematic (bias, epistemic) error and random (precision, aleatoric) error. When an error from a particular source is found to be significantly smaller than other existing errors, it will be neglected. For all of the experiments run, the data acquisition system was found to have a negligible impact compared to the uncertainty due to repeatability. For estimating the random error, a statistical analysis was performed. The *t-student* distribution was used to estimate the confidence interval of a mean value of a sample. A 90% confidence interval was employed for the experiments.

2.3.5 Experimental Results

The results show for both sizes of porous disc that there is a slight difference in the C_T values when the inflow speed increases, but they can be considered within the experimental error due to repeatability. It was therefore assumed that the C_T is invariant with Reynolds number. These results are shown in Figure 2.5.

In Figure 2.6 the C_T tendency with increasing blockage ratio can be observed for both open flume and false top cases. As expected, for both configurations the C_T tends to increase with higher blockage ratios and a slight difference between these two curves can be appreciated. The results show higher C_T when free surface effects are being considered, although it still falls within the experimental uncertainty.

The results for water height and axial rotor are presented in section 2.6.

2.4 CFD Simulations of Porous Disc

Previous work [33] has shown that a turbine operating in a constricted channel can produce significantly more power compared to a turbine placed in a very large unobstructed channel. This work now focuses on quantifying the effect of incorporating a free surface and foundations into the analysis.

The CFD software used for actuator disc modeling corresponds to STAR-CCM+, which uses a finite volume Navier-Stokes solver. The code solves the Reynolds-Averaged Navier Stokes (RANS) equations. The flow was assumed to be incompressible and steady-state solutions were of interest. The Reynolds averaging process introduces additional stress terms (Reynolds stresses) into the instantaneous Navier-Stokes equations. The Reynolds stresses, introduced from the Reynolds averaging, are modelled using the $k - \omega$ SST turbulence model by Menter [34], which has a well documented performance [35], [36].

2.4.1 Porous Disc Model

The most common method of implementing an actuator disc in CFD is to use a *momentum source model*, which effectively simulates the small scale induced turbulence that a porous disc generates when placed in the flow. This method has been used by many authors [37]–[39], showing good agreement with experimental results. In this work, an alternate approach for CFD simulations is employed. The *porous disc model*, which is also rooted in the actuator disc theory, uses a thin cylindrical disc,

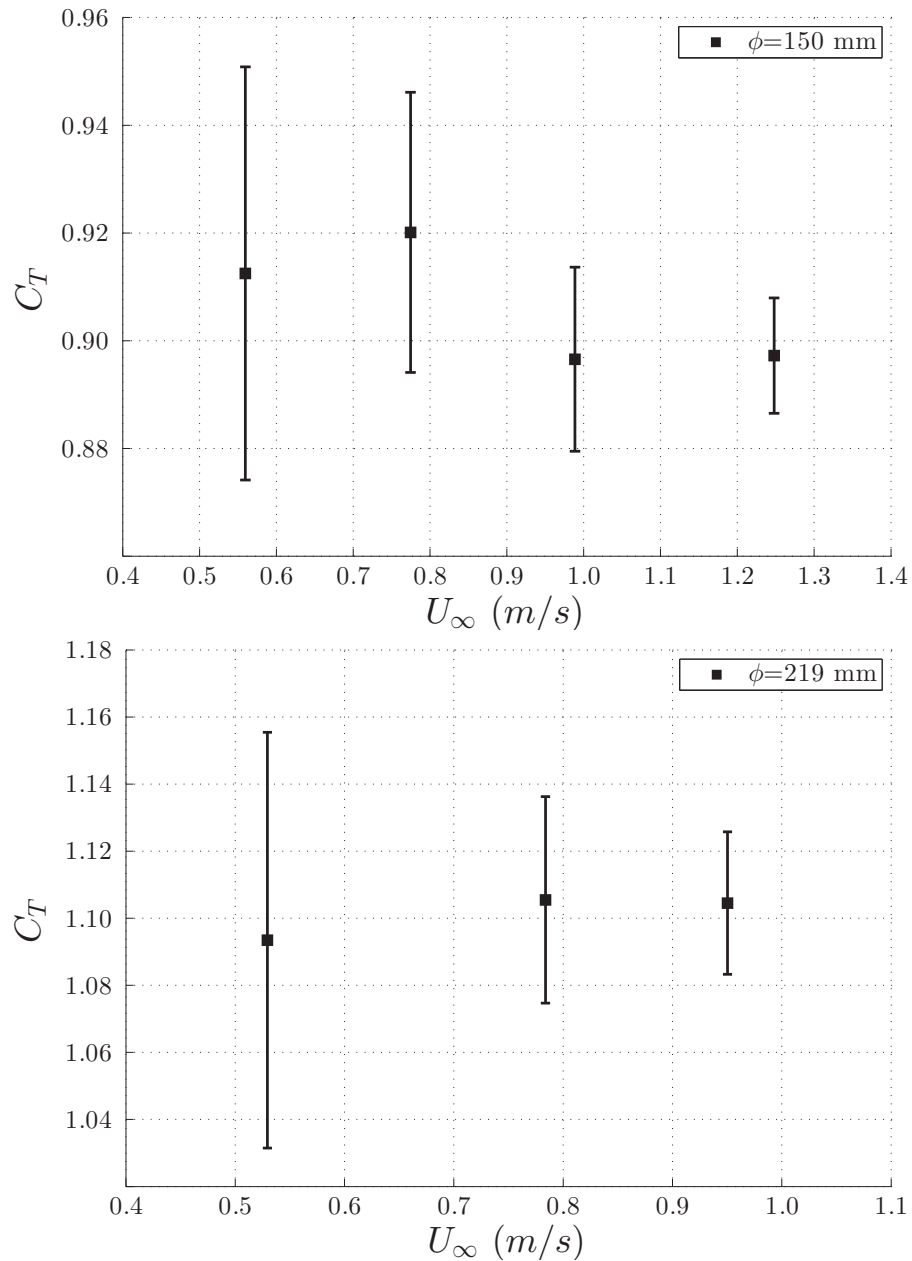


Figure 2.5: C_T obtained for both porous discs under a range of inflow speeds

similar to what experimental testing employs when using porous discs to represent a rotor. This simplified turbine model allows running many simulations in a short period of time. The porous disc model has several advantages:

- It is a closer representation of the physical porous discs used for experiments
- The settings used to specify the porous disc properties are not a function of

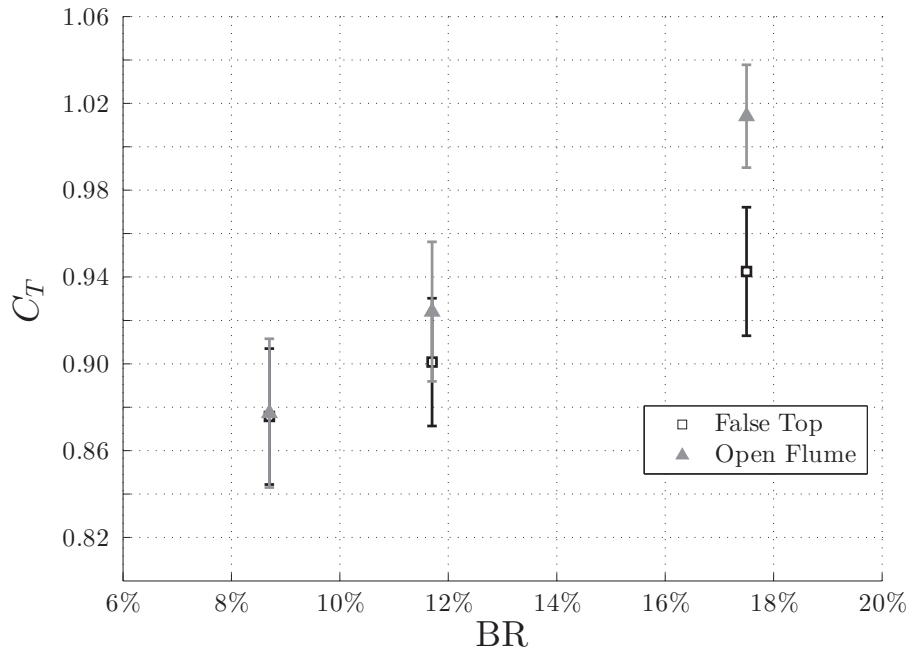


Figure 2.6: C_T for the 3 Blockage ratios using disc with $\phi = 150$ mm

incoming water speed

- Computation complexity, both meshing and solving, are considerably reduced

This model was validated with results obtained from UVic for an actuator disc using momentum source model, and also using Clean Current results for a ducted axial flow rotor in 2010. The thrust on the disc was calculated using:

$$T = \int_S \Delta p dS + \int_S \rho v^2 dS \quad (2.4)$$

Where Δp is the pressure difference between the upstream and downstream disc faces, S is the disc surface and v is the velocity through the disc. The power P is then calculated by multiplying the thrust by the x -direction velocity averaged over the volume of the disc ($\overline{u_{x-disc}}$)

$$P = T \overline{u_{x-disc}} \quad (2.5)$$

The thrust and power were subsequently non-dimensionalized using thrust and power coefficients using the previously defined equations 2.1 and 2.3.

Finally, the following ratios were used to calculate the percent change in T and P compared to an infinitely wide channel:

$$\%C_T = \frac{C_{T,calculated}}{C_{T,inf.channel}} \quad (2.6a)$$

$$\%C_P = \frac{C_{P,calculated}}{C_{P,inf.channel}} \quad (2.6b)$$

It is important to note, that for all results presented in this section, the percent change values were calculated based on the theoretical C_T of 8/9 and C_P of 16/27 for an infinitely large channel. The theoretical values were used as a baseline to allow for a more direct comparison between all simulation and future experimental results.

The porous disc settings specified for the CFD based analysis were initially tuned to match the experimental thrust measurement obtained in the closed flume for the 15 cm disc at a blockage ratio of 8.7%. All subsequent simulations settings were kept constant. However, as mentioned in section 2.6.1, the final experimental results were gathered after the CFD simulation studies.

The boundary conditions are the same as described later in section 2.4.3, using a slip-wall instead of the air-water interface.

For validation purposes, BR=0.5%, 5%, 10% and 20% were considered using MAVI's porous disc model. The disc support stings were not modeled. To reduce the required simulation time, only half of the domain was actually modeled, where a vertical symmetry plane along the tank centerline was used to split the domain. To match previous simulation work completed by UVic, the tank walls were modeled as slip walls, i.e. zero shear. Figure 2.7 presents the simulation results, showing both the percent change in C_T and the percent change in C_P . The discrepancy in the results is also in part attributed to differences in RANS solvers used (CD-Adpco vs. CFX), mesh structure, density settings and the method of calculating the reference velocity used for deriving C_P . In general, $\%C_P$ for all methods is within 5%-10% of the theoretical $\%C_P$.

2.4.2 Influence of Rotor Scale

The University of Victoria's flume tank was used to obtain experimental results to confirm predictions made by the CFD models. Because the flume tank is only 0.45 m wide, the size of the porous discs and rotors tested in the tank are much smaller

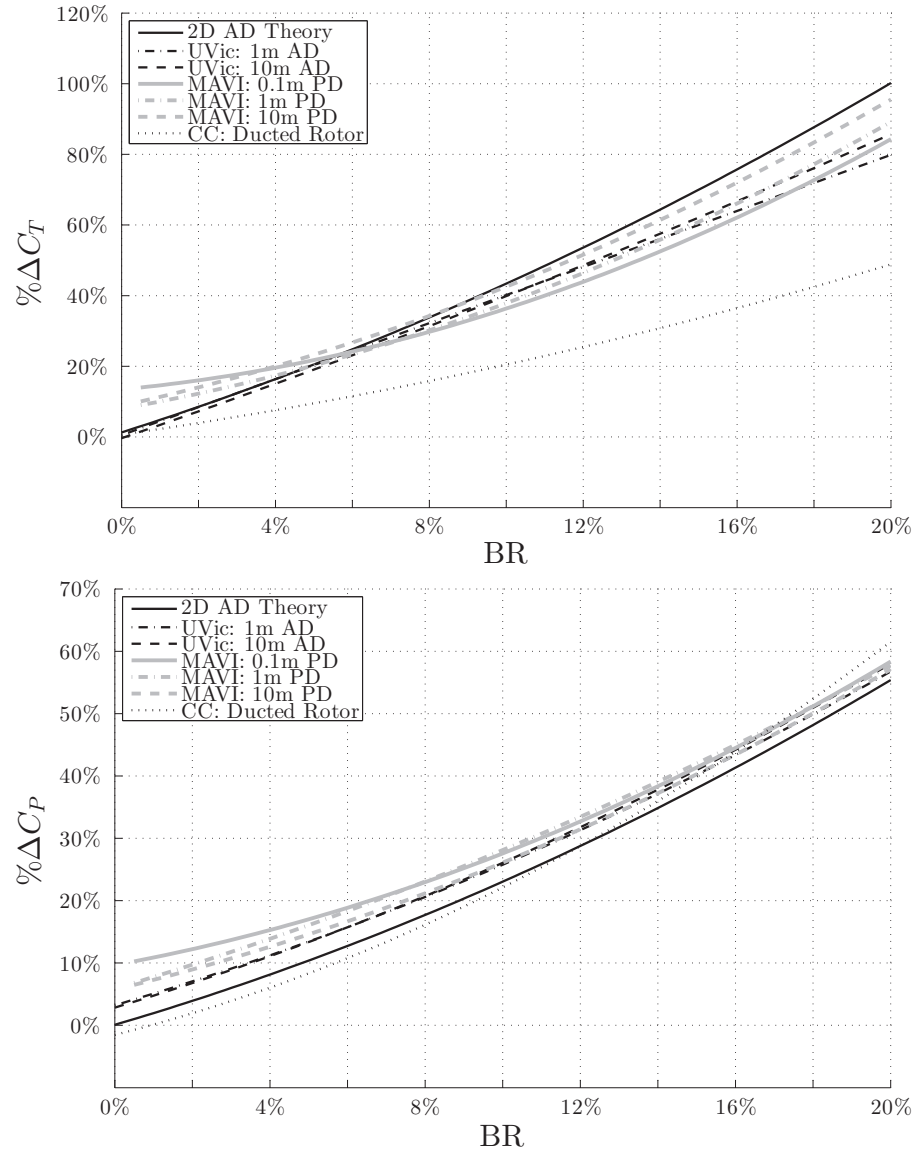


Figure 2.7: CFD Validation of Porous Disc Model, showing the comparison of % ΔC_T (top) and % ΔC_P (bottom) between UVic, Clean Current and MAVI results

compared to the turbines being deployed in rivers or tidal passages. For this reason, CFD models validated against experimental results at flume tank scale were subsequently run for larger rotor and channel sizes. Thus, the impact of rotor scale on the predicted turbine performance change due to channel blockage can be quantified.

Simulations were therefore run for three different rotor sizes (0.10 m, 1.0 m and 10 m) for a range of BRs. As shown in Figure 2.7, the predicted change in performance for the 1.0 m and 10 m turbines is nearly identical at each BR. The smaller 0.10

m disc follows the same trend closely at BR's above 10% , but over predicts the change in performance for a lightly blocked channel. The reason for this is still under investigation.

Based on simulations work to date for a porous disc, it can be concluded that an increase in scale from a 1.0 m to a 10 m rotor results in minimal change in performance as the percentage of channel blockage is increased.

2.4.3 Model Boundary Conditions

A uniform velocity, matching the experimental value that corresponds to $U_\infty = 0.77$ m/s, was set at the inlet. In addition, the inlet turbulence intensity was set to 0.8% and the length scale to 25 mm, following previous work results between UVic and MAVI [33].

The free surface was modeled as both a fixed slip wall and an actual air-water interface. A new CFD domain geometry, shown in Figure 2.8 was created to model the air-water interface. The water level was fixed at the outlet and was allowed to rise at the inlet. A hydrostatic pressure condition was applied at the outlet.

The inlet was split at the air-water interface using a wedge to help stabilize the simulation by creating a physical division between the air and water. As the channel becomes increasingly blocked with turbines, the water level at the inlet begins to rise along the wedge. If this wedge was not in place, the water would attempt to spill out through the air inlet causing instability in the simulation. The air and water inlets are defined as mass flow inlets instead of velocity inlets. Using mass flow inlets was found to significantly improve convergence.

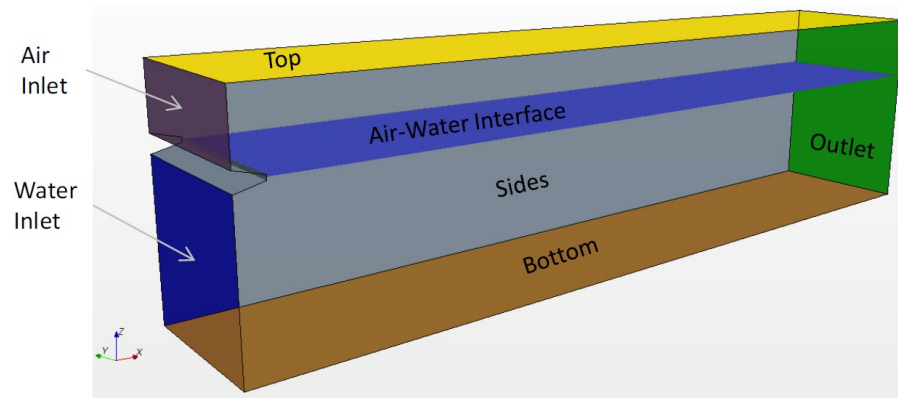


Figure 2.8: CFD model with inclusion of free surface

The non-dimensional parameter that will be used in free surface CFD simulations to characterise surface waves is the Froude number, defined as:

$$Fr = \frac{U_\infty}{\sqrt{gh}} \quad (2.7)$$

Where U_∞ corresponds to the speed of the flow and \sqrt{gh} is the speed of gravity waves, where g is the gravitational acceleration and h is the water depth. This parameter, using the water depth as the characteristic length, can also be found in previous studies [14], [20], [40] in good agreement between CFD and experiments. Table 2.1 shows the maximum Fr at several Canadian turbine deployment sites of interest. A Fr in the 0.15-0.5 range was determined to be appropriate for CFD simulations based on the results in table 2.1. To obtain Fr within this range for the UVic flume tank, the flow velocity was set to $U_\infty = 0.77$ m/s, which corresponds to a full scale free stream velocity of 3 m/s. A disk diameter of 0.15 m was used to improve the signal-to-noise ratio on the disc force measurement.

Location	Water depth (m)	Max U_∞ (m/s)	Fr
Seven Sisters Dam	8.5	2	0.22
Point Du Bois	4	3	0.48
Butze Rapids	15	4.7	0.39
Digby Gut	67	3.9	0.15
Petite Passage	35	5.9	0.32
Grand Passage	37	4.3	0.23

Table 2.1: Froude numbers of potential Canadian turbine sites

Using previous results, the Fr will be modified for each simulation following table 2.2.

Disc diameter (m)	BR (%)	U_∞ (m/s)	Fr
0.15	8.7%	0.77	0.37
	11.6%	0.77	0.42
	17.5%	0.77	0.52

Table 2.2: Froude numbers of free surface CFD simulations

2.4.4 Simulation Matrix

Three BRs were considered for this study, which are the same as the ones considered for the experiments, previously explained in section 2.3.2. The first set of simulations, summarized in Table 2.3, were run to investigate the effects of free surface on thrust and power production. No foundations were included. A second set of simulations were also run to determine if foundations need to be considered when developing power correction curves in blocked channels. Table 2.4 summarizes the parameters used for this set of simulations.

Blockage (%)	Disc ϕ (m)	U_∞ (m/s)	Top Surface
For comparison to closed-lid			
8.7	0.15	0.785	Slip-Wall
11.6	0.15	0.766	Slip-Wall
17.5	0.15	0.77	Slip-Wall
For comparison to open-lid			
8.7	0.15	0.789	Free-Surface
11.6	0.15	0.786	Free-Surface
17.5	0.15	0.826	Free-Surface
For comparison to axial rotor			
18.6	0.219	1.261	Slip-Wall

Table 2.3: Investigation into free surface effects

Blockage (%)	Disc ϕ (m)	U_∞ (m/s)	Top Surface
8.7	10	3.0	Slip-Wall
11.6	10	3.0	Slip-Wall
17.5	10	3.0	Slip-Wall
8.7	10	3.0	Free-Surface
11.6	10	3.0	Free-Surface
17.5	10	3.0	Free-Surface

Table 2.4: Investigation into influence of foundations

2.4.5 Impact of Modeling the Free-Surface on Channel Blockage

To analyse the impact of free surface effects on power extraction, two operating conditions were considered:

1. Turbine (porous disc) settings are kept constant irrespective of BR

2. Turbine (porous disc) is tuned to operate at the maximum power point (MPP)

The results obtained for the first operating case, presented in figure 2.9, indicate that for both situations the overall performance increases with increasing BR, in agreement with previous studies [12], [14], [19], [33]. However, the results show that thrust force and power on the disc decreases in the presence of free surface compared to the slip wall case, showing discrepancies with the work done by Whelan *et. al* [14] and the experimental results. The analysis and comparison with experimental results regarding this discrepancy can be found in section 2.6.

Figure 2.10 depict how the free surface deforms in the presence of the disc. The contour plots show that upstream of the disk, the water elevation is higher than downstream of the disk where a clear wave trough is observed.

In contrast, when the disc is tuned to operate at the maximum power point, C_T and C_P are nearly identical irrespective of whether a free surface is modeled or replaced by a slip wall, as shown in figure 2.11.

2.4.6 Impact of Foundations on Channel Blockage with Inclusion of Free Surface

To date, all of the simulation work was focused on modeling facsimiles of turbine rotors, without the inclusion of any non-power generating structures such as the nacelles that house the power take-off and conversion equipment, or the foundations that keep the turbine in place. It is presumed that if a foundation is significant enough in size and occupies a large enough portion of the channel, its presence will block a portion of the channel and thereby influence the turbine's power output. Tidal and in-stream river turbines, and their associated foundations, have not converged on a single design as is the case with their cousins in the wind industry. There are gravity based ducted turbines, open rotor turbines mounted on piles, multi-rotor designs with unique foundations and various types of floating-moored turbines. Some of these turbine designs are merely concepts, but most have been tested at pre-commercial scale. The large variability in foundation designs means that several types of foundations will need to be considered before any generalized conclusions can be drawn.

A monopole type foundation, shown in Figure 2.12, was selected as the first case to consider, primarily because this is the foundation that will be used for experimental testing in the flume tank. As was the case with previous simulations, a symmetry condition was used along the flume tank longitudinal axis.

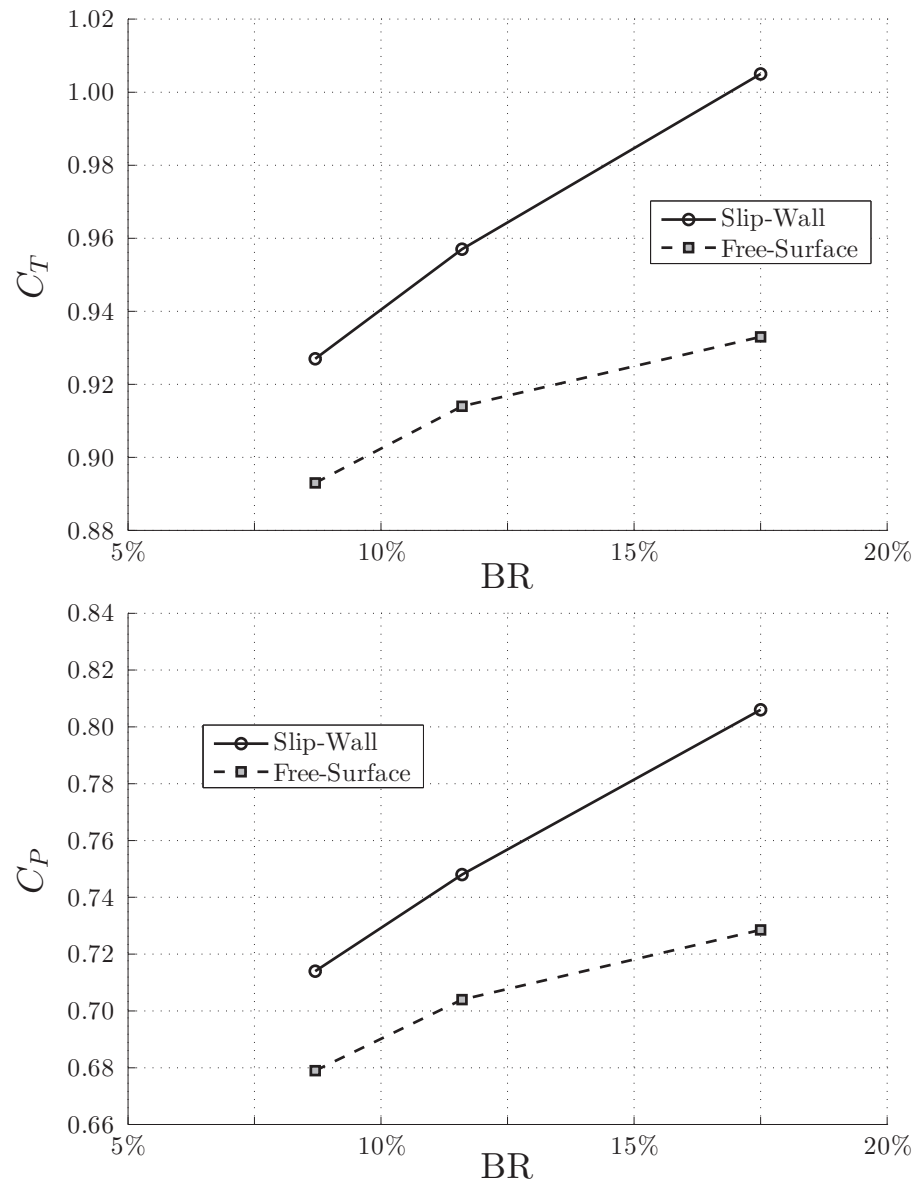


Figure 2.9: CFD results between Slip-Wall and free-surface simulations, showing the impact on C_T (top) and C_P (bottom) when simulation settings are kept constant, irrespective of BR

A second foundation type with the support pile in place of the rotor was also analyzed. A pile with a 3 m diameter was placed alongside the rotor as shown in Figure 2.13b. This foundation is comparable to that used by Open Hydro (Figure 2.13a).

Figure 2.14 compares the percent change in C_T and C_P between the two different foundations as channel blockage is increased. The analysis for the second foundation

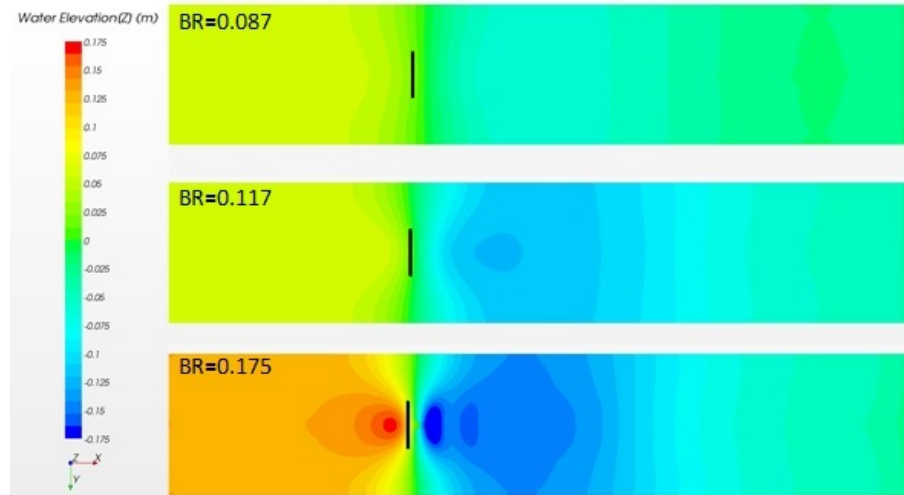


Figure 2.10: CFD results showing water elevation contour plots at three different BR, for free-surface simulation cases

was only run for the highest BR of 17.5%.

The results show that the monopole type foundation has a negligible effect on C_P . The lack of impact on C_P due to the foundation is likely due to the fact that the foundation structure is located entirely downstream of the disc. Conversely, a significant increase in power is observed for the second foundation type. This result confirms that a structure placed in-plane with the rotor will impact turbine power production.

The foundation's impact on performance is therefore directly coupled to the shape of the structure and its interaction with the turbine. A highly streamlined structure (the extreme case being a duct) will greatly increase the power produced by a turbine when compared to a truss type structure for example, even though both foundations may occupy a similar cross-sectional flow area. Developing a general correction factor to account for foundations is therefore likely not possible given the present variability in foundation types and geometries.

2.5 CFD Simulations of an Axial Flow Rotor

All of the results obtained thus are focused on modeling and testing porous discs that are idealized facsimiles of real turbines. The use of simplified turbine models has many benefits including simpler experimental set-up and faster simulation run times. There are important differences, however, between real rotors and porous disks that

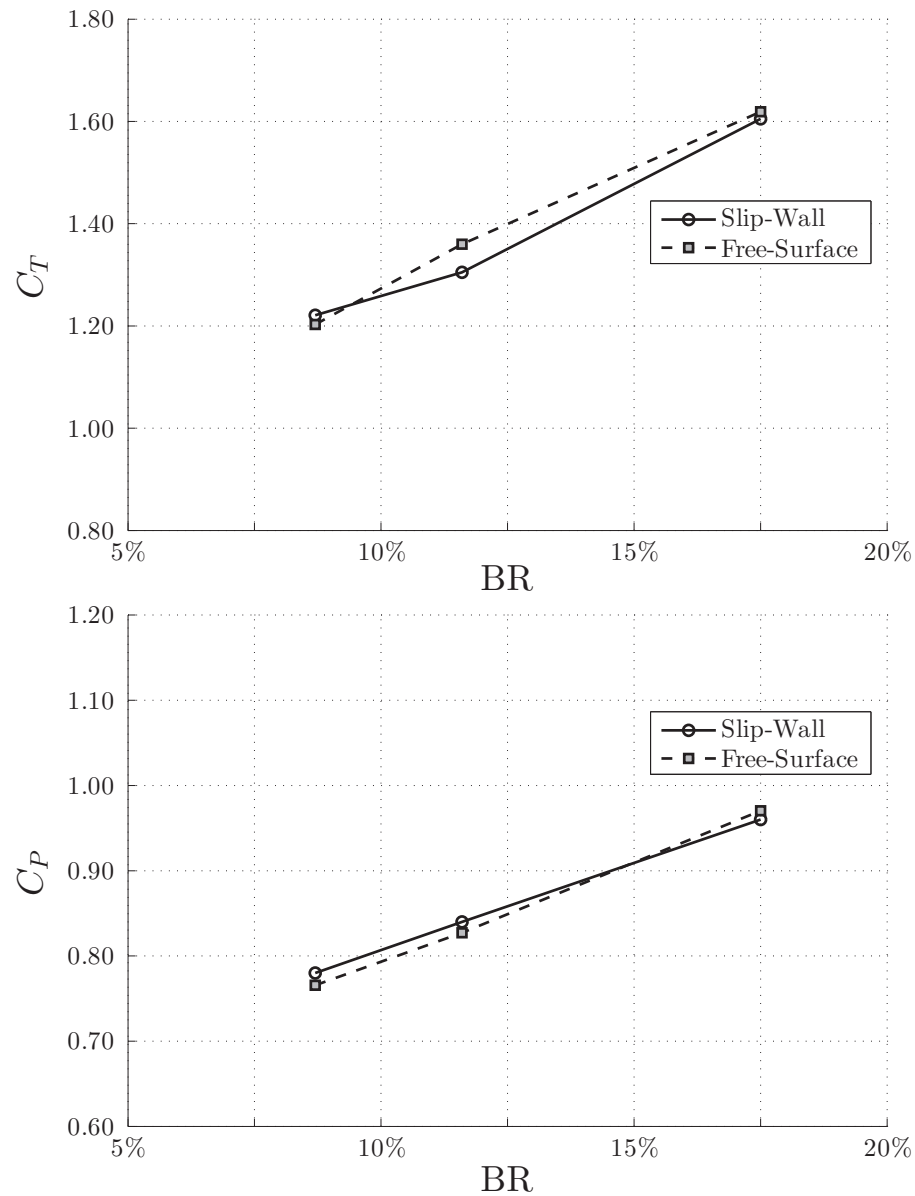


Figure 2.11: CFD results between Slip-Wall and free-surface simulations, showing the impact on C_T (top) and C_P (bottom) when simulation settings are tuned to operate at MPP

need to be well understood and documented to ensure that the corrections for channel blockage effects are valid.

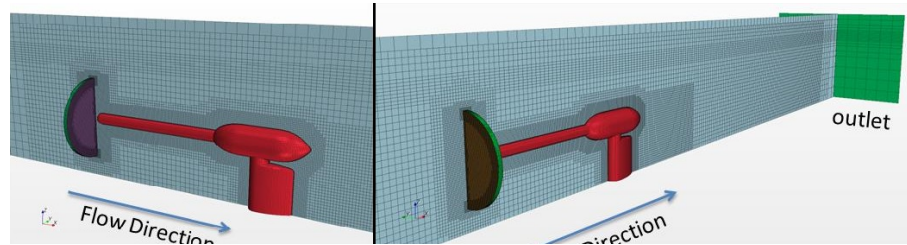
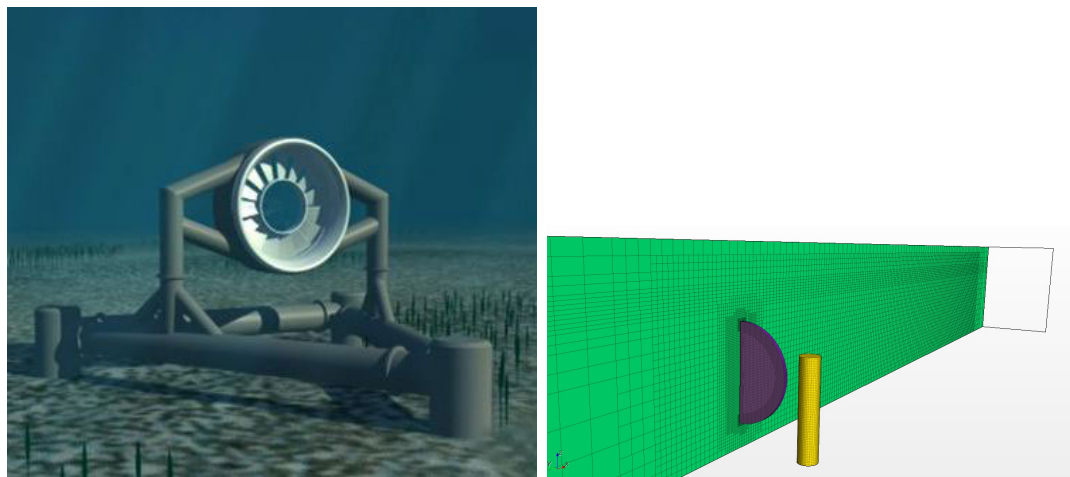


Figure 2.12: Porous disc model with monopole foundation



(a) Open Hydro ducted turbine

(b) Porous disc model with foundation structure in the plane of the rotor

Figure 2.13: Use of gravity foundations for porous disc model

2.5.1 Background and preparation

A number of CFD simulations were ran using UVic's small scale axial rotor, described in 2.3.1. The entire model was replicated in the CDF environment, i.e. the 219 mm three-bladed rotor mounted on the same monopole foundation geometry, as shown in figure 2.15. The CFD simulations of the rotor were performed without including free surface effects, using a non-slip boundary condition at the top.

The experimental test only allowed for the rotor to be tested at a BR=18.6% in a close lid flume tank, i.e. no free surface effects. To account for other BR, namely 11.6% and 8.7%, the virtual water channel in the CFD simulation was modified in width only, maintaining the same 45 cm water depth so that the foundation geometry remained unaltered.

For each BR, simulations were run at three λ to capture the turbine's peak performance point. At BR=18.6%, the flume tank tests indicated that λ for peak per-

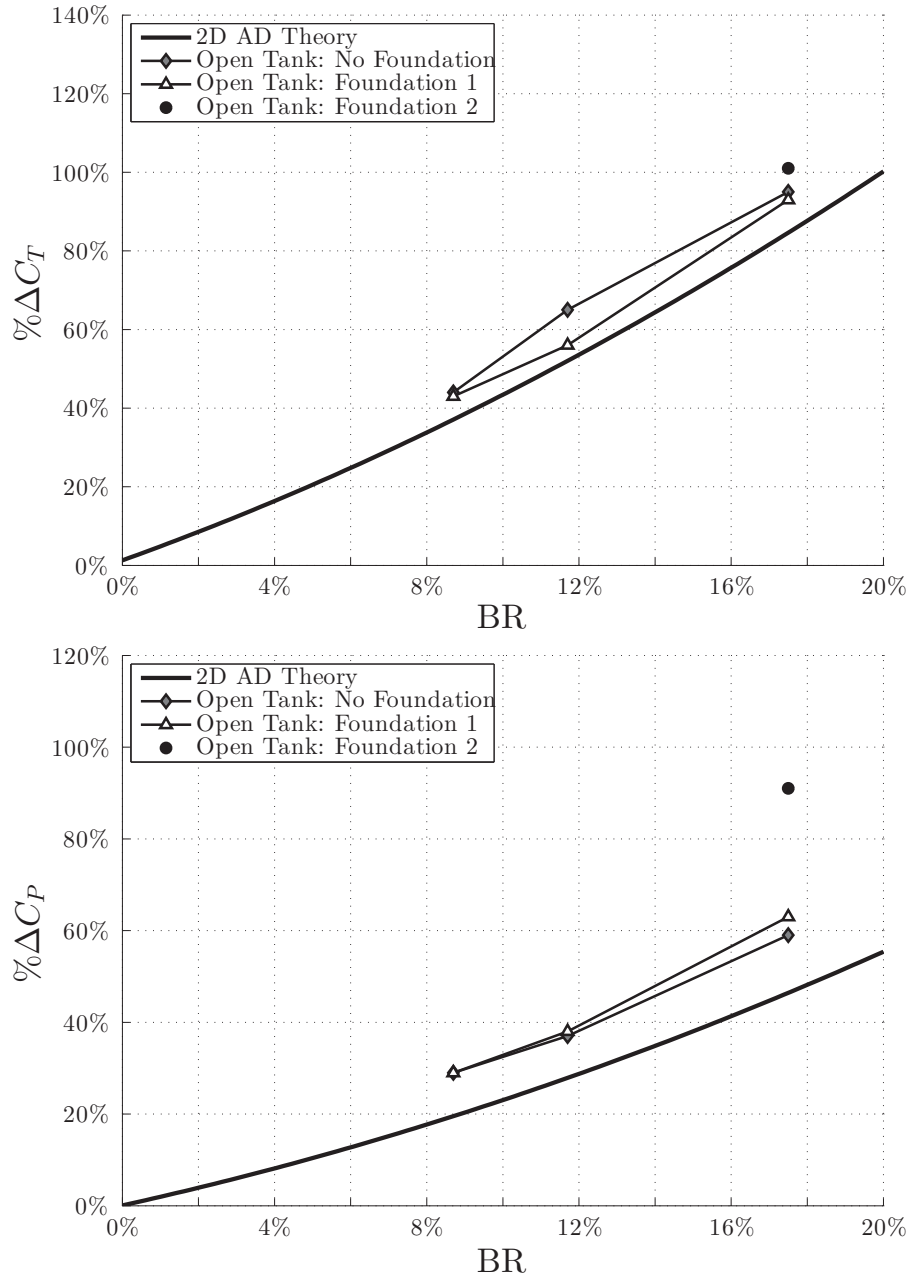


Figure 2.14: Impact of foundations on blockage effects

formance point was about 3.5. Therefore, to capture the turbine's peak performance point accurately, $\lambda=3.0$ and $\lambda=4.0$ were added to the CFD test matrix for BR=18.6%.

The TSR for the CFD simulations of BR=11.6% and 8.7% were calculated using a correlation obtained from the experimental porous disc results from figure 2.6, for the false top case. In all cases, a flume tank velocity of 1.261 m/s was replicated in

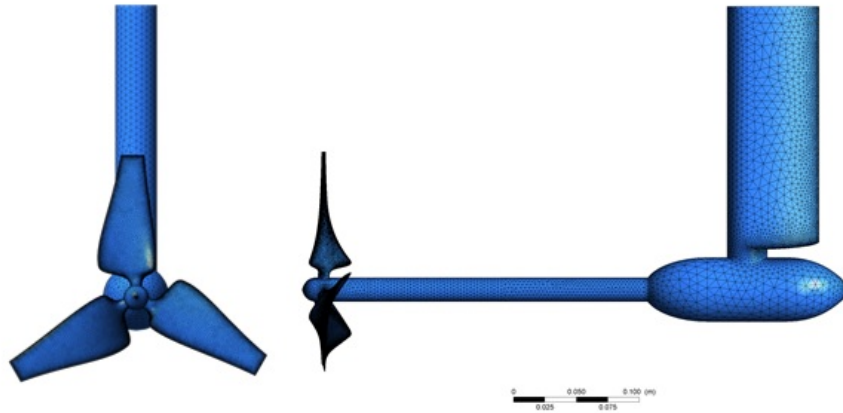


Figure 2.15: CFD model of rotor and foundations

the CFD simulations. The results are presented in table REF.

2.5.2 CFD Set-up

To replicate the test set-up, the blade plane was situated at 755 mm from the flume's inlet. It was vertically centered at 225 mm from the bottom of the tank. In all blockage cases investigated, the rotor was kept horizontally centered.

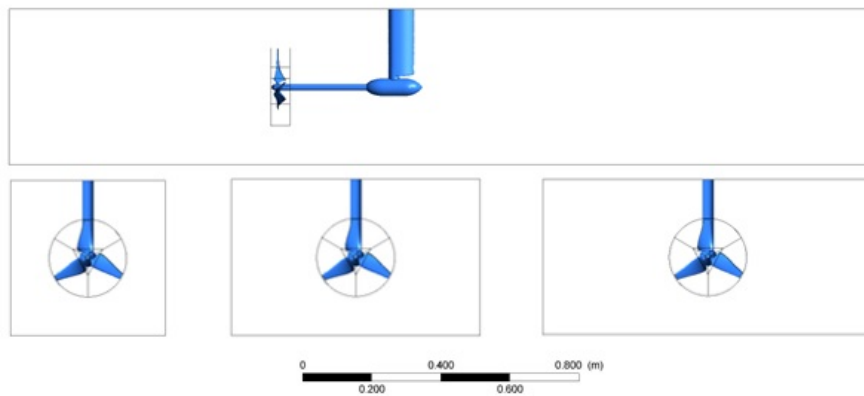
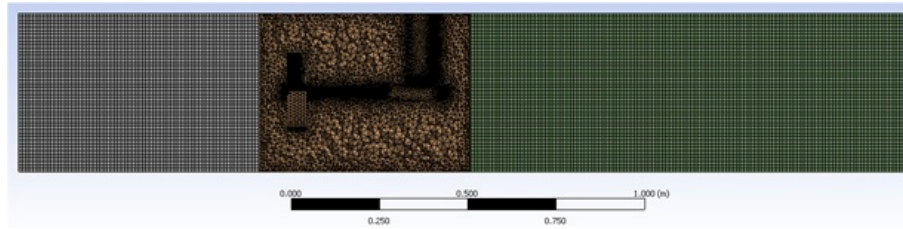


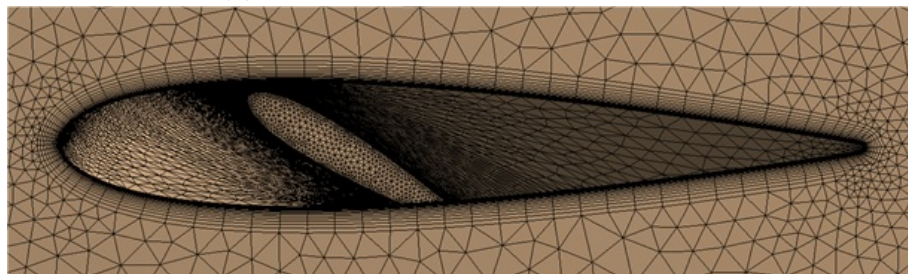
Figure 2.16: Top: Side view of the turbine in the virtual flume tank. Flow is from left to right. Bottom: Frontal view for BR = 18.6%, 11.6% and 8.7%. Cylindrical region around the blade corresponds to the rotational domain.

A stationary domain is considered for the CFD set-up, except at the blades, where a cylindrical region around the rotor is modeled as a rotational domain, as shown in figure 2.16. The near field region, including the rotational domain, was meshed with

tetrahedral elements to preserve geometric conformity, whereas hexahedral elements were used in the far field regions to reduce computational load (Figure 2.17a). In the rotational domain, inflation layers of prismatic elements were utilized to capture the non-dimensional wall distance (y^+) values below 2 for the low Reynolds number turbulence models to work (Figure 2.17b). The total number of elements employed per BR is approximately 6 millions.



(a) Near and far field mesh topologies



(b) Inflation layers about the blade

Figure 2.17: Mesh topologies for CFD simulations

The Shear Stress Transport (SST) model was used as the low Reynolds number turbulence model. Figure 2.18 illustrates the CFD model boundary conditions. A normal inlet velocity of 1.261 m/s was applied as the inlet boundary condition. The outlet was modelled with the opening boundary condition with the entrainment option of zero relative pressure and turbulence gradient. Side walls as well as the top and bottom bounds were set to have non-slip wall conditions. The fluid medium was chosen to be fresh water with properties of $\rho = 997 \text{ kg}/\text{m}^3$ and $\mu = 0.0008899 \text{ kg}/(\text{ms})$.

In order to perform a more thoroughly study and also to compare simulations, both steady state and transient analysis are considered. A steady state simulation computes the fully developed solution that does no change in time, whereas a transient analysis is a marching time solution, which can capture non-linearities by computing the values at each time step.

The simulations were run for 1000 iterations in steady state, after which they were run for 300 time steps in transient mode, each with 10 coefficient loops. The rotor

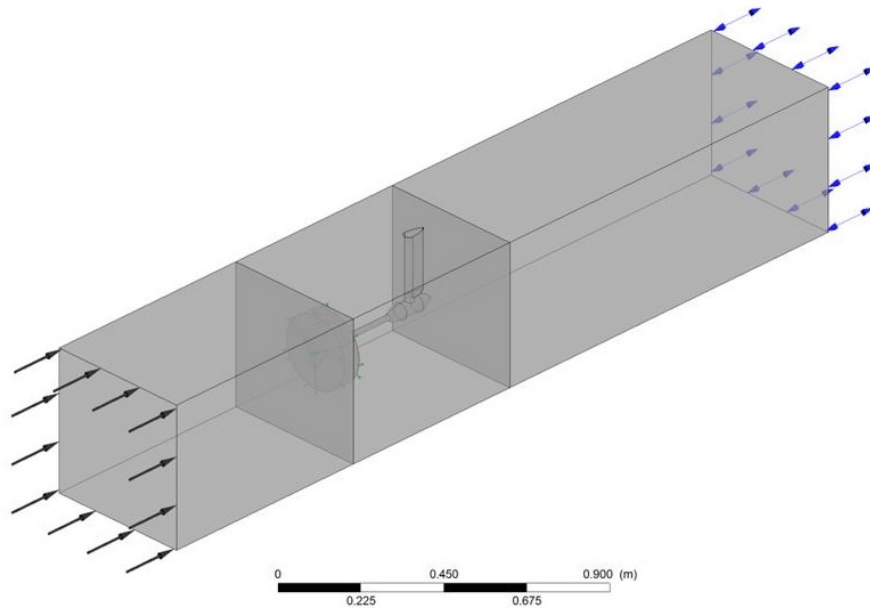


Figure 2.18: CFD model with applied boundary conditions: Single arrows indicate the normal inlet velocity, whereas double arrows show the opening boundary condition at the outlet of the domain

completed a full rotation in 60 time steps making each time step corresponding to a 6° rotational increment.

The final simulation matrix is presented in table 2.5

BR (%)	Tank width	TSR	ω (rad/s)
18.6%	0.45	3.000	34.548
		3.500	40.306
		4.000	46.064
11.6%	0.715	2.910	33.512
		3.390	39.039
		3.880	44.682
8.7%	0.962	2.890	33.281
		3.370	38.809
		3.860	44.452

Table 2.5: Axial rotor CFD simulation matrix, where the inlet velocity $U_\infty = 1.261$ m/s and tank width=0.45 m were kept constant throughout the simulations

2.5.3 CFD Rotor Simulation Results

The y^+ values on the blades were obtained and are shown in Figure 2.19. The root of the blade lacked the inflation layers, therefore the values are outside the target

range. Fortunately, the root area has little effect on the performance of the rotor. In this region, the flow is highly separated and the flow more inertially dominated, therefore having no inflation layers in this area is a small compromise to increase the calculation accuracies and to ease the meshing about the rotor.

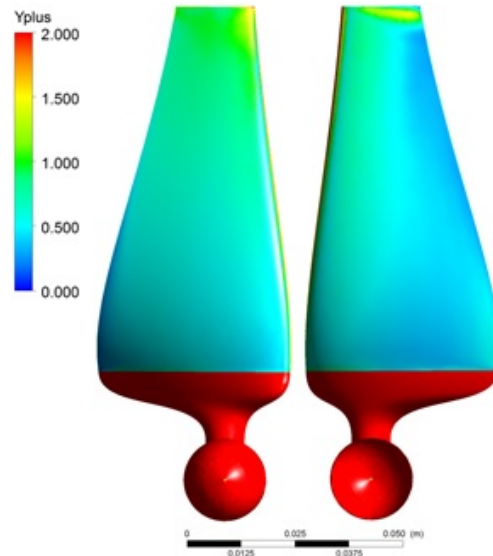
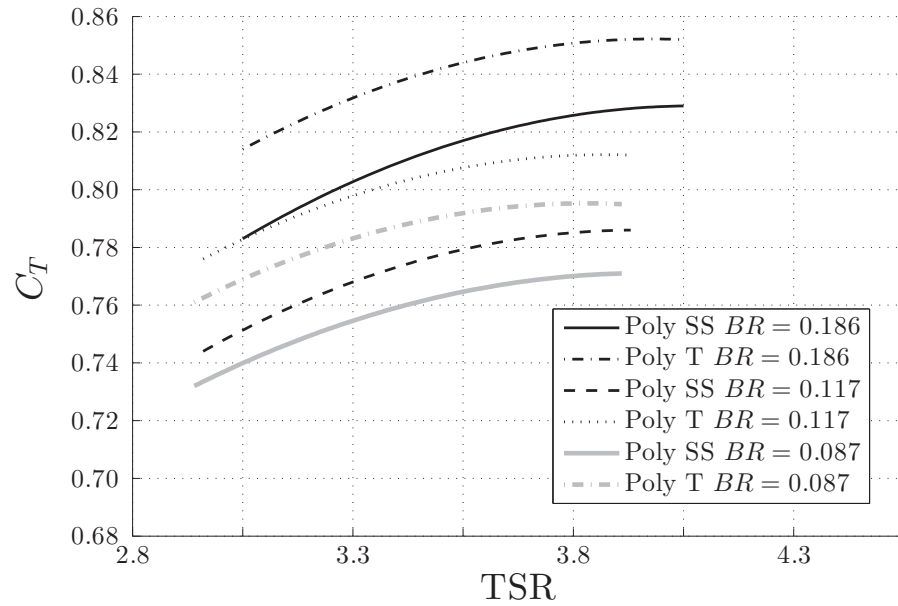


Figure 2.19: $y+$ values on the blades. Left: Upstream (high pressure) side. Right: Downstream (low pressure) side.

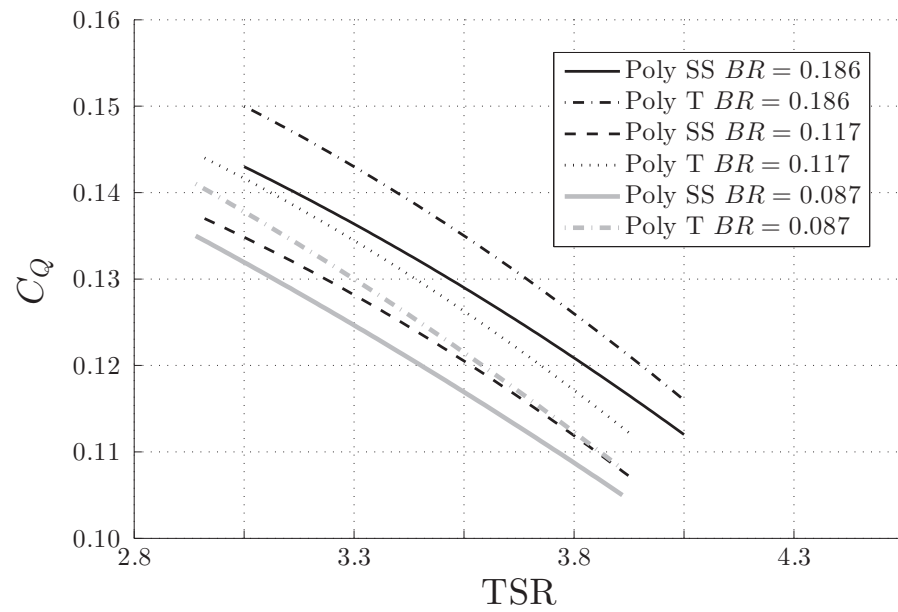
For steady state and transient simulations the following parameters were computed: C_T , torque coefficient (C_Q), C_P and the Velocity Ratio (VR), defined as the ratio of the axial velocity through the rotor to the inlet fume tank velocity, which was kept constant at $U_\infty = 1.261$ m/s.

To assess the actual peak performance points of the rotor, polynomials were fitted to C_T , C_Q , C_P and VR, as shown in figures 2.20 and 2.21, for steady state and transient simulation results. The maximum C_P and the corresponding TSR were calculated for each BR based on figure 2.21a to determine the peak performance point of the rotor at different BR. C_T , C_Q and VR values at the peak performance points were determined using the fitted curves from figures 2.20, 2.21 and the TSR at the peak C_P . Tables 2.6 and 2.7 show the peak performance values for steady state and transient simulations respectively.

It is clear from the analyses that there is a slight difference in the steady state and transient results. This is partially due to the fact that the wake structure in reality is not steady with respect to a stationary coordinate system particularly with a foundation structure behind it.

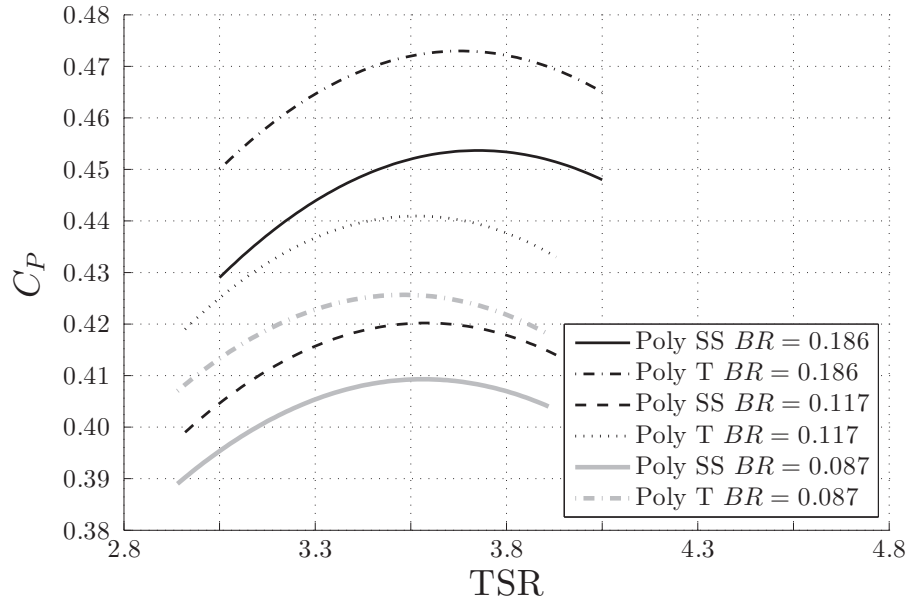


(a)

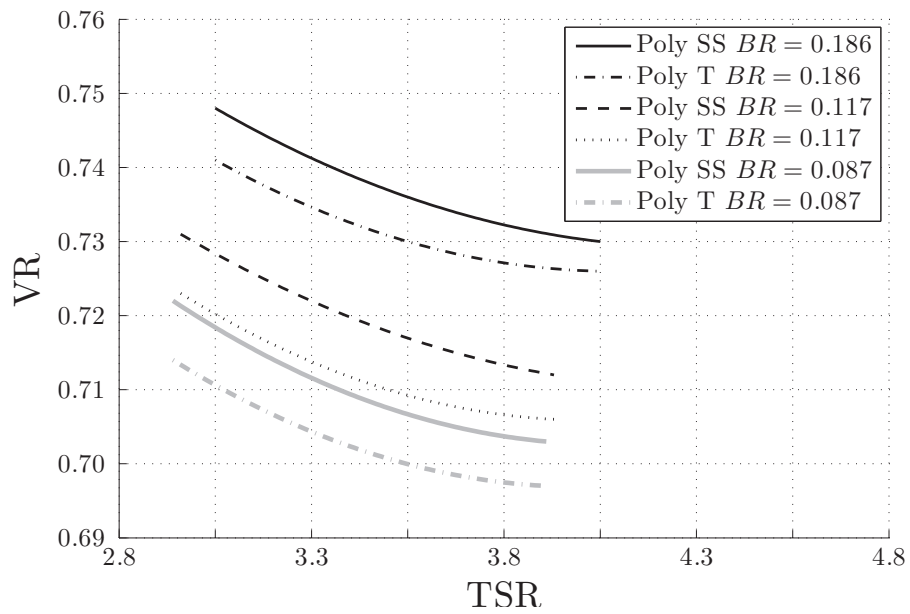


(b)

Figure 2.20: Steady-state (SS) and Transient (T) results showing the effect of BR on λ for C_T and C_Q



(a)



(b)

Figure 2.21: Steady-state (SS) and Transient (T) results showing the effect of BR on λ for C_P and VR.

In addition, figures 2.22, 2.23 and 2.24 show the relative values of these peak performance values with respect to those at BR=18.6% for steady state and transient simulations.

The results clearly show that C_T , C_Q , C_P and VR are all increasing with BR. Figure 2.22 shows the change in relative λ and VR with BR. By definition, it is expected that λ and VR are affected similarly by the BR, if BR does indeed affect the effective velocity through the blade plane. The transient results show a very good correlation between λ and VR in terms of their relative change with BR. The steady state results, interestingly, lack this correlation. This may be due to some numerical error in the calculation of the peak performance values of interest. Similarly, relative C_Q , C_T and VR^2 are shown in Figure 2.23. These results show a significant correlation between these values, particularly for the transient case.

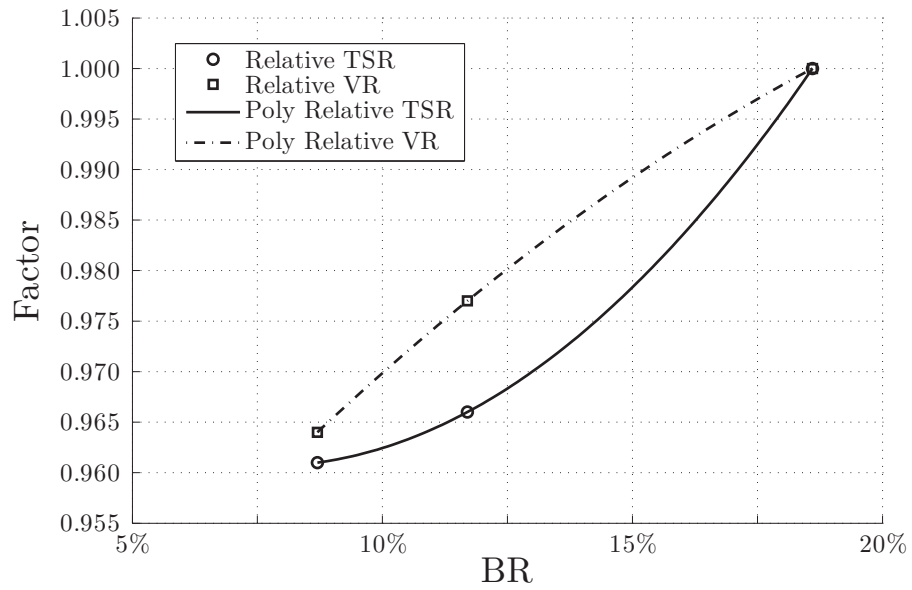
Finally, the relative C_P and VR^3 were compared against the BR in Figure 2.24. Both steady state and transient results show a good correlation between C_P and VR^3 . The results clearly indicate that the BR impacts the effective velocity through the rotor such that the turbines in constricted channels would behave as if they were subjected to higher velocities in a free stream environment.

BR (%)	TSR	C_T	C_Q	C_P	VR
18.6	3.669	0.823	0.124	0.454	0.733
11.6	3.543	0.780	0.119	0.420	0.716
8.7	3.527	0.765	0.116	0.409	0.706

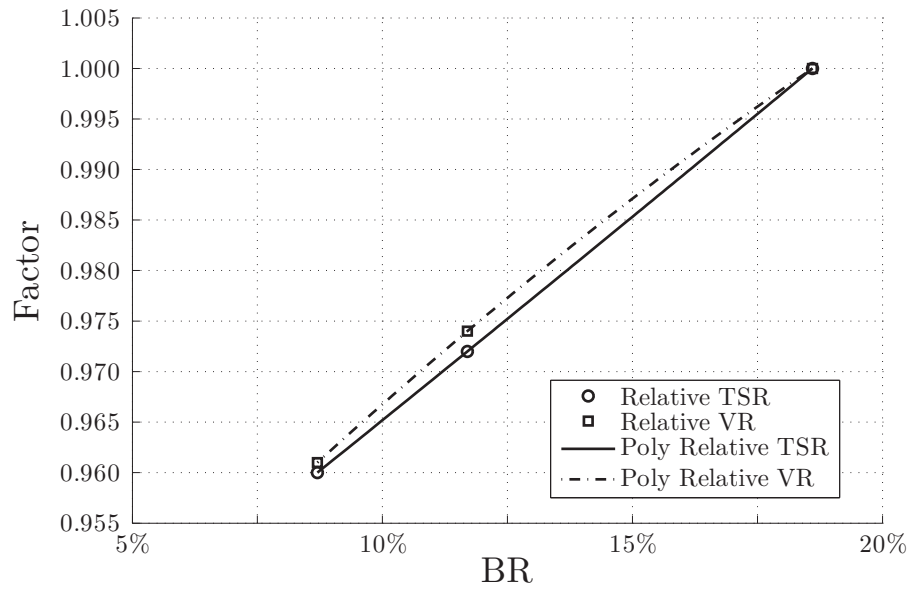
Table 2.6: Peak performance values based on steady state simulation results

BR (%)	TSR	C_T	C_Q	C_P	VR
18.6	3.626	0.848	0.131	0.473	0.728
11.6	3.523	0.808	0.125	0.441	0.709
8.7	3.483	0.791	0.122	0.426	0.700

Table 2.7: Peak performance values based on transient simulation results

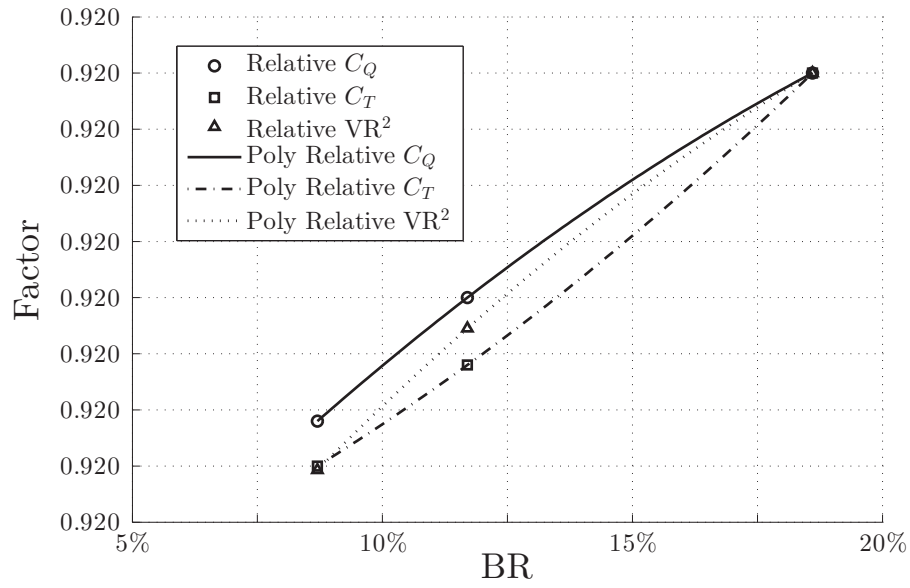


(a) Steady State

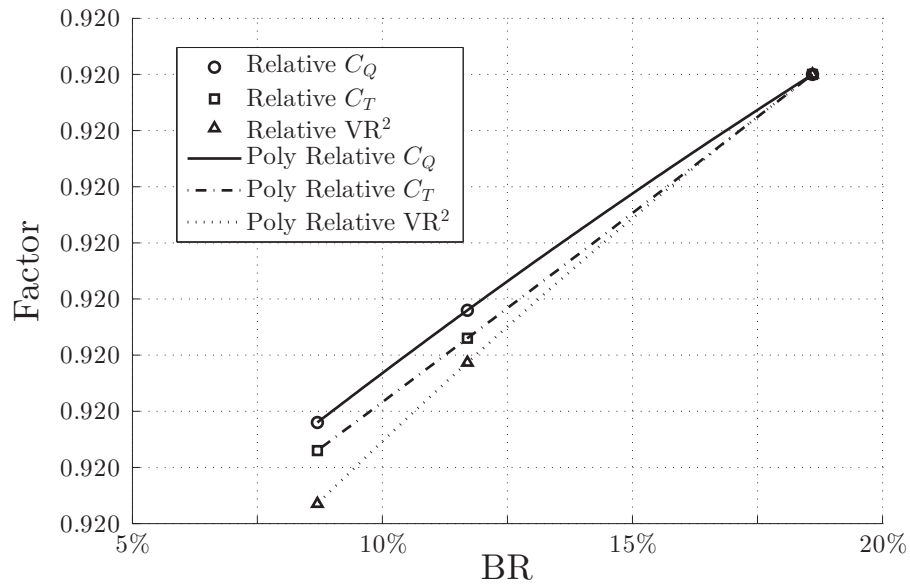


(b) Transient

Figure 2.22: Effect on BR on relative λ and VR at peak performance point

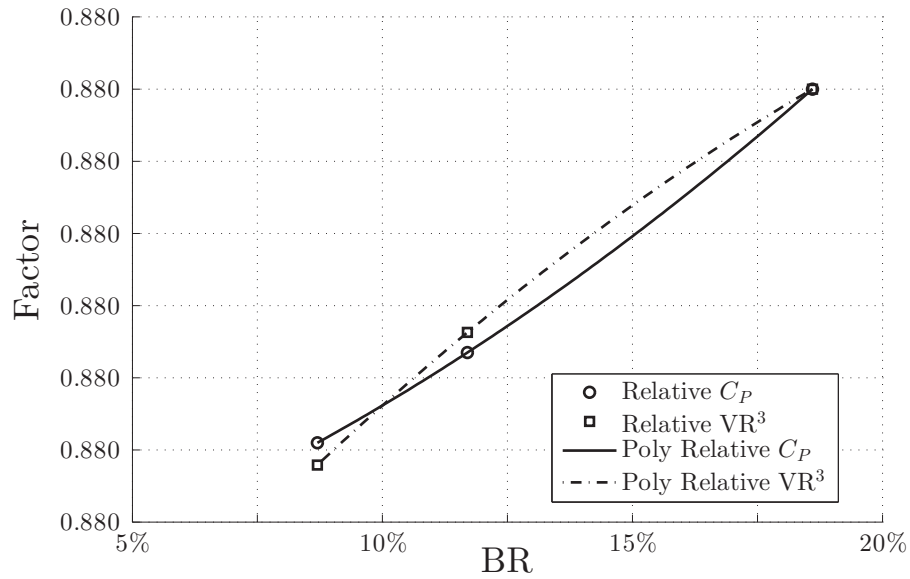


(a) Steady State

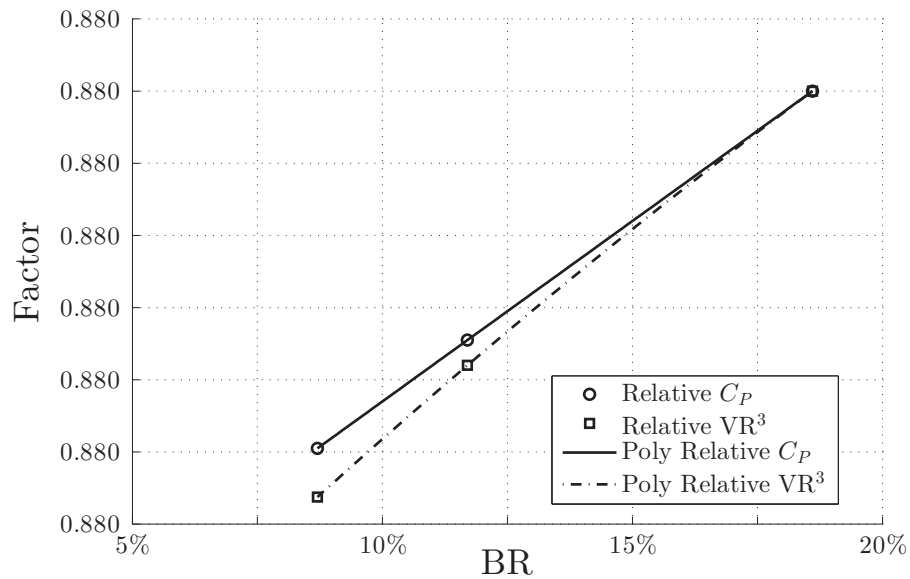


(b) Transient

Figure 2.23: Effect on BR on relative C_Q , C_T and VR^2 at peak performance point



(a) Steady State



(b) Transient

Figure 2.24: Effect on BR on relative C_P and VR^3 at peak performance point

2.6 Comparison of Experiments to CFD Simulations

2.6.1 Porous Disc vs CFD

The experimental and CFD results for both the closed and open flume tank conditions are compared in Figure 2.26. The comparison is done on a thrust force basis since

the disc drag was the actual value directly measured (as opposed to power).

It is important to mention that the final experimental campaign was executed after the simulation results, which is the main reason why the C_T value shown in figure 2.26 for BR=8.7% does not match the experimental value. This value can be manually modified by changing the resistance coefficient in the simulations to match the experimental results at that BR. Nevertheless, the final results show a great agreement in predicting the linear trend as blockage increases. The slopes are almost identical and show evidence of increasing performance as blockage increases.

The water depth along the length of the channel was also compared between CFD and experiments to further validate the work. Figure 2.25 plot the water elevation at the 3 BR being studied. In general, good agreement is shown between the CFD and experimental results given the error margin in measuring the water elevation during the experiments, caused by the inherent flow unsteadiness, observed as very subtle variations on the height, going up and down a few millimeters over a short period of time. In order to find the most representative height for each measurement, the minimum and maximum registered height was captured over a 5 min time window, thus reducing the measurements errors. A final average between the minimum and maximum values was taken for each point on the free surface.

A different scenario was found when free surface effects were considered. Even though both curves show evidence of performance improvement, the CFD results predicted a reduced performance when free surface effects are taken into account. There are mainly two reasons that explain these results. According to the CFD free-surface model definition, the boundary conditions set a fixed outlet height, allowing the inlet to rise. This results in a decrease of blockage ratio, according to Whelan's definition, that uses the inlet height to compute the BR. Looking at figure 2.25 it can be seen that, for the highest BR of 17.5%, there is a slight difference in the inlet height compared to experiments, thus decreasing the actual BR. However, this difference is almost negligible ($\approx 0.3\%$) and does not explain the drop in C_P .

The second reason involves the free surface deformation directly upstream of the porous disc, which is shown to increase as Fr increases, according to figure 2.25. This standing wave increases the effective cross sectional area, thus decreasing the inflow velocity at the disc. Since C_T and C_P are proportional to the velocity squared and cubed, respectively, a minor drop in the velocity could have a noticeable decrease in effective thrust and power. The same figure shows a negligible upstream surface deformation regarding the experimental results. Therefore, the potential benefit of a

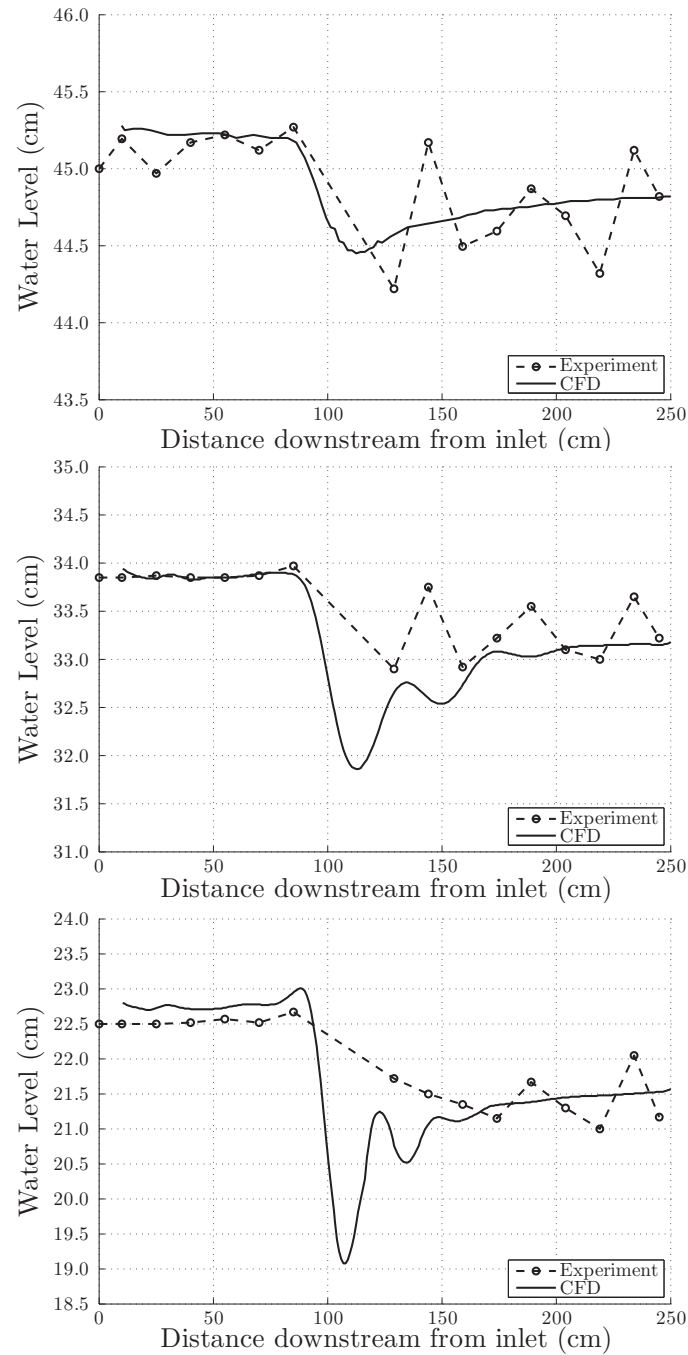


Figure 2.25: Comparison between CFD and experiments showing the free surface deformation for (a) $BR=8.7\%$, (b) $BR=11.6\%$ and (c) $BR=17.5\%$

higher Fr gets diminished by the effective velocity reduction at the porous disc plane. Similar results were found by Adamski [41].

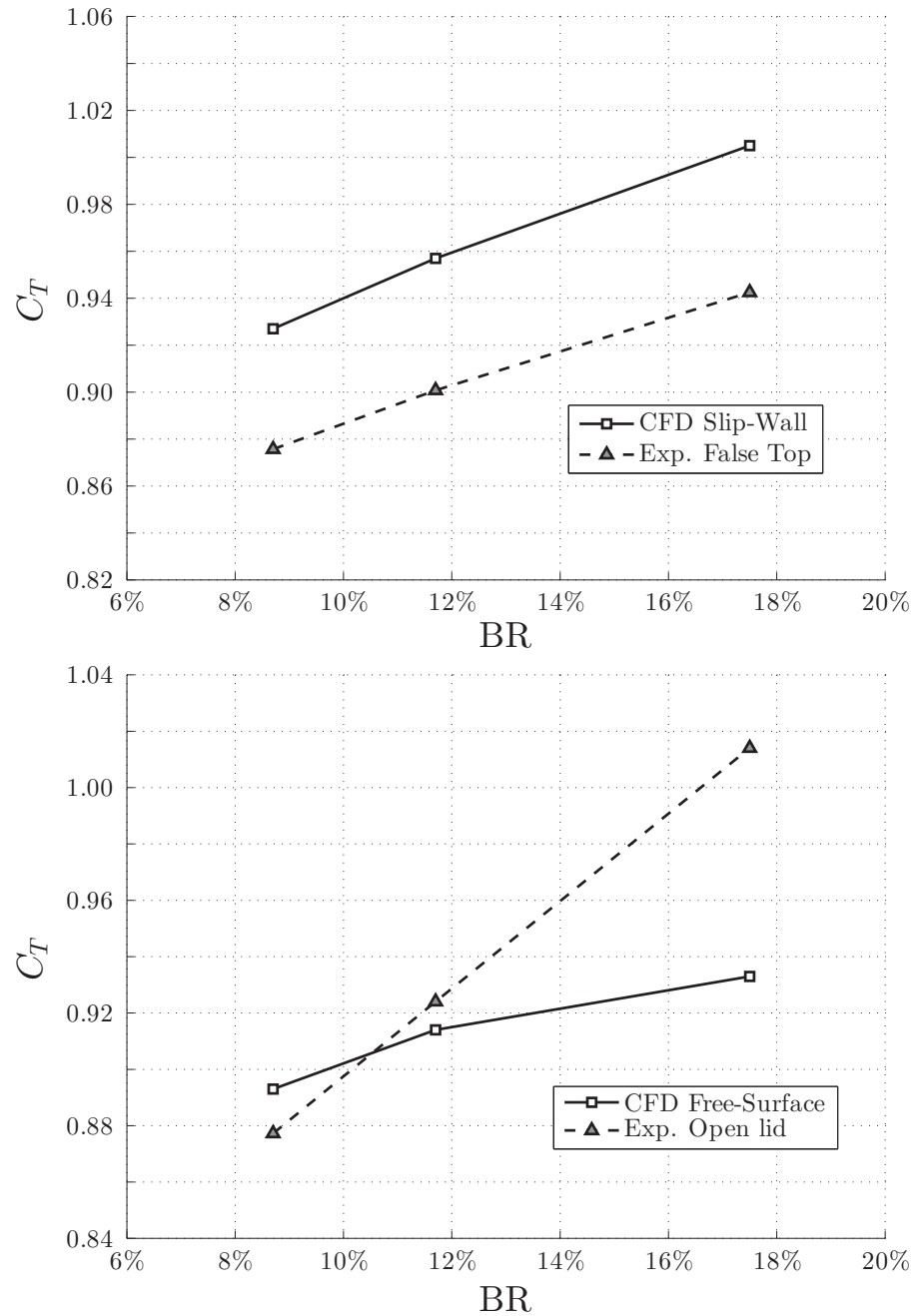


Figure 2.26: Comparison of experiments and porous disc CFD results, showing how the C_T varies with increasing blockage, for slip wall (top) and free surface (bottom) cases

2.6.2 Axial Rotor Experiments vs CFD

Figure 2.27a compares the experimental values of C_P to those obtained by CFD simulations for $\lambda=3.0$, 3.5 and 4.0. Both steady state and transient simulations

predicted higher overall performance values compared to the experimental results, the transient simulations being the highest. It is clear from both experiments and CFD simulations that the peak performance value is in the consistent range $\lambda=3.6$ - 3.7. As expected, the largest discrepancy between CFD and experimental results happens at λ lower than the peak performance point.

The interaction between the rotational and stationary domain happens through communication between domain interfaces. At low λ , due to the lower rotational speed, the rotor blades experience higher angle of attacks than those at the peak performance point and beyond. Due to this, the flow detaches from the blades and the rotor experiences stall. In this stall regime, a detached wake structure is formed behind the blades. The turbulence behaviour of this wake structure is quite different than that at higher λ . The information of this detached wake structure which starts in the rotational domain must be accurately conveyed to the stationary domain for the correct wake structure to occur at low λ . Due to interpolation errors and/or sudden changes in the element sizes, the information may be only partially transferred and cause an artificially smoother wake behind the turbine. This will cause the performance of the turbine at such low λ to be predicted to be higher than actually is.

The other possible explanation for this large discrepancy between the CFD and experimental results at $\lambda=3.0$ may be due to hysteretic behaviour of the blade, which may not be captured accurately in the current CFD simulations. In the stall regime, the current performance of the blades is very much dependent on the previous state they were in. If the blades were in favourable flow conditions prior to reaching their current state of flow, their performance would be better compared to having prior flow conditions which were inferior, i.e. increasing the angle of attack from a lower angle of attack would yield better performance values than decreasing the angle of attack to the current one. This hysteretic behaviour may be another cause of the difference between the measured and calculated values of power in low λ . Even ‘steady’ stall conditions, particularly in the laminar flow regime at the low Re experienced on the blades is notoriously difficult to predict accurately. This behaviour wasn’t noticed during the experimental campaign, although it was not directly addressed.

At $\lambda=3.5$ and 4.0, the steady state and transient results show about 5% and 9.5% higher performance values than measured. This difference may be due to the efficiency of the mechanical set-up during the experiments. Another possibility could be that the actual rotor may have a higher roughness on the blade surfaces than

the simulated one. The experimental rotor results are calibrated taking into account shaft and belt friction, but it may still present error, specially at lower torque values at lower λ .

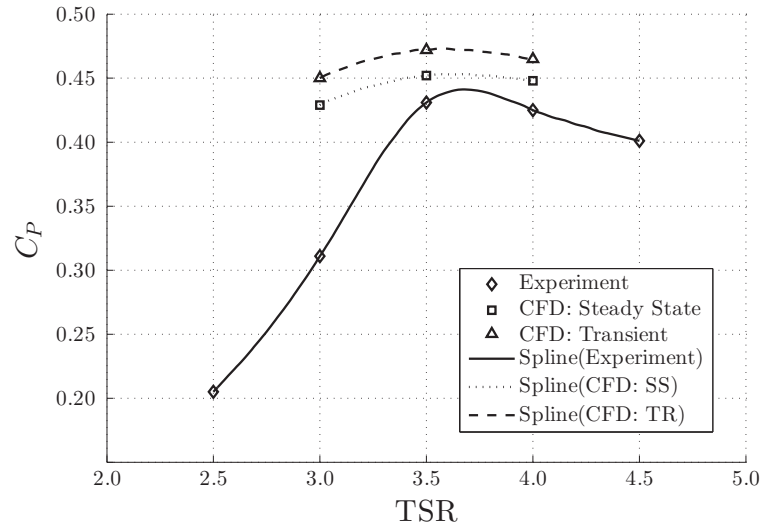
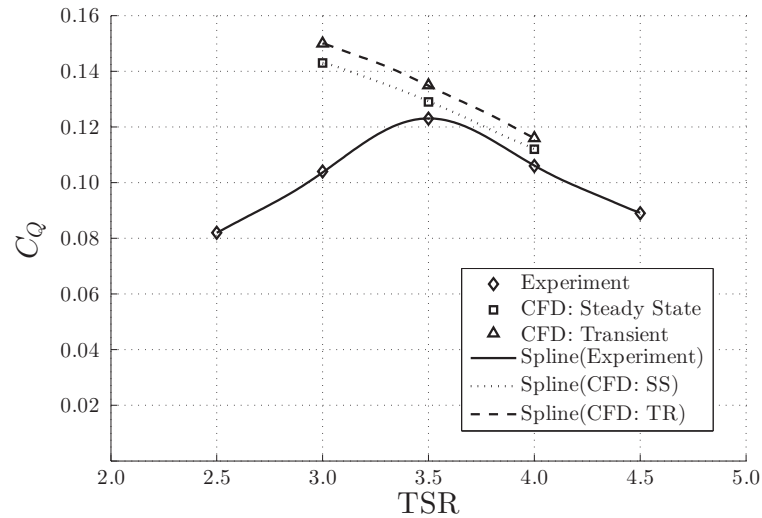
(a) C_P results(b) C_Q results

Figure 2.27: Experimental and CFD results for axial rotor

2.6.3 Porous Disc vs Axial Rotor

One of the objectives of this work was to compare the use of porous discs to an actual turbine rotor for deriving correction curves for thrust and power in blocked channels. The comparison was made based on performance values obtained using CFD

at three blockage ratios for the 21.9 cm diameter axial rotor and a 21.9 cm diameter porous disc. It was not possible to obtain experimental values at varying blockage ratios without significant redesign to the rotor rig mount. The CFD simulations were run until the maximum power point was reached and subsequently compared to 2D theoretical values on a thrust and power coefficient basis.

The values tabulated in Table 2.8 show that the thrust and power values agree relatively well between the porous disc simulation and the actuator disc theory. This result is inline with all of the previous validation work presented in Section 2.3.

The computed thrust and power for the axial rotor, however, is lower at each BR. This result is not unexpected given the fact that the efficiency of the axial rotor was limited by design constraints (use of thick blade sections) and by its small scaling (Reynolds effects).

What is more important for this study is to compare how the performance changes as the amount of channel blockage is varied. Table 2.9 provides a comparison between the rotor, porous disc simulations and AD theory on a percent change basis. These results show that both thrust and power for the axial rotor are much less affected by channel blockage compared to the porous disc or predictions made using AD theory. This outcome leads to the conclusion that the thrust and power corrections derived using actuator disc theory (and porous disc) likely represents an upper bound for real rotors. The actual boost in power for a physical turbine placed in a blocked channel will vary depending on the turbine's design.

BR	Axial Rotor CFD		Porous Disc CFD		2 AD Theory	
	C_T	C_P	C_T	C_P	C_T	C_P
0.087	0.791	0.426	1.118	0.730	1.215	0.708
0.116	0.808	0.441	1.260	0.780	1.343	0.757
0.175	0.848	0.473	1.624	0.948	1.697	0.890

Table 2.8: Comparison of C_T and C_P for a 21.9 cm rotor and disc

% Change	Axial Rotor CFD		Porous Disc CFD		2 AD Theory	
	% ΔC_T	% ΔC_P	% ΔC_T	% ΔC_P	% ΔC_T	% ΔC_P
0.087 to 0.116	2	4	7	7	11	7
0.116 to 0.186	5	7	29	22	26	18

Table 2.9: Comparison of C_T and C_P for a 21.9 cm rotor and disc on a percentage change basis

2.7 Conclusions

Results from experiments and CFD simulations for porous disc and rotor rig effectively show a boost in thrust and power with increasing blockage, with and without the inclusion of free surface effects.

Discrepancies in results between CFD and experiments on porous disc were found. The flume tank experiments showed a small increase in thrust when free surface effects are considered, as blockage increases. In contrast, simulations found that allowing the free surface to deform had the effect of decreasing C_T on the porous disc, compared to a slip wall set up. These differences could be explained mainly due to the wave observed right in front of the porous disc, which increases as Fr increases, affecting the effective inflow velocity through the disc. Since C_T is proportional to U_∞^2 , a small disturbance in velocity has an appreciable impact on C_T . This phenomenon will be assessed in future studies, as well as the impact on tip immersion on thrust and power coefficients.

CFD simulations also showed that a turbine foundation could have a significant impact on turbine performance. The impact of the turbine foundation was shown to be directly coupled to the shape of the structure and its interaction with the turbine. A streamlined structure placed in the plane of the rotor (extreme case being a duct) would be more effective at increasing the power produced by a turbine when compared to a truss type structure for example, even though both foundations may occupy a similar cross-sectional flow area.

Results from CFD simulations and experiments on an axial rotor were in good agreement in terms of predicting the peak power point. Overall, the CFD predicted higher performance values with the largest discrepancy occurring at λ lower than the peak performance point. CFD simulations were subsequently used to derive performance values for a range of blockage ratios.

The impact of channel blockage on an axial rotor was compared to that of a porous disc as well as theoretical values. These results showed that both thrust and power for the axial rotor were less affected by channel blockage compared to the porous disc or predictions made using actuator disc theory. This outcome leads to the conclusion that the increase in thrust and power derived using actuator disc theory (and porous discs) for increasingly constrained channel likely represents an upper bound for real rotors. The actual boost in power for a physical turbine placed in a blocked channel will vary depending on the turbine's design.

In addition to addressing the key project objectives, it was shown through this work that using porous disc in place of momentum sinks for simulating idealized turbines is a valid and more straight forward to implement. Since the momentum loss through a porous region is a function of the velocity, this modeling method is better suited to cases where an actuator disc may encounter non-uniform flows such as for array modeling. Future work in larger facilities could confirm these results without the confounding effects of low Re for the rotor testing.

Chapter 3

PIV/Flume-Tank Experimental Study of 2D Hydrofoil Coefficients at Low Re

Authors: Italo Franchini¹, Michael Shives¹, Michael McWilliams¹, Curran Crawford¹

¹ Dept. of Mechanical Engineering, University of Victoria, BC

To be submitted

The author of this thesis contributed with the experimental work, instrumentation development, hydrofoils optimization and testing using PIV, as well as XFoil predictions

3.1 Abstract

The present work aims to experimentally determine the performance of four candidate hydrofoils for use in later rotor testing. The experiments were carried out in a recirculating flume tank over the range of low Reynolds numbers expected ($Re = 6 \times 10^4 - 1 \times 10^5$) on the small scale rotor ($D \approx 150$ mm). The foil sections were produced using the same fused deposition modeling (FDM) used on the blades to replicated the natural (and beneficial) surface roughness of the FEM process. The majority of experimental polar curves available in literature are for relatively high Re, hence the necessity to develop and implement a reliable method to measure the lift and drag with an acceptable confidence level at low Re. Even for cases within the operational Re, the particular characteristics of the flume tank such as turbulence intensity and

the hydrofoil surface roughness will impact the performance in ways that cannot be predicted without a dedicated experimental study. Therefore, an automated 2D hydrofoil test rig was designed to test any foil using Particle Image Velocimetry (PIV). A numerical data reduction method processed the time-averaged flow field to obtain the experimental C_l and C_d . The second objective was to compare experimental results with numerical performance predictions from XFoil, a standard viscid-inviscid coupled method. The results are analyzed in order to find the most suitable numerical parameters for reliable performance prediction. It was found adding a numerical trip at a certain chordwise distance good agreement was achieved.

3.2 Introduction

The study of low Reynolds number (Re) airfoils is of special interest for flume and wind tunnel testing of small scale tidal and wind turbine rotors [17]. Blade design plays a fundamental role in these devices, and although model and full-scale on-blade Re cannot be matched, wake behavior is well represented, as studied by Vermeer, Sørensen, and Crespo [42] using an horizontal axis wind turbine and Harrison, Batten, Myers, and Bahaj [43], who compared CFD simulations with experiments for predicting the far wake of a HATT. It is however critical to select and characterize airfoils and hydrofoils that have a satisfactory performance at low Re in order to define a reasonably performing rotor. Due to the flume tank's dimensions in the authors' facility (specified in section 4.5.1) only small scale prototypes can be tested, where the usual range of chordwise Re varies from 6×10^4 to 1×10^5 . The approach and results of the current work are equally applicable to air and water tunnels, assuming the Re and turbulence characteristics are matched. Previous studies [44]–[47] have not adequately covered the Re range required for these types of small-scale rotor tests.

The aims of this paper can be broken down into two major parts. The first objective is to accurately obtain coefficients for four different candidate foil shapes. Two of these foils are taken from literature [48]; the other two were obtained after performing a numerical optimization. The hydrofoils are fabricated using a Fused Deposition Modeling (FDM) machine available in the Sustainable Systems Design Laboratory (SSDL), which is essentially a 3D printer that builds-up the model geometry in layers using extruded plastic. The flow field around the hydrofoil is captured using the Particle Image Velocimetry (PIV) technique and finally a data reduction method (ex-

plained in section 3.5.5) is used to obtain the lift and drag coefficients. This obviates errors associated with direct force measurements at the small force values present on the hydrofoil.

The second part of the paper involves obtaining acceptable performance predictions. The idea is to use medium-fidelity numerical methods easily used for design work to predict the polar curves with an acceptable accuracy level for the working conditions in our flume tank. These methods generally solve either the incompressible potential flow equation or compressible flow with small disturbances. Panel methods, point vortex solutions or coupled viscous/inviscid methods [49] are commonly used. The latter is the one utilized in this paper, embodied in the 2D airfoil code named XFoil, developed by Drela [28]. The idea is to compare the experimental results with XFoil predictions in order to find the most suitable numerical model parameters for future hydrofoil development. This work will only focus on varying two important variables: the e^n laminar–turbulent transition criteria and adding a numerical trip (x_{tr}) on the hydrofoils surface. In order to eliminate the laminar separation, several techniques have been developed to accelerate transition and improve performance at low Re [50]. By adding a trip (or any type of roughness) near the leading edge of the foil, the point where separation starts can be modified, leading to potential improvements in the final design, as shown in the work done by Gopalarathnam et. al [51]. The fabrication method and flow conditions suggest an earlier transition point, hence adding an artificial trip on the surface in the numerical simulation leads to better performance predictions. The goal is to find a suitable range of x_{tr} where predictions can be improved for future hydrofoil selection.

The next section presents the selection of the initial candidate foils, which will be used as a baseline for comparisons and optimization. Section 3.4 outlines the potential flow code employed and explains the optimization method to obtain new foil shapes. The experimental set-up and data reduction method are presented in section 3.5, including hydrofoil fabrication, water tunnel/PIV equipment description and numerical analysis of the flow field to obtain C_l and C_d . The final results and analysis can be found in section 3.6, where a comparison between literature, PIV experiments and predictions using XFoil are presented for the principal foils selection, following by a final summary of the work done in section 3.7.

3.3 Candidate Foils

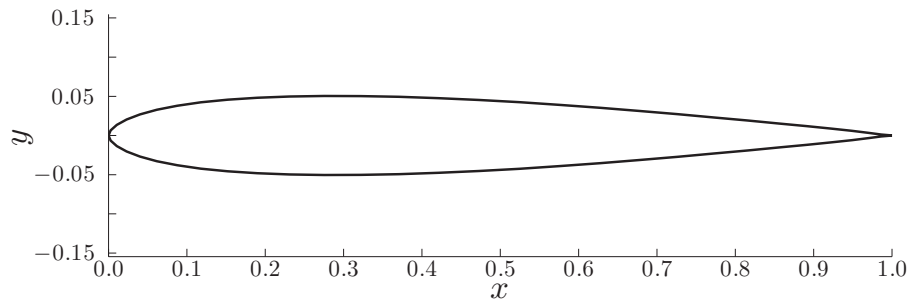
The ideal foil candidates were chosen based on how they performed at low Re. The main source of airfoil data was the University of Illinois at Urbana-Champaign (UIUC) [48]. After reviewing the performance of many different airfoils, it was decided to select the SD8020 and the NACA 2415, as shown in figure 3.1. Figure 3.2 shows the C_l and C_d of the SD8020 for a range of Re available from that dataset; figure 3.3 presents a similar dataset from the UIUC for the NACA 2415. Note that the UIUC data was obtained for 'clean' and smooth airfoils.

One of the main reasons to choose these airfoils is directly linked to the work done with our small scale rotor rig [17], specifically when blade design is considered. Due to the blades manufacturing method and small size, structural constraints were imposed in order to avoid blade deflection during operation in the water tunnel. The final decision was to limit the minimum hydrofoil thickness to 15%, hence the original SD8020 shape was resized to meet the minimum thickness requirements, as shown in figure 3.4b. After reviewing the literature it was found a possible better candidate (NACA 2415) which already has a thickness within the desired range.

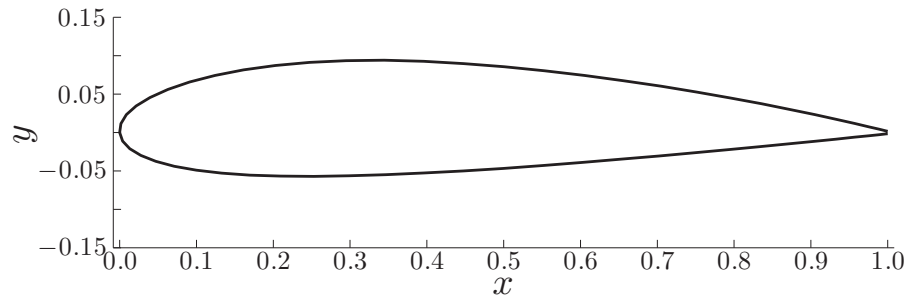
The other two hydrofoils considered in this study were obtained using numerical optimization, as explained in section 3.4. A final schematic of the candidate foils can be found in figure 3.4; the optimized foils are named NACA 2415-SSDL and SD8020-SSDL.

3.4 XFoil and Optimization method

The 2D airfoil code XFoil [28] applies a coupled method to resolve the flow around the foil. Boundary layer equations are used in the inner viscous region on the airfoil surface, coupled to a panel method used to solve the inviscid flow equations that govern the outer region. A finite trailing edge thickness correction is also added, together with viscous wake thickness treatment. An e^n free laminar-turbulent transition or fixed transition location augments the boundary layer formulation. The two solutions are matched through the displacement thickness δ /surface transpiration [52]. The primary advantage of using this method as compared to a full Eulerian CFD method is the large computational savings obtained from the solution method, including a convergence-acceleration scheme that improves convergence for flow with some separation. The method is generally accurate below stall, including for drag prediction,



(a) SD8020 airfoil shape



(b) NACA2415 airfoil shape

Figure 3.1: Final airfoil selection

but does progressively lose validity as the airfoil stalls owing to the assumed boundary layer profiles. For on-design rotor performance, the blade's hydrofoils should be operating below stall, so this is not expected to be a major limitation for the current task. Notwithstanding this primary limitation, XFOIL will be employed for all hydrofoil predictions throughout this paper, including as part of the aerodynamic optimization.

As mentioned before, part of this work includes an attempt to introduce new hydrofoil shapes that could yield better performance under specific conditions selected by the user. XFOIL includes user controlled design functionality, however a numerical optimization scheme was used in the current work. The optimization was performed using a recently developed script called XOPTFOIL developed by Prosser [53]. This program uses a particle swarm algorithm as a global optimization technique to find the best overall design, along with simplex algorithm for local search. A seed hydrofoil is used as the initial design and shape functions are introduced to deform the seed hydrofoil. The functions used in this work are called Hicks-Henne "bump" functions, originally presented by Hicks and Henne [54], [55] and further studied and compared against other parametrization techniques by Tashnizi *et. al* [56]. Every new airfoil

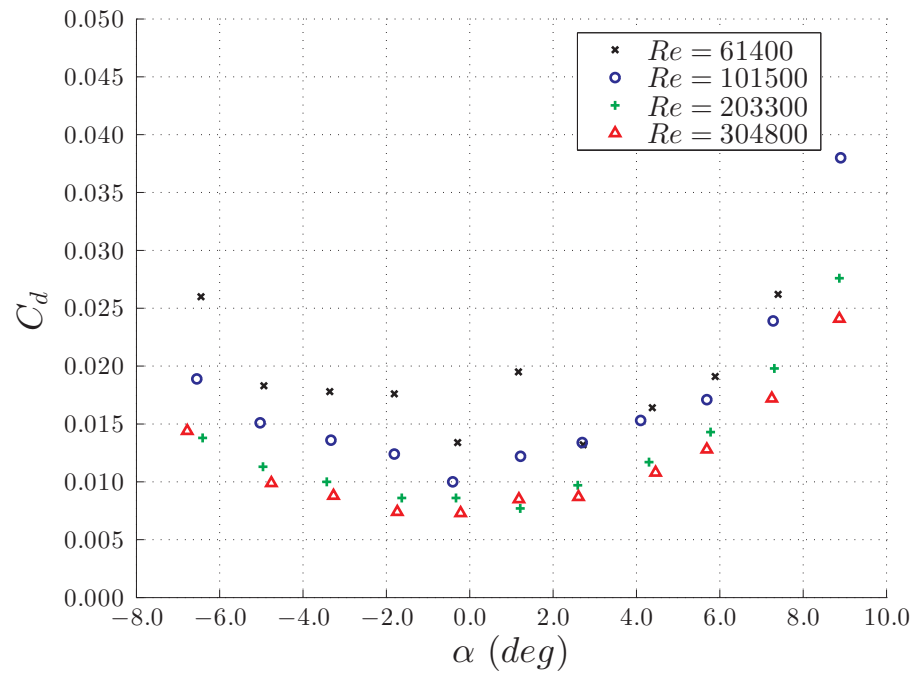
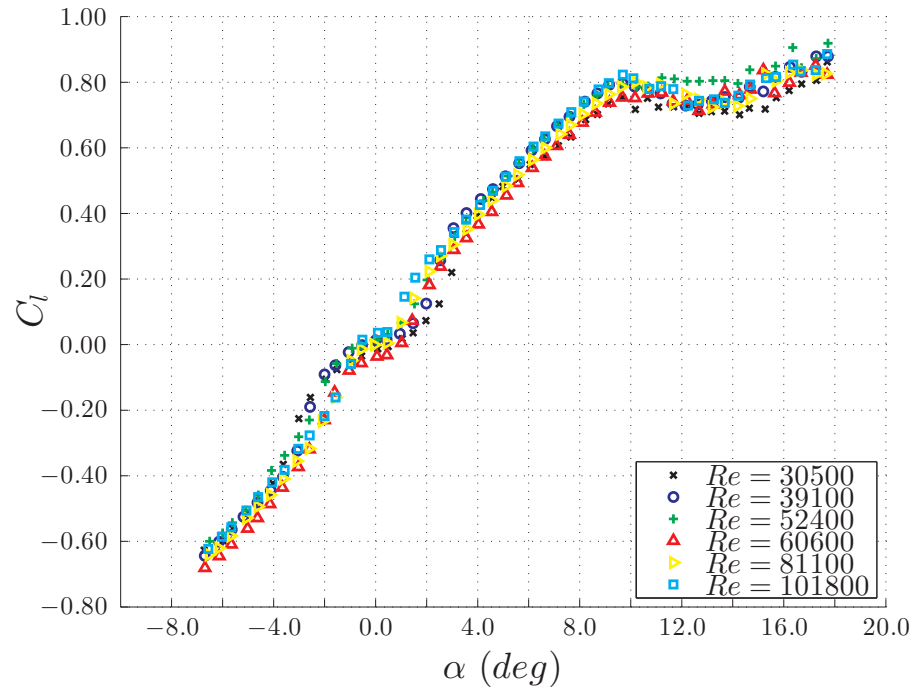


Figure 3.2: SD8020 airfoil data taken from UIUC

shape is evaluated using XFoil and the performance obtained is evaluated in the objective function. In this particular case, the objective function is defined by 5

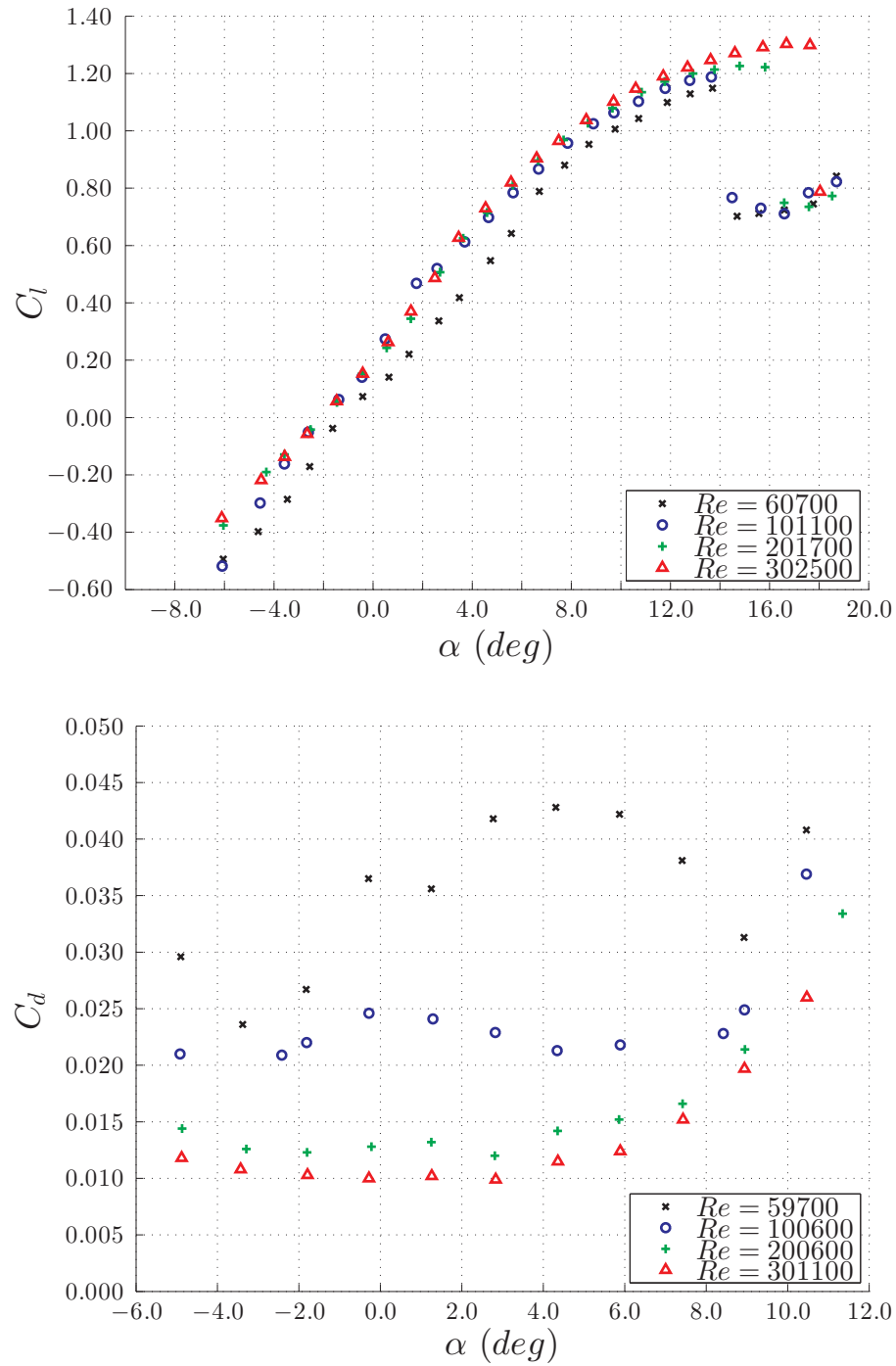


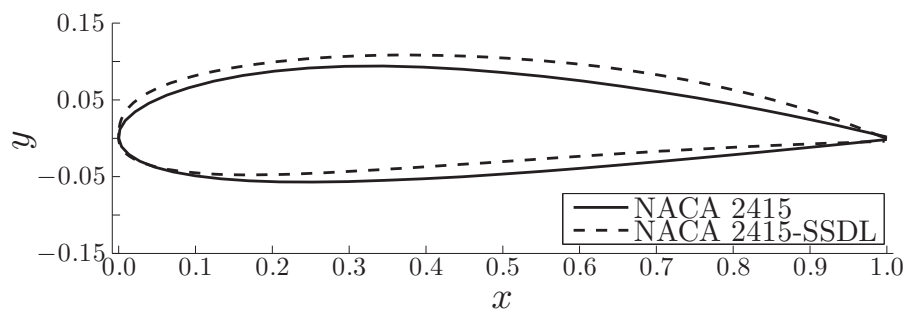
Figure 3.3: NACA2415 airfoil data taken from UIUC

angle of attack operating points at a given Re and the optimizer will attempt to maximize the glide ratio, given by C_l/C_d , averaged across those five points.

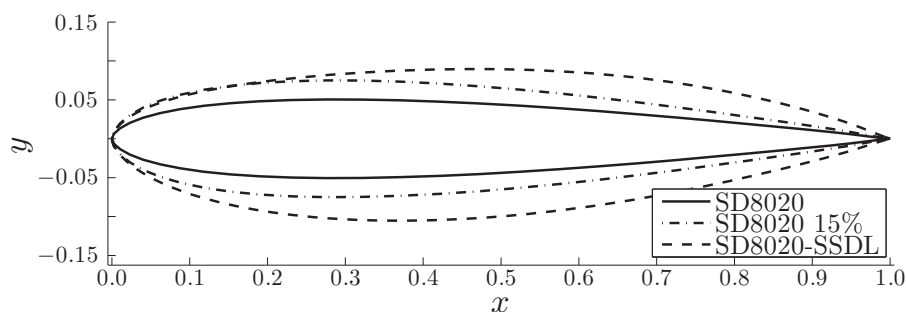
This optimization was initiated twice, using NACA 2415 and SD8020 15% shapes as seed hydrofoils. The operating points were set for $Re=6.2 \times 10^4$ and for $\alpha = 2^\circ, 4^\circ, 6^\circ, 8^\circ, 10^\circ$, which resulted in the objective function from equation 3.1

$$\begin{aligned} \max \quad & \left(\frac{C_l}{C_d} \right) \Big|_{\alpha=2^\circ} + \left(\frac{C_l}{C_d} \right) \Big|_{\alpha=4^\circ} + \left(\frac{C_l}{C_d} \right) \Big|_{\alpha=6^\circ} \\ & + \left(\frac{C_l}{C_d} \right) \Big|_{\alpha=8^\circ} + \left(\frac{C_l}{C_d} \right) \Big|_{\alpha=10^\circ} \end{aligned} \quad (3.1)$$

The reason for choosing these operational points is because it was desired to increase the hydrofoils performance for the lowest Re , consequently decreasing Re dependency for the entire desired range as performance typically improves with Re .



(a) NACA 2415 family



(b) SD8020 family

Figure 3.4: Optimized airfoil shapes

3.5 Experimental Method

The overall method included fabrication of hydrofoil test articles and testing with PIV in the water tunnel, as detailed in this section.

3.5.1 FDM Airofil Fabrication

The final foil selection were fabricated using the Fortus 400mc FDM machine at the SSDL with a total chord length of 70 mm. This machine builds parts layer-by-layer from the bottom up by heating and extruding thermoplastic filament, allowing the manufacturing of real parts in-house with multiple production-grade thermoplastics, providing great accuracy and repeatable builds. Building material and tip sizes are important parameters that will define the quality and roughness of the final part, among other significant properties. The available materials at the SSDL are the ABS-M30 and polycarbonate (PC). The ABS is versatile and tough, providing a slightly smoother finished when compared with the PC, which exhibits better mechanical properties.

The tip selection affects the layer thickness, which have a direct impact on the surface finish. Previous campaigns [17] manufactured blades using the smaller tip available (T10), resulting in a slice height of 0.0127 *mm*. The combination of using this tip and the ABS-M30 material resulted in smooth blades that turned out to have a low performance when tested with the rotor rig. It was decided to change the tip to T12 and the model material to PC. This resulted in a higher slice height, which combined with the new selected material, delivered a rough finish surface and a better mechanical performance.

3.5.2 Water tunnel

The test campaigns were conducted at the University of Victoria Fluids Research Lab flume tank. The test section of the water tunnel has a cross section of 0.45×0.45 m and a useable length of approximately 2.5 m. The flow is driven by a single-stage axial flow propeller pump delivering a maximum flow rate of 405 L/s. The pump shaft RPM is controlled using a Toshiba VT130H7U6270 frequency controller that allows inflow speeds up to 2 m/s.

The inflow to the test section consists of a perforated plate, honeycomb section, 5 high-porosity screens and a 6:1 contraction section. Downstream of the test section the flow is diverted by turning vanes in the return plenum into the return flow pipe located underneath the test section. The ambient turbulence level is approximately 1.0 %. The tunnel can be run both with and without top plates. For the current work, the top plates were used and tunnel completely full to avoid free-surface effects. In this configuration, the maximum tunnel speed is 2 m/s.

For this work three different free-stream inflow speeds (U_∞) were selected. Since the only parameter that can be controlled is the pump frequency, it was decided to use for the experiments frequencies of 25, 35 and 40 Hz. Using PIV images, as detailed in section 3.5.4, the time-averaged velocity field was obtained at the inlet of the flume's test section for every case, resulting in $U_\infty = 0.887, 1.243$ and 1.419 m/s which correspondingly leads to $Re=62874, 88023$ and 100598 .

3.5.3 2D Airfoil Test Rig

The test rig apparatus consists of a rectangular acrylic box that allows optical access through the sides and bottom. The edges of the box are beveled to create sharp entry on all four sides. The hydrofoil is placed vertically inside the bounding box and secured by an alignment shaft. The initial design was developed by Root [18]. It was redesigned so that the hydrofoil mounting shaft could be automatically controlled by a Parker HV-233-02-10 stepper motor. This modification allows the user to accurately set the desired angle of attack α using a GUI. Previous campaigns were executed by manually setting the angle of attack, leading to considerable errors in the collected data and considerable time requirements for a full range of angles of attack to be traversed. The final test rig is shown in figure 3.5.

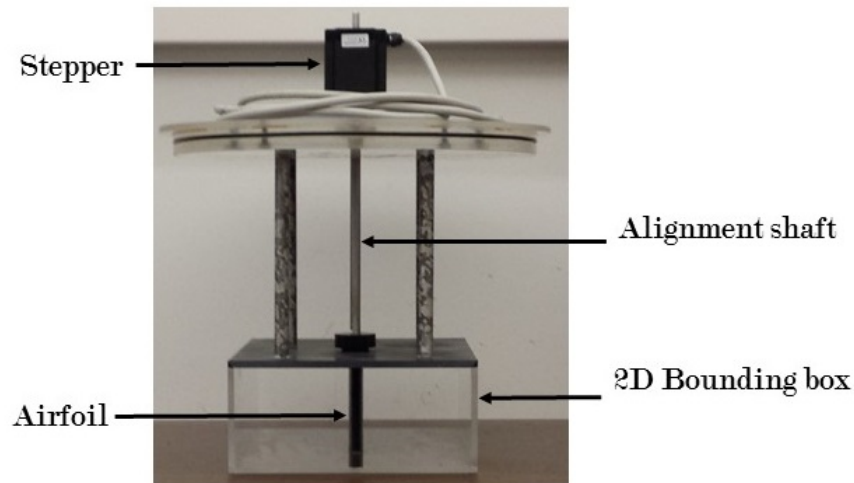


Figure 3.5: 2D Airfoil Test Rig as viewed from upstream

Initially the SD8020 15% was tested only for positive angles of attack, since it is a symmetric foil and the interest was mainly on the positive α side. Thus, the 2D test rig was set for $\alpha = 0^\circ, 2^\circ, 4^\circ, 8^\circ, 10^\circ, 14^\circ, 18^\circ$. For each α a set of 300 PIV images were

taken to obtain the time-averaged flow field. For the rest of the foils, i.e. SD8020-SSDL, NACA2415 and NACA2415-SSDL, the test included also negative angles of attack, with a full tested range of $\alpha = -18^\circ, -14^\circ, -10^\circ, -8^\circ, -4^\circ, -2^\circ, 0^\circ, 2^\circ, 4^\circ, 8^\circ, 10^\circ, 14^\circ, 18^\circ$.

3.5.4 PIV Setup

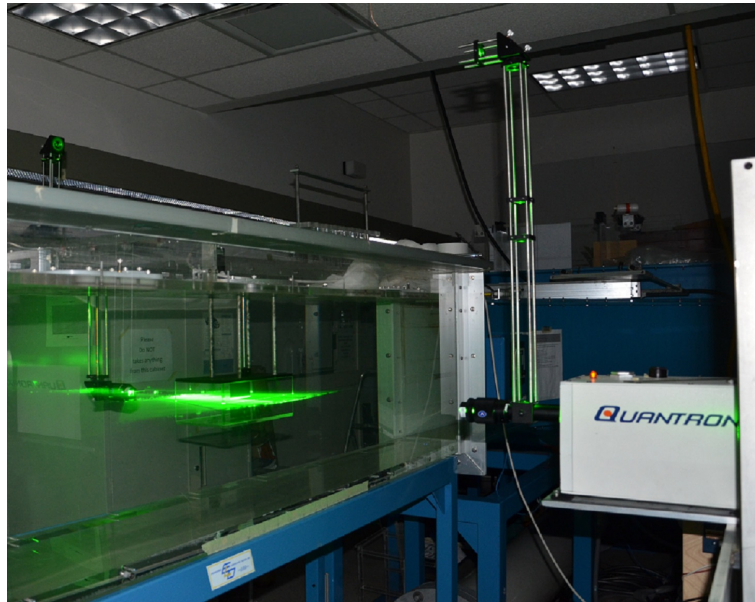
The PIV setup consists of a Photron Fastcam APX RS camera with a 50 mm focal length lens that allows the capture of a wide field of view around the hydrofoil. The camera was mounted on a carriage assembly beneath the test section. The laser was located on top of an optical table, mounted on rails that can accurately position the system for the desired height and distance parallel to the flume. The laser model is a Quantronix Darwin-Duo that operates at a wavelength of 527 nm. The horizontal laser sheet setup is explained in section 3.5.4. The system was configured to capture double-frame images and 300 images were taken to ensure statistical convergence of the post processed mean velocity field. The image post processing was done using the commercial software Davis v7.2.

Laser Double-sheet

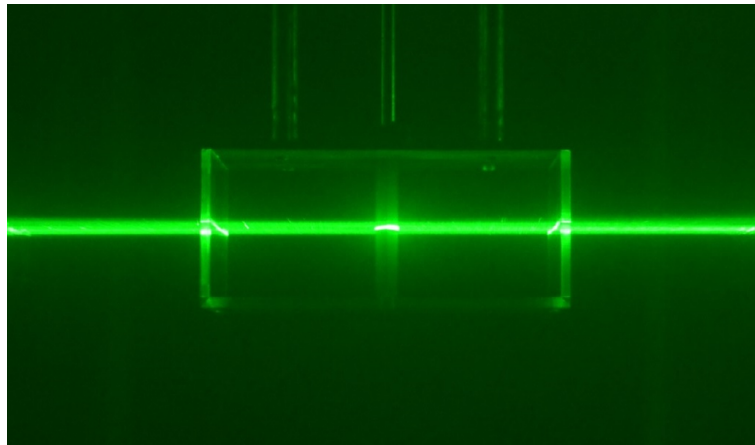
Previous experiments carried out to validate the data reduction method applied PIV using a single laser sheet due to the available optical configuration. This original setup meant the flow could only be fully illuminated on one side of the hydrofoil, creating a shadow region on the other side. This problem was addressed by taking two data sets for each angle of attack, starting with positive α followed by the corresponding negative angles. The resulting time-averaged flow fields were later combined to obtain a complete flow field. Only symmetric hydrofoils were considered in those initial test campaigns, and was one of the main reasons to initially choose the SD8020. This method was employed by Ragni *et al.* [57] showing good success, however it was very tedious and time consuming.

The new setup consists of a beam splitter and reflecting mirrors that bypass the water tunnel cross section, creating an adjustable laser sheet on both sides of the hydrofoil at the same time, as shown in figure 3.6. By carefully adjusting the horizontal sheets to the same height it is possible to resolve the complete time-averaged flow field for every single α . This major improvement along with the automation of the test rig eliminated the uncertainty produced by stitching the vector fields and

drastically decreased the data acquisition time.



(a) Experimental setup



(b) Double sheet around airfoil

Figure 3.6: Laser double sheet for PIV

3.5.5 Data Reduction Method

The aerodynamic coefficients were obtained using the momentum integral and wake rake methods to find lift and drag, respectively, as detailed in the following. These non-contact, indirect methods are preferable given the small hydrodynamic forces present on the hydrofoil section. The methods rely on post-processing 2D control

volumes around the hydrofoil section, as seen in the experimentally obtained time-averaged PIV data for each angle of attack setting.

Pressure Fields

The momentum integral and wake rake method require the pressure along the control volume boundaries. There are several documented methods for determining the pressure field from PIV data and a good summary is given in Charonko [58]. The space marching method of Bauer and Koenigter [59] seems to be a popular option and was adapted in both Van Oudheusden et al [60] and Ragni *et. al* [57]. There are two steps in obtaining the pressure field. The first involves pressure gradients calculations using a time-averaged 2D velocity field ($x - y$ plane). The incompressible RANS equations were used, assuming that the out of plane velocity w is 0, thus the partial derivative of any variable in the z direction is also 0. Canceling terms, the pressure gradient equations become:

$$\begin{aligned} \frac{\partial p}{\partial x} = & \mu \left(\frac{\partial^2 u}{\partial x^2} + \frac{\partial^2 u}{\partial y^2} \right) - \rho \left(u \frac{\partial u}{\partial x} + v \frac{\partial u}{\partial y} \right) \\ & - \rho \left(\frac{\partial \overline{u'u'}}{\partial x} + \frac{\partial \overline{u'v'}}{\partial y} \right) \end{aligned} \quad (3.2a)$$

$$\begin{aligned} \frac{\partial p}{\partial y} = & \mu \left(\frac{\partial^2 v}{\partial x^2} + \frac{\partial^2 v}{\partial y^2} \right) - \rho \left(u \frac{\partial v}{\partial x} + v \frac{\partial v}{\partial y} \right) \\ & - \rho \left(\frac{\partial \overline{v'u'}}{\partial x} + \frac{\partial \overline{v'v'}}{\partial y} \right) \end{aligned} \quad (3.2b)$$

Where p is the pressure, μ is the dynamic viscosity and ρ is the fluid density. The velocity and Reynolds stress gradients were evaluated using second order central differencing.

The obtained pressure gradient is subsequently integrated to obtain the pressure field. The method employed uses a 5-point stencil, as shown in figure 3.7. The pressure at point C for interior nodes is then calculated using:

$$\begin{aligned} p_C = & \frac{1}{8} \left[\left(\left. \frac{\partial p}{\partial x} \right|_2 - \left. \frac{\partial p}{\partial x} \right|_3 \right) \Delta x + \left(\left. \frac{\partial p}{\partial y} \right|_4 - \left. \frac{\partial p}{\partial y} \right|_1 \right) \Delta y \right] \\ & + p_1 + p_2 + p_3 + p_4 \end{aligned} \quad (3.3)$$

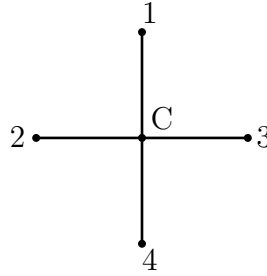


Figure 3.7: 5-point stencil

The stencil is modified for nodes on the side of the domain and the corners. The finite difference stencil provides one equation for each node and the equations can be represented as a linear algebra matrix system, i.e. $Ax = b$.

To improve the accuracy of the pressure field in the interior of the domain, the Bernoulli equation was used to set boundary conditions on the inflow and upper and lower boundaries, similar to the work done by Ragni *et. al* [57], who used an isentropic pressure solution for all regions outside the shear layers.

Momentum-Integral

The final c_l was calculated using the momentum-integral approach. In previous analysis it was found that both momentum-integral and circulation-integral methods resulted in similar c_l . However, the circulation-integral is strictly valid for irrotational flows, but since part of this path passes through the viscous/separated wake region it may contribute to some error. Therefore the final results were calculated using momentum-integral.

The total force applied to the flow by a body enclosed by a control surface can be determined by numerical integration of the pressure, momentum flux, viscous shear and Reynolds stress terms along the surface boundary. The force terms are found directly from the RANS equations as follows:

$$\vec{F} = \oint_A (\sigma - \rho \vec{u}\vec{u}) \cdot \hat{n} dA \quad (3.4)$$

where σ is the symmetric stress tensor composed of pressure, shear and Reynolds stress terms:

$$\sigma = -p\delta_{ij} + \mu \left(\frac{\partial u_i}{\partial x_j} + \frac{\partial u_j}{\partial x_i} \right) - \rho \overline{u'_i u'_j} \quad (3.5)$$

The corresponding $x - y$ set of integrals can be evaluated numerically along the

user-defined integration path. A trapezoidal integration was used for each path element and the total path integral is simply the sum from all the path elements.

The c_l was found to be quite stable with varying control volume dimensions. The results showed that the ideal control volume should be taken as far as possible from the hydrofoil, close to the edges of the vector field in every direction and as far as possible in the wake region. The pressure component was the largest contributor of the total c_l and the shear and Reynolds stress components were typically negligible.

Jones Wake Rake Method

The momentum integral method produced reasonable results for C_l but failed to provide reasonable values for C_d . The lift is typically two orders of magnitude (at low α) larger than the drag force and is therefore less sensitive to noisy input data and truncation errors. The calculations are not as robust for the drag since the signal-to-noise ratio is poorer and cumulative truncation errors are likely of similar magnitude to the drag. Van Oudheusden [60] and Ragni [57] noted similar difficulties in applying the momentum integral method to finding the drag force.

The wake rake method from Houghton and Carpenter [61] makes several assumptions about the flow which allow the drag to be determined by an integration carried out over just the wake behind the hydrofoil. The method is essentially similar to the momentum approach, but all shear and Reynolds stress terms are neglected. It is assumed that along the upper and lower integration path boundaries there is no streamwise momentum flux. This method is widely used physically in wind tunnel experiments and is known to provide accurate results for low α where there is little to no flow separation and almost no head losses due to mixing in the wake.

3.5.6 Predictions Considerations

The results obtained are compared to XFoil predictions; the main interest lies on finding the right numerical parameters in order to accurately predict future hydrofoil polar curves a priori. To accomplish this, two XFoil parameters are considered in this study: the critical transition amplification factor (N_{crit}) and the addition of a trip at a given location on the suction side of the foil (x_{tr}). The N_{crit} can be approximated using Drela's correlation [62] for a free stream turbulence level τ , given by $N_{crit} = -8.43 - 2.4 \ln \tau$, but a sensitivity analysis will be performed for a wide range of values, going from $N_{crit} = 3 \rightarrow 12$.

The second parameter to be considered is of particular importance for low Re , since a separation bubble typically appears in the boundary layer that has an impact on the overall performance of the hydrofoil. This separation bubble is caused by an adverse pressure gradient away from the leading edge that produces a separation of the still-laminar boundary layer, followed by a transition to turbulence regime in the separated shear layer and culminating in a reattachment of the turbulent shear layer, as thoroughly studied by Arena and Mueller [63]. Therefore, by adding a trip on the hydrofoil’s surface, the transition point can be numerically modified and hence the behavior (or absence) of the separation bubble altered. It is expected that a suitable range of trip location can be found to improve the predictions, reflecting the physical surface of the hydrofoils which is relatively rough owing to the FDM production process. Note that at low Re rougher surfaces leading to earlier transition can improve overall foil performance by delaying stall.

It is important to remark that these numerical parameters are never universal, due to the complex flow phenomenon and will vary with foil shapes, angles of attack, flow conditions and surface roughness, as noted by Arena and Mueller [63] and Gopalarathnam et. al [51]. Nevertheless, the findings should help guide future hydrofoil development for low Re testing.

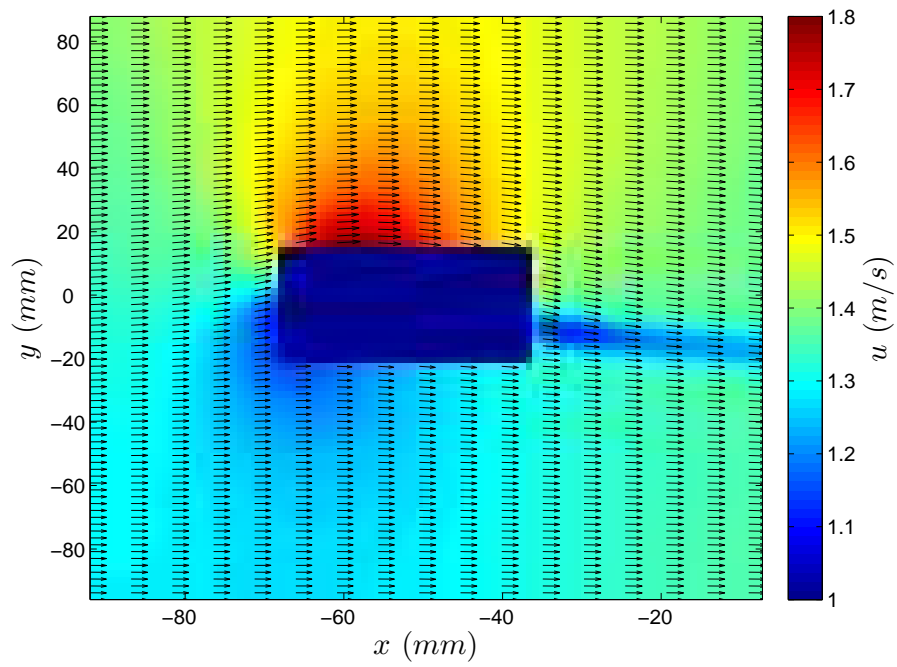
3.6 Results and Discussion

The NACA2415 foil results are presented first in section 3.6.1. As the only hydrofoil that hasn’t been modified from past studies, in thickness or shape, it becomes the ideal candidate to check whether the experimental results provides reasonable and accurate results or not compared to literature.

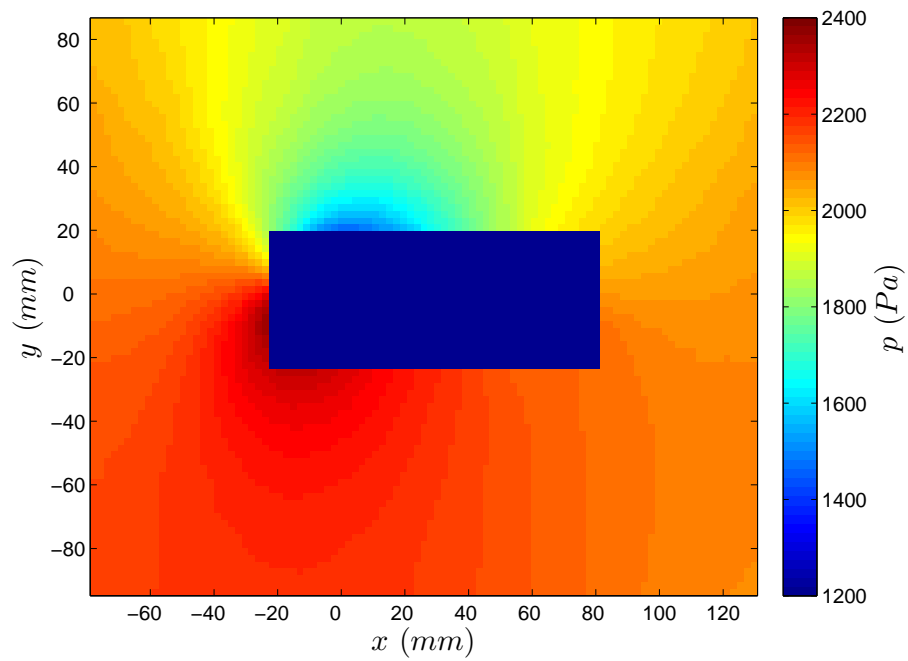
3.6.1 NACA 2415 SSDL vs UIUC

PIV time-averaged flow field results were analysed using the data reduction method to obtain C_l and C_d and compared against the UIUC database, as shown in figure 3.9.

These results show a very good agreement between the collected data and the database used as the main reference. From figure 3.9a it can be seen that the C_l trend is followed closely for similar Re and both results show very similar stall regions, although the SSDL results suggest a higher maximum C_l , which may be explained



(a)



(b)

Figure 3.8: Example of a post-processed PIV result showing the time-averaged velocity field (a) and the obtained pressure field (b) for the NACA2415-SSDL at $\alpha = 10^\circ$

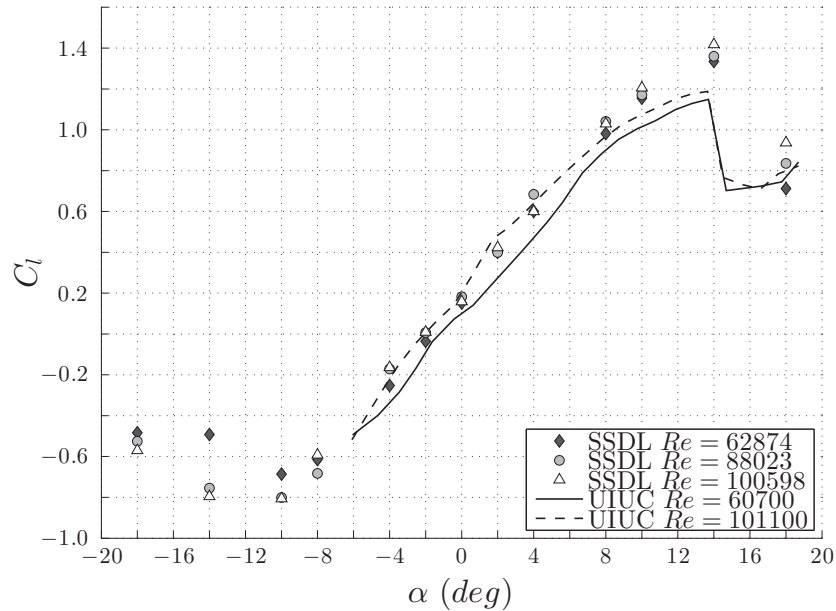
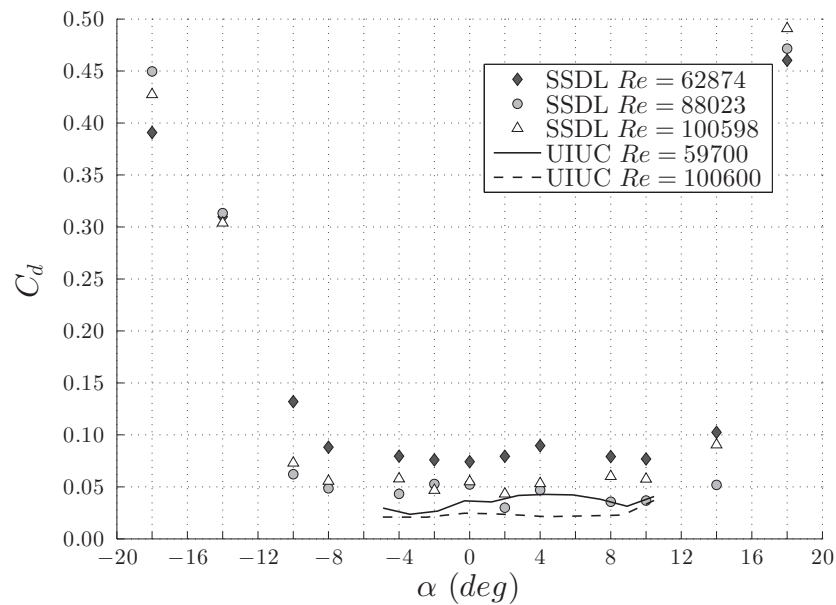
(a) C_l vs α (b) C_d vs α

Figure 3.9: NACA2415 PIV v/s UIUC results

due to the higher turbulence intensity in the water tunnel ($\approx 1\%$) vs the UIUC wind tunnel ($\approx 0.1\%$). The C_d obtained in this experiment and illustrated in figure 3.9b shows a higher trend for similar Re, which can also be expected due to differences in surface roughness of the hydrofoil and again the flume turbulence level. The layer-by-layer printed hydrofoils have an intrinsically higher roughness than the ones used

by UIUC. Additionally, the C_d beyond stall increase rapidly, as expected, but the validity of the wake rake method becomes questionable well into stall.

It is interesting to notice that for the various datasets all experience a pronounced "drop" in the lift coefficient going into stall, which fully agrees with the findings by Lee *et. al* [64]. In that work, the long trailing edge separation bubble that causes a collapse of the suction peak, manifests in a sudden drop in C_l . Therefore, the method employed at the SSDL provides a reliable experimental procedure.

3.6.2 NACA 2415 and SD8020 15% XFoil Predictions

With the confidence that the method employed delivers reasonable results, it is now possible to use XFoil to predict the performance of these hydrofoils as accurately as possible in order to find the ideal input parameters. This study considers mainly two variables that will be modified in XFoil to represent as close as possible the nature of the work flow and the hydrofoil manufacturing process, as explained in section 3.5.6. An initial sensitivity analysis was performed by varying the critical transition amplification factor N_{crit} from $n = 3 \rightarrow 12$, showing noticeable differences when free transition was assumed. These results couldn't fully match the experimental results, although it is worth mentioning that lower N_{crit} resulted in better predictions, as expected by Drela's N_{crit} correlation [62]. However, the simplicity behind XFoil's laminar-turbulent transition model for this case resulted in a poor predictive capability.

When the x_{tr} parameter was studied, the results were greatly improved as shown in figures 3.10 and 3.11. Due to the large number of plots generated during this investigation, this paper only presents the sensitivity analysis when varying x_{tr} , given the fact that it finally led to better predictions.

Two major results were found: when adding a trip on the surface between $x_{tr} = 0.1 - 0.2$ on the suction side of both hydrofoils, the lift curve slope in the pre-stall region satisfactorily agrees with the experimental results for the three different Re tested. The NACA 2415 lift trend is found to be in very good agreement until the critical angle of attack, which is accurately predicted ($\alpha_{max} \approx 14^\circ$) but differs in the $C_{l_{max}}$. Care must be taken when using XFoil for predicting such maximum, since flow conditions, hydrofoil fabrication and transition point can vary at α_{max} , leading to the uncertainty shown before. The SD8020 15% also showed a good correlation with the SSDL experimental lift slope and also the stall region was within the expected

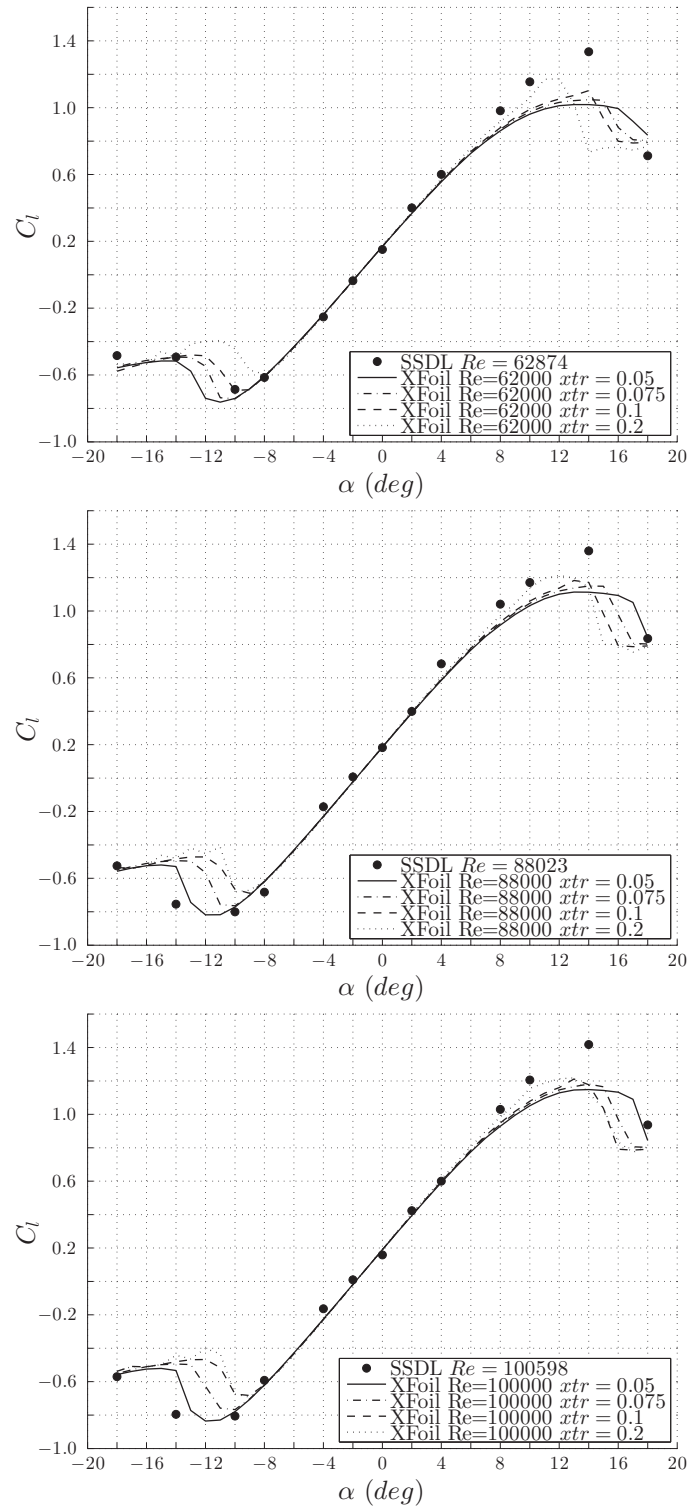


Figure 3.10: Sensitivity analysis of NACA2415 XFoil predictions using $N_{crit} = 9$ for a range of x_{tr}

values, with a $\alpha_{max} \approx 10^\circ$. However, $C_{l_{max}}$ was over predicted for this particular case, reinforcing the idea that this tool must be used carefully and a proper analysis must be done to interpret the outcomes.

The second observation is that these results were mostly insensitive when to the e^n criteria. Only minor differences were noticed when forced transition was implemented on the suction side, therefore every XFOIL prediction was set to $N_{crit} = 9$ and only the trip location was carefully modified.

Overall, XFOIL predicts with acceptable accuracy the trend of the lift curve and the maximum angle of attack, where stall occurs.

3.6.3 SSDL Hydrofoil performance

Finally, the results of the numerically optimized shapes are presented in figure 3.12 for the NACA 2415-SSDL and in figure 3.13 for the corresponding SD8020-SSDL. Looking at the NACA 2415 vs NACA 2415-SSDL, it is important to notice that XFOIL predicts a slight increase in the overall lift coefficient for different α , particularly for the ones accounted for in the optimization routine. The C_d shows little differences with the original foil in figure 3.12b, which translates to an overall higher glide ratio, as expected from the numerical analysis. However, the experimental results only show a moderate variation in the trend for both C_l and C_d , although it effectively turned into a slightly higher glide ratio for the optimized operating points. It can also be noticed that again XFOIL under-predicts the drag, which is expected to be higher given the physical characteristics of the hydrofoil’s roughness and turbulence intensity.

Hydrofoil (%)	Objective Function	Method
SD8020-15tk	91.966	XFOIL
SD8020-SSDL	106.1992	XFOIL
NACA2415	111.9082	XFOIL
NACA2415-SSDL	112.1517	XFOIL
SD8020-15tk	41.946	Exp
SD8020-SSDL	49.150	Exp
NACA2415	39.177	Exp
NACA2415-SSDL	46.250	Exp

Table 3.1: Objective function evaluation between selected hydrofoils

Similar findings were obtained for the SD8020-SSDL. In figure 3.13a the SD8020-SSDL generates a higher lift coefficient over the entire range, in agreement with

XFOIL predictions. Again there is a similar lift curve slope, but shifted upwards. Figure 3.13b, however, shows a substantial increase in drag for the SD8020-SSDL experimental results. The XFOIL prediction also exhibits this drag increase, but underestimates its magnitude. The glide ratio is still in favor of the SD8020-SSDL for the operational points taken during the optimization stage. The final results considering the objective function values is presented in table 3.1. Both predictions and experimental results show an increase in the final operational points considered. It must be remarked that there is a difference in the final experimental value of the objective function, since the data points did not considered the case for $\alpha = 6^\circ$. Nevertheless, the final objective function was constructed using the other 4 operational points. The final SSDL foils show a better performance for the selected range.

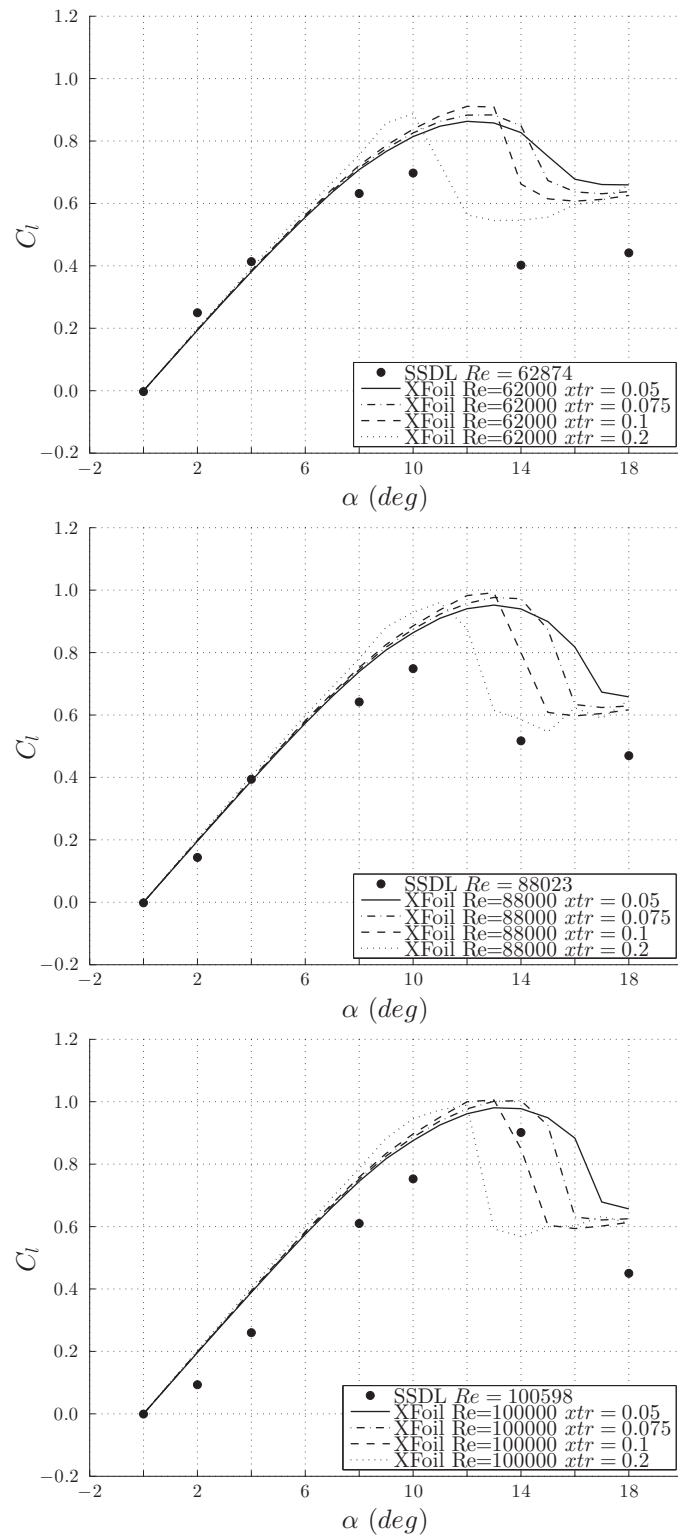
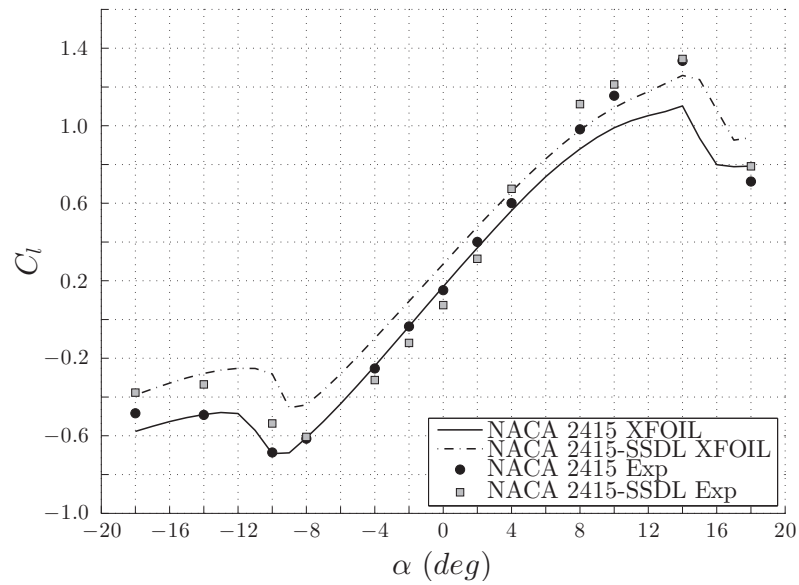
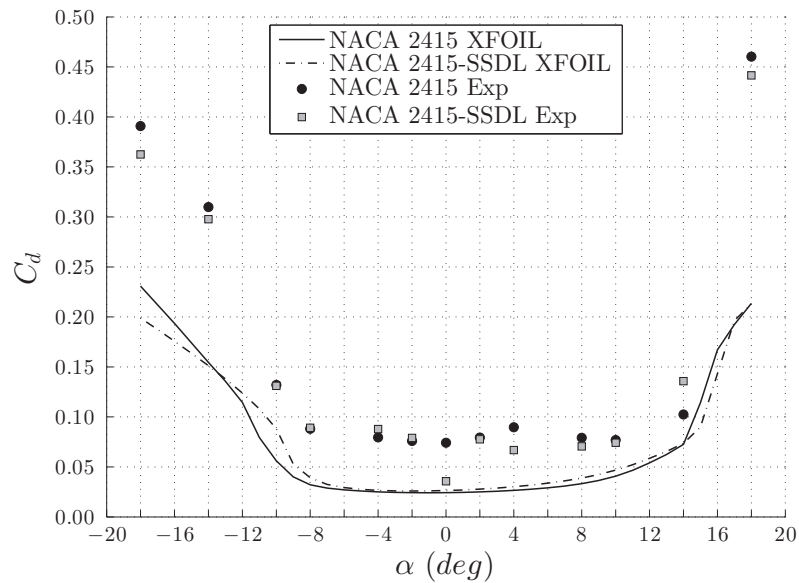


Figure 3.11: Sensitivity analysis of SD8020 15tk XFoil predictions using $N_{crit} = 9$ for a range of x_{tr}

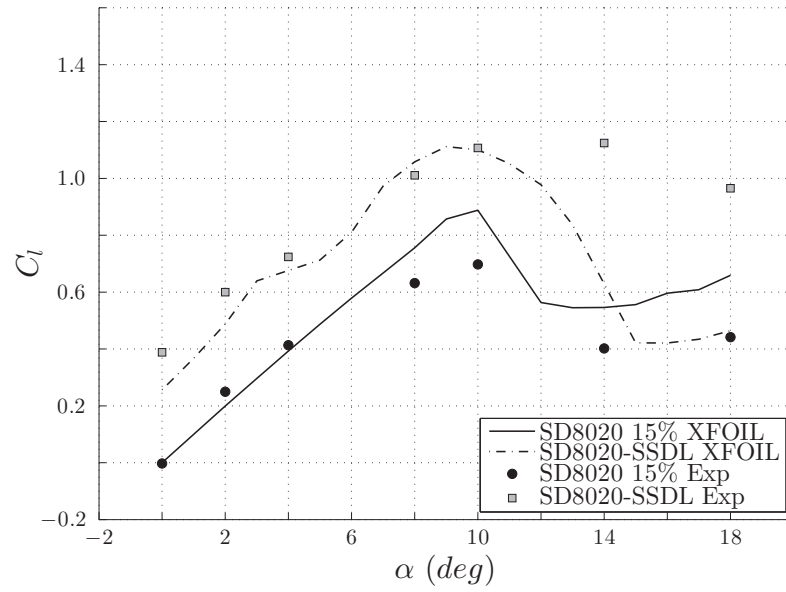


(a)

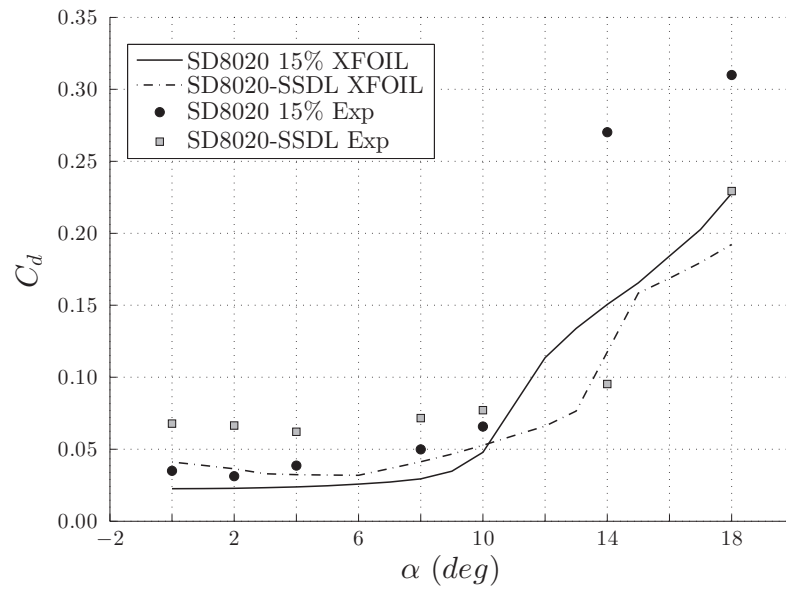


(b)

Figure 3.12: Final results for NACA 2415 and NACA 2415-SSDL for $Re=6 \times 10^4$



(a)



(b)

Figure 3.13: Final results for SD8020 15% and SD8020-SSDL for $Re=6 \times 10^4$

3.7 Conclusions

This study presented a method to experimentally assess the performance of different hydrofoils at low Re using a recirculating water tunnel and PIV to obtain the performance coefficients. This method adequately provides both lift and drag at different angles of attack, considering the particular characteristics of the fabrication method and test facility. The ability to obtain these polar curves also led to further investigations into the performance predictions by employing numerical methods. Using XFOIL and experimental results, it was found that by adding a trip on the suction side of the hydrofoil's surface at a location range between $x_{tr} = 0.1 - 0.2$, the overall predictions were greatly improved. The N_{crit} was also assessed and showed improvement when low N_{crit} values were taken and free transition was set, but the results were not as satisfactory as when forced transition was introduced.

Further experimental studies using PIV are strongly suggested in order to better understand the laminar to turbulent transition that occurs at low Reynolds numbers on the suction side. This way the laminar separation bubbles can be better identified in order to increase the accuracy of predictions when using numerical methods.

Finally, it is interesting to mention that using XOPTFOIL could eventually lead to great improvements in certain hydrofoil characteristics. The SSDL hydrofoils exhibited slightly better performance when comparing the results using the objective function, in this case the glide ratio. There will always be a trade-off when implementing numerical optimization on hydrofoils but it can be a useful tool if a certain performance is needed for a specific flow condition. The objective function can also be modified accordingly and the final results can be compared against experiments by following the same method described in this work. It would also be possible to employ Eulerian CFD methods for optimization of foils were performance well into stall more of a concern, however the experimental determination of stalled drag coefficients would also have to be revisited.

Chapter 4

An experimental study of small scale horizontal axis turbine rotor performance and tip vortex behavior

Authors: Italo Franchini¹, Curran Crawford¹

¹ Dept. of Mechanical Engineering, University of Victoria, BC

To be submitted

The author of this thesis completed this entire work using Crawford's optimization routines [\[23\]](#)

4.1 Abstract

Horizontal axis wind and tidal turbines have similar wake behavior that can economically be studied at small scales in a flume tank. This study presents blade design, rotor performance and near-and-far wake structure characterization using a recirculating flume tank and a small scale axial rotor rig. Power coefficients for the developed blade set are obtained and corrected for blockage effects. Good agreement with BEM simulations was obtained for a range of inflow speeds and tip speed ratios, once the low Reynolds number on-blade performance is properly accounted for relative to full-scale rotor section flow conditions. Regarding the wake structure, tip vortex locations

(shed from the blade tips) were captured using Particle Image Velocimetry (PIV) in the near wake region, showing evidence of wake expansion. The velocity and vorticity fields are also provided to contribute to the development and validation of CFD and potential flow codes.

4.2 Introduction

Horizontal axis wind turbines (HAWTs) are being deployed commercially around the world, notwithstanding the continued challenges in understanding and predicting their detailed hydrodynamic behavior. Horizontal axis tidal turbines (HATTs), as well as 'hydrokinetic' turbines deployed in rivers and channels, are rapidly growing as another viable alternative for zero-carbon energy production. Both tidal and river currents are of great interest due to the large source of energy and predictability that they offer. Thanks to the improvements in turbine technology and design over the past decades, this renewable resource is starting to become competitive, with several projects currently being implemented around the globe. There has been an increasing volume of research in this area, which is critical to understand and predict the hydrodynamic characteristics governing this technology. There are clear similarities to wind turbines, however, there are specific considerations that only apply to tidal rotors that need to be thoroughly investigated.

The goal of this paper is to present experimental results of a small scale three-bladed HATT, developed at the Sustainable Systems Design Lab (SSDL) at the University of Victoria [17]. The study presented here explains the procedure adopted in order to obtain an improved blade design for rotor testing. Dedicated rotor design at small scales is critically important given the low on-blade Re [65]. The power performance over a range of tip speed ratios is experimentally found and using Bahaj wall blockage correlation curves [12] the rotor performance is corrected to unbounded conditions.

The present work also investigates the near-and-far wake regions using Particle Image Velocimetry (PIV) as the quantitative flow visualization technique. It is of particular interest to capture the vortical near-wake flow structures that shed from the blade tips following a helical path downstream. A number of previous experimental campaigns have also sought to evaluate and capture tip vortices propagating downstream of a wind turbine; McTavish [65] provides a good overview of the range of rotor studies in the literature. Haans [66] measured tip vortex locations, vortex

pitch, wake skew angle and wake expansion using smoke as a quantitative flow visualization method. McTavish [24], [67] employed dye visualization to study wake expansion and vortex pairing for different blockage ratios. Other studies involving PIV were of particular interest since the same technique will be employed in this work. Grant and Parkin [25] studied the trailing vortex in yaw using PIV, Massouh and Dobrev [26] obtained phase-locked PIV to capture the near wake for different azimuth planes and Sherry *et. al* [27] presented a complete study showing tip and root vortices using both qualitative and quantitative flow visualization methods. All of these studies considered wind turbines for near wake characterization. The present study is focused on application to tidal turbines, but many of the findings can also be applied to wind turbines if the wake structure is assumed (rotor diameter based) Reynolds independent, which is typically found to be the case [68], and chord Re are taken into account in any analysis or up-scaling to full size.

The use of PIV on small-scale rotors (≈ 0.25 m diameter) presented in this report is the distinguishing feature of the current work. If viable from a technical perspective, the use of small rotors can reduce fabrication costs and enable the study of many rotor designs easily, while enabling the use of smaller, lower cost facilities. The remainder of the paper is organized as follows. 4.3 describes the rotor rig, followed in 4.4 by the blade design. The experimental method is documented in 4.5, followed by a presentation and discussion of results in 4.6.

4.3 Axial Rotor Rig

An experimental apparatus, originally design by Lártiga [17], was developed at the SSDL to reproduce in a realistic manner the flow phenomenon behind a HATT. This test rig allows researchers to study the wake structure behind the rotor plane, in particular in the near-wake region, where the gathered data can be used to validate CFD and potential flow simulation codes also being developed in the SSDL.

A three-bladed rotor is attached to a main horizontal shaft that is connected to a vertical support tube. A fairing surrounds the vertical tube to reduce its wake, and can be yawed separately from the rotor to align with the flow in yawed experiments. These parts comprise the entire submerged structure, leaving the drive system and instrumentation (also referred as the top structure) outside the water tunnel. A AKM23D servomotor is attached to a Novatech F326-Z torque cell, allowing the system to capture the reaction torque ranging from $\pm 1 \vec{N}m$. A timing belt going

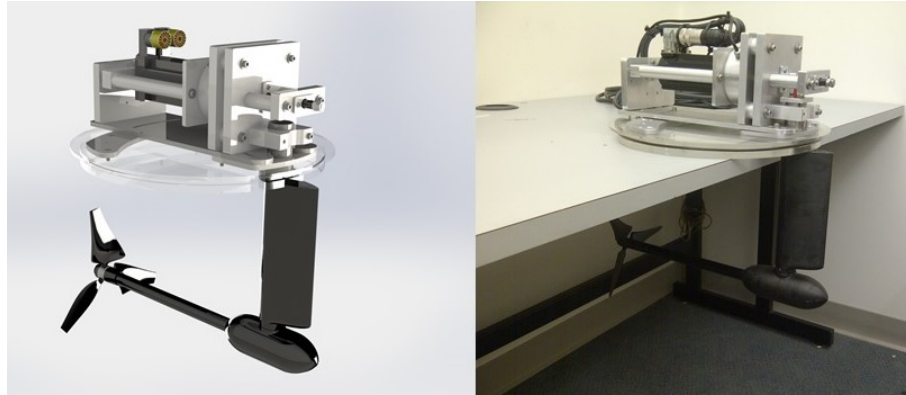


Figure 4.1: Rotor rig final design

down through the vertical tube carries the motion from the motor to the horizontal shaft. The rotor is fully controllable to any desired rotational speed, thus allowing a precise control of the Tip Speed Ratio (TSR, λ), defined in section 4.5.3. Important modifications to the original design by Lartiga [17] were addressed by the current authors to resolve some operational and assembly issues with the drive system, hub assembly and instrumentation. The final testing rig is shown in figure 4.1. The hub diameter is 25.4 mm and can accommodate a range of rotor diameters.

The instrumentation system uses the NI CompactRio package as a control and DAQ system. The NI 9237 simultaneous bridge module captures the torque readings and the NI 9514 is a single-axis servo drive interface module with incremental encoder feedback that allows full control of the system. A specific user-defined software was developed in Labview, providing a graphical user interface for easy access and control.

4.4 Blade Design

Previous experiments involving different blade sets have been tested at the SSDL by Lártiga [17], without successful results. Relatively poor performance and bending of the blades were the main issues to tackle at the start of the present work. The blades are manufactured using a Fused Deposition Modeling (FDM) machine that builds-up the model geometry in layers using polycarbonate. The structural problems arose mainly due to the small scales involved and the fabrication method employed.

The blade length considered in this work is 100 mm, following previous analysis and experimental work presented by Lártiga [17]. After evaluating different possible solutions, the chosen approach was to set a minimum chord length during the design

process, since most of the bending occurs close to the tip. Another very important factor to be considered for an optimal blade design is the hydrofoil selection. The University of Illinois at Urbana-Champaign (UIUC) Low-Speed Airfoil Test program [48] database was consulted for airfoils capable of performing well at low Re. Most of the ideal candidate foils have a maximum thickness $\leq 10\%$, which could potentially present structural problems. Therefore, it was decided to impose a constraint on the maximum thickness as well, bearing in mind the existing trade-off between performance and structural behavior, since thicker foils usually exhibit higher drag forces. That being said, a minimum of 15 % thickness was imposed in order to ensure blade rigidity. Both considerations, i.e. chord length and foil thickness, seemed the most viable alternatives in terms of building cost, complexity and ensuring acceptable rotor performance.

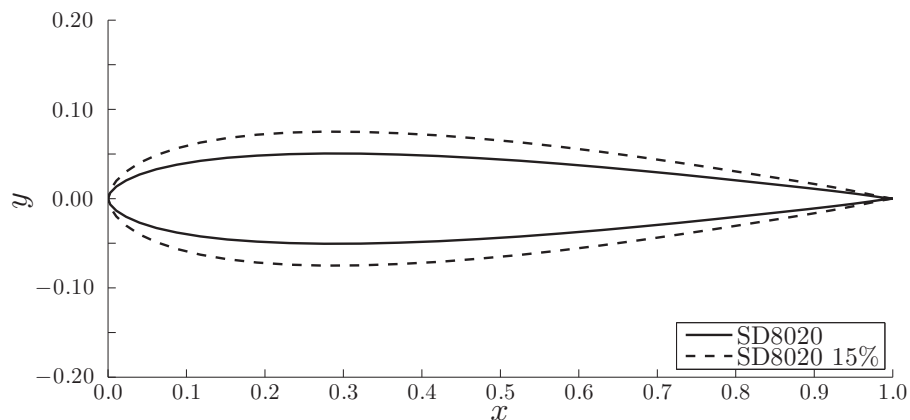


Figure 4.2: SD8020 hydrofoil

The selected hydrofoil was the SD8020 [48] and is shown in figure 4.2. This hydrofoil exhibits good low Re performance and also shows very low Re dependency over the range of interest, i.e. between $6 \times 10^4 - 1 \times 10^5$. Since a 15% thickness is imposed and the hydrofoil's hydrodynamic coefficients can be found only for a 10% thickness, it is necessary to obtain these polar curves experimentally. For this purpose, a 2D hydrofoil test was carried out using the SD8020 15%. Using the FDM machine a hydrofoil with 70 mm chord was printed and tested in the UVic's water tunnel. A more detailed explanation of the experimental procedure to obtain C_L and C_D from these tests is provided by Franchini *et. al* [69].

Once the hydrofoil selection was completed, including the results of lift and drag coefficients, an optimization routine developed by Crawford [23] was implemented

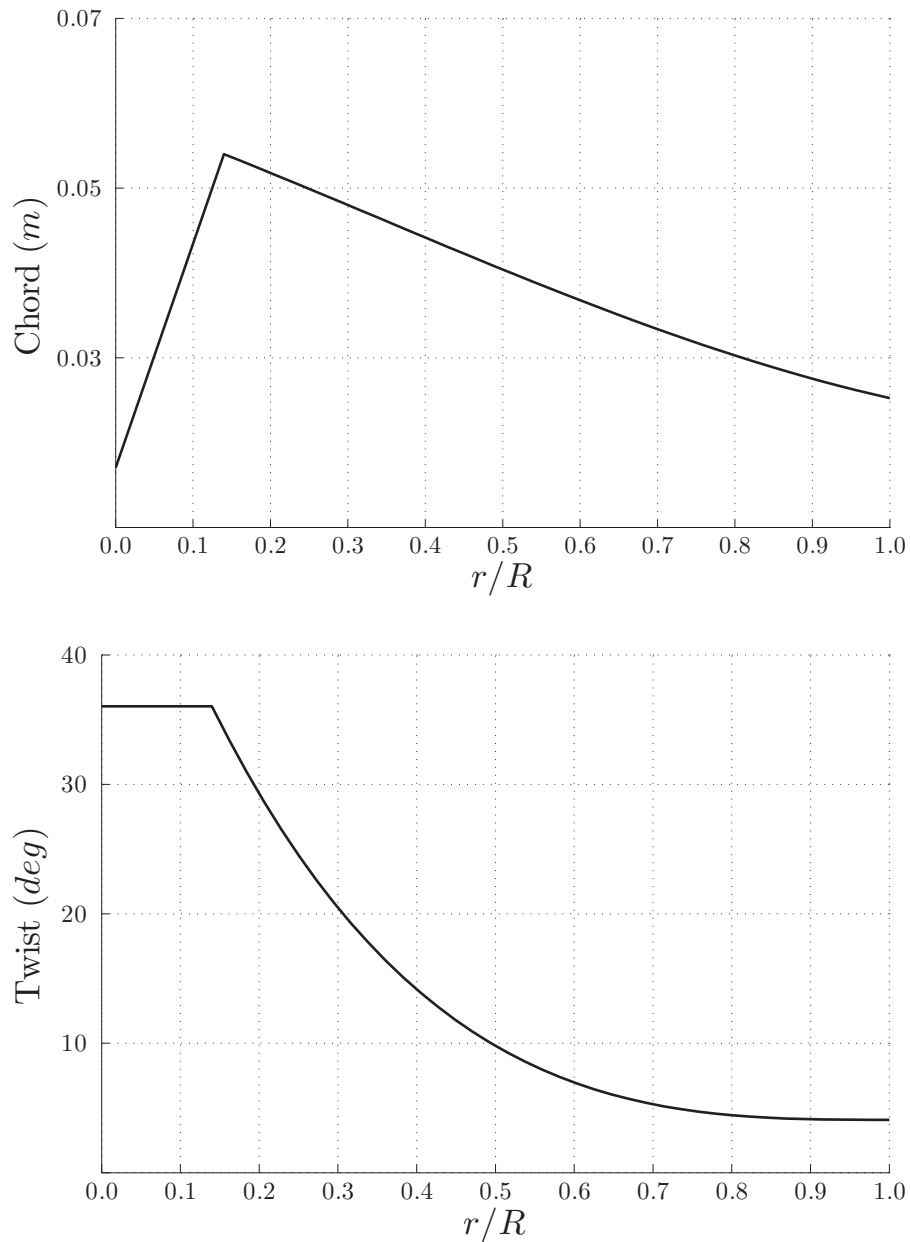


Figure 4.3: BEM results showing the blade parameter distribution to be used for the final design

based on Blade Element Momentum (BEM) theory (Glauert [10]). The optimization algorithm to find an optimal chord and twist distribution was limited to inflow speeds between $1.2 - 1.4 \text{ m/s}$ and for a total blade length of 100 mm . The script also accounted for a minimum chord length of 10 mm . This constraint forces a trimmed tip shape, which is slightly detrimental to power performance but also sheds a more

defined vortical structure that will aid the visualization and identification of these tip vortex cores.

Figure 4.3 shows the BEM simulation results, where both chord and twist distribution parameters are plotted over the entire blade span. From the BEM simulation the Re operational range is also illustrated in figure 4.4. For this particular case a steady state simulation was considered using three different free-stream velocities and for an operational point of $\lambda = 3.5$, which is the point where simulations predicted a maximum C_P .

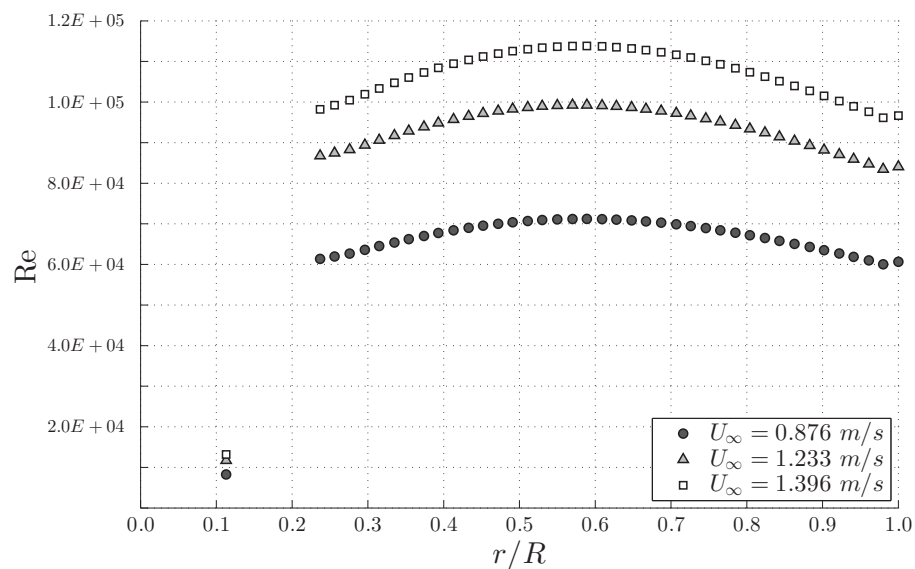


Figure 4.4: Blade set Re operational range

Having the optimized blade parameters, the final design was modeled using the commercial CAD tool Solidworks and fabricated using the FDM machine, as represented in figure 4.5. The FDM machine builds parts layer-by-layer from the bottom up by heating and extruding thermoplastic filament. Building material and tip sizes are important parameters that will define the quality and roughness of the final part. Previous experimental campaigns [17] used the smallest tip available (T10) and the ABS-M30 material, resulting in smooth blades that turned out to have a low performance. Therefore the final blades were printed using a T12 tip combined with a polycarbonate material, resulting in a rough surface finish and better mechanical performance.

Additionally, a Finite Element Analysis using a static structural approach was performed using the commercial software ANSYS Mechanical REF and shown in

figure 4.7, where the expected maximum deflection under the highest possible load conditions should not exceed 2.5 *mm*.

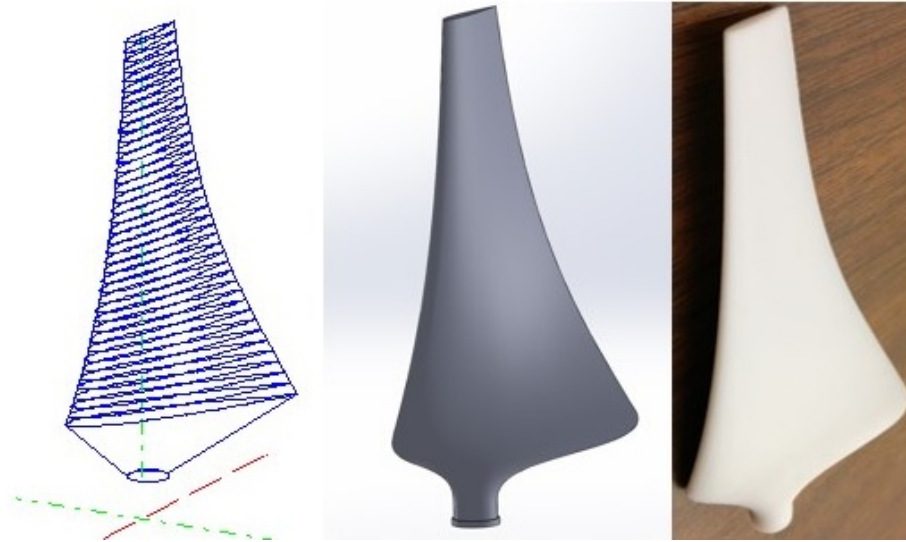


Figure 4.5: Final blade design

The experiment setup, as described in section 4.5.1, utilized an acrylic lid located on top of the section test that eliminated any free surface effects. However, an existing wall blockage is present and needs to be taken into account in order to obtain more accurate comparisons to free boundary condition simulations. The blockage ratio (BR), defined as the ratio of rotor swept area to the cross-sectional flume area, is found to be $BR = 0.197$ for this particular blade set. Since the blockage ratio is not negligible, a correction method must be applied to the BEM results.

4.5 Experimental Method

The model turbine was placed in the water tunnel, as shown in figure 4.6. The pitch angle β , defined as the angle at which the blades rotate around their own axis relative to the overall plane of the rotor, is set to the design value $\beta = 4.1^\circ$ at the tip. The angle of yaw is set to $\gamma = 0^\circ$ throughout the entire study.

4.5.1 Water tunnel

The test campaigns were conducted in the University of Victoria Fluids Research Lab flume tank. The test section of the water tunnel has a cross section of 0.45×0.45

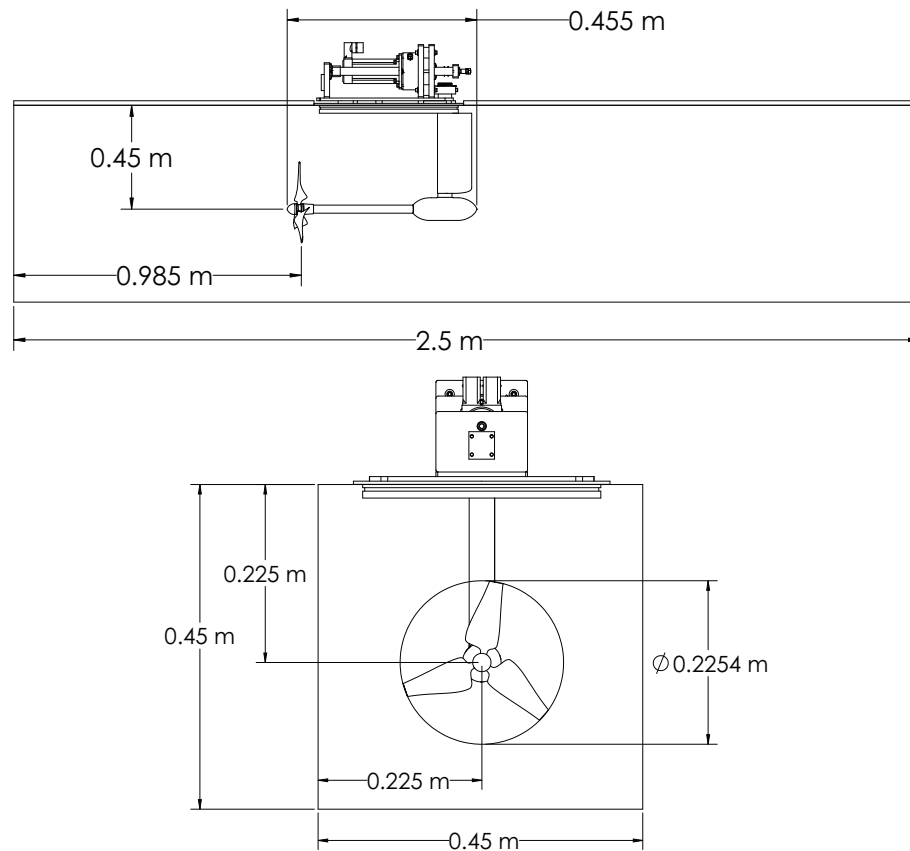


Figure 4.6: Rotor rig sketch inside flume tank showing principal dimensions

m and a length of approximately $2.5 m$. The top of the test section can be opened for tests involving a free surface (air-water interaction), or can be closed off using two acrylic lids. With the lids installed, the effects of free surface deformation are no longer present and throughout this experimental campaign it was used to test the rotor rig. The wall material is clear acrylic allowing optical access through the sides and bottom. The flow is driven by a single-stage axial flow propeller pump delivering a maximum flow rate of $405 L/s$. The pump shaft RPM is controlled using a Toshiba VT130H7U6270 frequency controller that allows inflow speeds up to $1.6 m/s$. The controller only allows setting a specific pump frequency, therefore additional instrumentation is required to obtain the flow velocity in the working section of the tunnel.

The inflow to the test section consists of a perforated plate, honeycomb section, 5 high-porosity screens and a 6:1 contraction. Downstream of the test section the flow is diverted by turning vanes in the return plenum into the return flow pipe located underneath the test section. The design turbulence level is approximately 1.0% .

4.5.2 Particle Image Velocimetry

Particle Image Velocimetry (PIV) is a non-intrusive flow visualization technique that is capable of obtaining quantitative flow visualizations of the global velocity field over a two-dimensional region, allowing researchers to study flow structures with great detail due to the large number of data points contained in one image [70]. In addition, the high speed capability for image acquisition allows time resolved PIV measurements that can capture several flow properties, such as vorticity, turbulence, rate of strain or viscous dissipation, among others.

The PIV equipment at the University of Victoria Fluids Research Lab consists of a Quantronix Darwin-Duo Nd:YLF high speed laser operating at a wavelength of 527 nm , a Photron Fastcam APX-RS high-speed camera that provides full 1024×1024 pixels resolution images at frame rates up to 3 kHz and a PC hardware/software system run by LaVision Davis 7.2 for data processing. The laser is placed on top of an optical table on one of the sides of the flume and mounted on rails that can accurately position the system for the desired height and distance parallel to the flume. The laser sheet was set horizontally and right at the center of the test section, coincident to the rotor rig's hub.

The water is seeded with silver-coated hollow glass spheres that effectively reflect the laser beam and allows the capture of the entire flow. The camera is mounted on a carriage assembly beneath the test section, allowing images to be taken along the entire flume's length. The system is configured for double-frame images separated by a small time delay δt , which is experimentally tuned based on the particle shift displacement between frames.

4.5.3 Blade Performance

The new blade design needed to meet the maximum deflection criteria before proceeding with the experimental campaign. In order to test the rotor blades, the pump controller was set to 40 Hz, as this will provide the highest flow rate condition, giving a free-stream velocity of $U_\infty = 1.396\text{ m/s}$.

It was also necessary to introduce a non-dimensional parameter to analyze the turbine efficiency. The Tip Speed Ratio (TSR) is defined as the ratio between the tangential speed of the tip and the free-stream velocity of the flow, given by the

following expression:

$$\lambda = \frac{\omega R}{U_\infty} \quad (4.1)$$

where ω is the rotor rotational speed controlled by the user, R is the rotor radius taken from the center of the hub to the tip of the blade, which in this case is $R = 112.7 \text{ mm}$ and U_∞ corresponds to the flow velocity at the inlet of the test section. The rotor was programmed to run at TSRs ranging from $\lambda = 1 \rightarrow 6$, which is the same range that the rotor will be tested for blade performance. To capture the blade deflection, PIV images will be taken when the blade goes through $\varphi = 0^\circ$. The deflection will be analysed manually based on the resulting images.

After checking the structural behavior of the blades, the characteristic power performance curve needs to be obtained experimentally. The rotor rig setup remains unaltered and the power coefficient C_P was computed using equation 4.2 for the entire range of TSR previously mentioned.

$$C_P = \frac{P}{\frac{1}{2}\rho U_\infty^3 A_d} \quad (4.2)$$

Here P corresponds to the total power given by $P = T\omega$, ρ is the water density and A_d is the area swept by the rotor's blades. The experiment was carried out using three different pump frequencies of 25, 35 and 40 Hz. For each frequency the velocity was measured using PIV at the inlet, using a 50 mm focal length lens to capture the two-dimensional flow field of the horizontal plane. In order to obtain an acceptable time averaged flow field, 2500 images were captured using a frame rate of 25 Hz, the smallest rate available for the system. The procedure was repeated 3 times per pump frequency. Finally, the resulting inflow speeds used for this experiment are 0.876 m/s, 1.233 m/s and 1.396 m/s.

In addition, the Blockage ratio (BR), defined as the blade's swept area over the flume's cross-sectional area, is found to be 19.7%. This will be the only blockage considered for the experimental tests. Since the blockage ratio is not negligible, a correction method must be applied to the test results in order to express them to unbounded conditions. For wind turbine applications, Glauert [10] was the first one to propose an analytical expression to correct the testing data to unbounded conditions, using the actuator disk theory approach. Important improvements to Glauert's method were developed by Mikkelsen and Sorensen [11], but their study involved exclusively wind turbines. The first approach for wall interference correction

for tidal applications was presented by Bahaj *et. al* [12], who provided a correlation between the thrust coefficient C_T and the ratio given by U_T/U_F , where U_T is the measured water tunnel speed and U_F corresponds to an equivalent water speed. This method, however, could not be directly applied to this study since thrust data is required to be measured experimentally. To overcome this issue and to obtain a rough correction, the C_T was taken from BEM simulations.

4.5.4 Wake structure

An important part of this work is focused on capturing the near wake region behind the rotor plane, specifically the vorticity shed from the blade tips that results in tip vortices trailed downstream in the rotor wake following a helical pattern. The induced velocities at the rotor are heavily influenced by this near wake region, in turn determining the power output of the rotor. The PIV technique becomes an essential tool that allows the capture of the vorticity in the rotor wake at a given azimuth plane. To minimize camera positioning errors, the camera was mounted on a linear actuator that allowed high-accuracy positioning. The camera was restricted in lateral motion and the images were taken at the tip of the rotor blades. The free-stream velocity was set at $U_\infty = 1.233 \text{ m/s}$ and the rotor was operated at the design tip speed ratio $\lambda = 3.5$.

Due to the small size of the rotor blades and the minimum resolution required for processing the images, a maximum window size of $50 \times 50 \text{ mm}$ was carefully chosen. A 130 mm focal length lens was selected to obtain double-frame images using a $\delta t = 160 \mu \text{ s}$. In order to accurately capture the tip vortices trailing from the blades, it was crucial to synchronize the rotor's azimuth angle with the PIV triggering system, since every 1 ms delay meant 2° of cumulative error of the azimuthal plane. Five camera locations were used to capture these trailing vortices up to 2 rotor radius's distance downstream ($2R$). Due to the camera's high frequency work range it is possible to obtain images for several azimuth angles within 1 rotor revolution. It was arbitrarily chosen to capture the wake at every 20° , i.e. $\varphi = 0^\circ, 20^\circ, 40^\circ \dots 340^\circ$. For each camera location and azimuth angle 300 images were taken to provide a phase-locked averaged wake velocity field, thus capturing snapshots of the vortical structures within the near wake region at a given azimuth plane.

The setup to capture the far wake region follows a similar procedure as described above, but the camera lens was replaced with a 50 mm focal length lens that allows

a wider field of view to be captured. For this experiment only one camera position in the y -axis was selected, i.e. at $y = 0$ for the entire test section, which was captured using 9 camera locations, including upstream and downstream of the rotor plane. Once again, 300 images at each position were taken to ensure statistical convergence of the phase-locked average velocity field. The camera field-of-view allowed to capture almost the exact size of the rotor's diameter, neglecting the results between the blade tip and the solid wall.

4.6 Results and Discussion

The results and analysis of final blade design, rotor performance and wake structure are presented in this section. The first results to be analysed are those involving blade deflection and performance. If the design does not meet the structural requirements, then results will not be comparable to previous studies.

4.6.1 Rotor Performance

The structural response caused by the load on the rotor blades is shown in figure 4.7. The highest load on the blades was found to be when the turbine was operating at $\lambda = 3.5$, as expected. The final result shows a $\delta_{max} = 1.2$ mm, reaffirming that the blade design and fabrication method satisfactorily avoids unwanted deflections on the rotor plane, keeping $\delta_{max} < 1\%$.

The following experiment was focused on obtaining rotor performance at three different inflow speeds. The results are presented in figure 4.8 and show excellent performance for the free-stream velocities considered in the study. The maximum C_P occurs at $\lambda = 3.5$ for all three cases, in good agreement with the BEM simulation results.

The total uncertainty analysis, including systematic and random components, was calculated following Wheeler and Ganji's [32] step-by-step uncertainty analysis procedure. The random uncertainty in the measurements was calculated using a t -student distribution with $\nu = 5$ degrees of freedom for each different operational point in the domain. It was found that systematic errors were an order of magnitude lower than the random component, thus their inclusion had a negligible impact on the total error.

As the inlet velocity U_∞ increases the uncertainty is reduced, mainly due to the

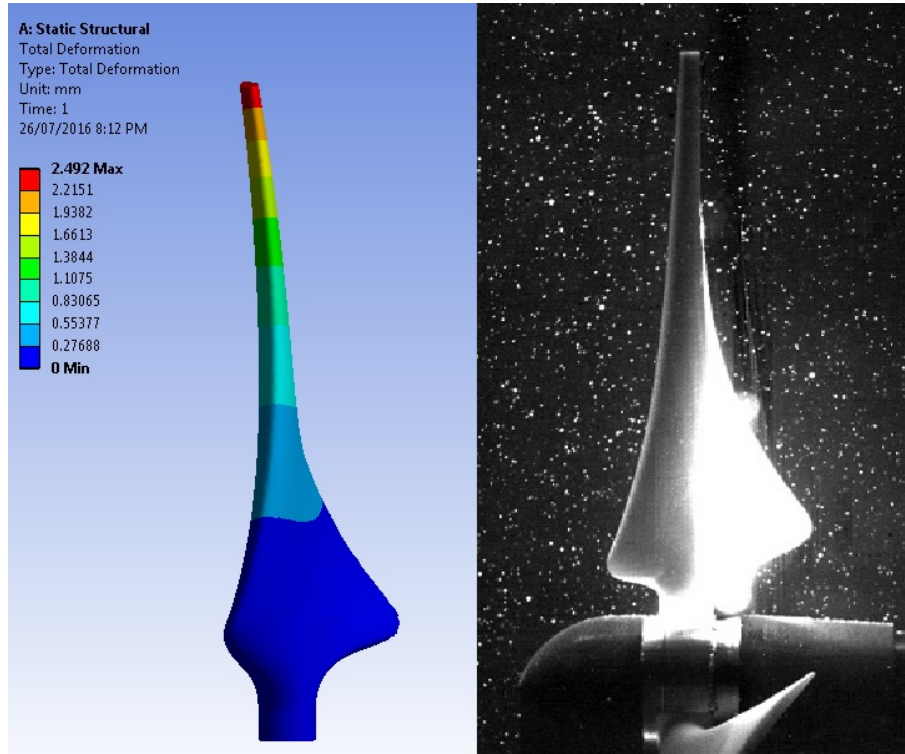


Figure 4.7: Blade deflection FEM analysis (left) and Experimental result (right). The maximum experimental deflection was found to be $\delta_{max} = 1.2 \text{ mm}$

fact that C_P is proportional to U_∞^3 , thus higher inflow speeds reduce the overall uncertainty of the measurements.

These results show a sudden drop in the C_P below the optimal λ . The physical origin of this behavior is that at low TSR the rotor blades experience higher angles of attack, causing the flow to detach from the blades, i.e. stalling. Another possibility is that HATTs become inherently unstable when they operate at TSR lower than the peak torque point, because it becomes difficult to maintain the desired rotor speed. However, the rig used for these experiments uses a high-accuracy servo motor that has capable speed control, and the PIV images did not indicate erratic rotor positions associated with speed errors.

It was decided to use $U_\infty = 1.233 \text{ m/s}$ for the next part of the experiments, since using the smallest free-stream velocity, i.e. $U_\infty = 0.879 \text{ m/s}$, resulted in a noticeable Re dependency and increasing uncertainty compared to the higher velocity cases. The higher speed was not considered this time only to avoid additional stresses on the rotor blades. Figure 4.9 presents the rotor performance for the selected inflow speed applying the correction method presented by Bahaj [12]. Since the rotor rig

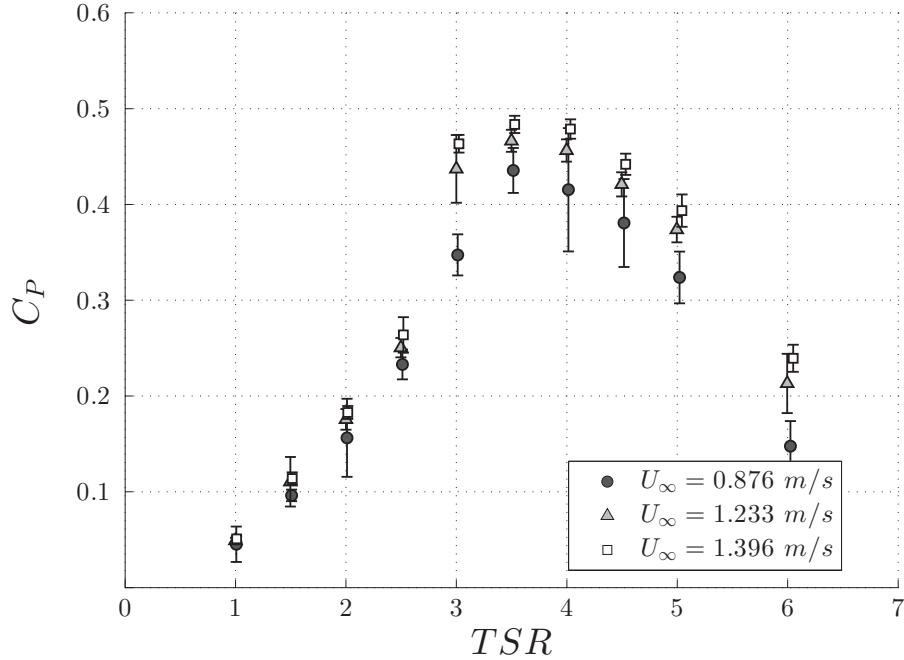


Figure 4.8: Rotor performance over a range of inflow speeds for BR=19.7%

is not capable of capturing C_T , BEM results were used to obtain a rough correction. The ideal situation for further experiments will focus on experimentally obtaining the axial induction factor and apply the correction approach developed by Lártiga [13], who used the axial induction factor instead of the C_T for power corrections.

Figure 4.9 also shows the BEM prediction. The code fails at predicting the power in the stall region, i.e. below $\lambda = 3$, but shows a reasonable trend for greater TSR. It also accurately predicts the TSR where the maximum power coefficient occurs, but underpredicts its magnitude. This can be explained by looking at previous experimental campaigns [17], where the experiments showed evidence of increasing C_P when rough surface blades were considered, since for this low Re the blade roughness delays laminar separation effects (because it becomes turbulent earlier on the suction side of the hydrofoil), enhancing its performance.

4.6.2 Near-and-Far Wake Regions

The near wake structure is captured at the maximum power performance operational point, i.e. when $\lambda = 3.5$, considering an inlet velocity of $U_\infty = 1.233$ m/s. The 300 images available for each camera location and azimuth angle were post-processed with Davis 7.2 [71] to obtain the velocity vector fields. For each set, a phase-locked average

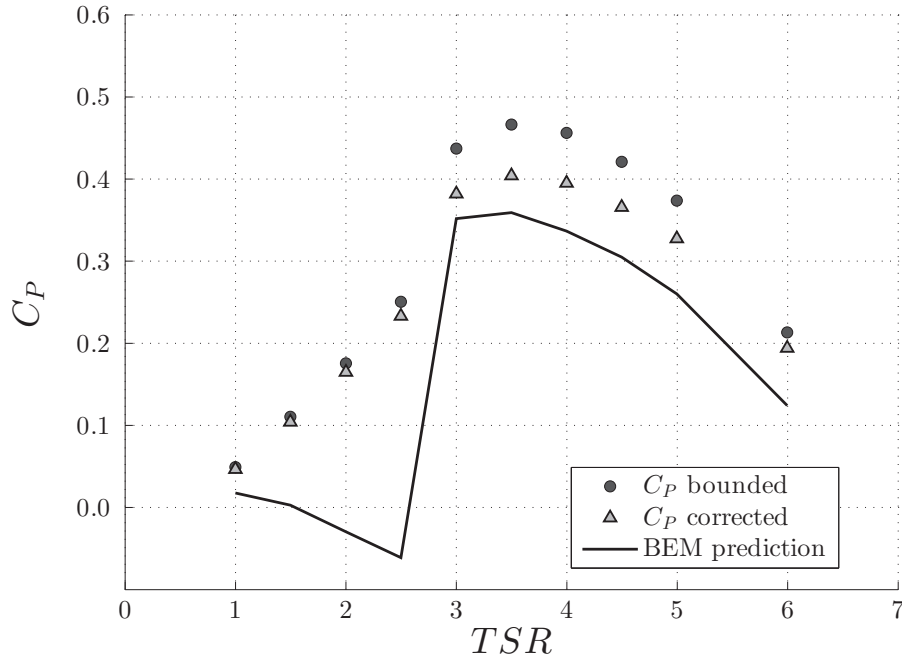


Figure 4.9: Rotor performance for $U_\infty = 1.233 \text{ m/s}$, showing the bounded, unbounded (corrected) and BEM predictions.

velocity field was obtained and posteriorly the average vorticity field was computed, using equation 4.3:

$$\omega_{\vec{z}} = \vec{\nabla} \times \vec{v} = \left(\frac{\partial v}{\partial x} - \frac{\partial u}{\partial y} \right) \hat{k} \quad (4.3)$$

The tip vortex location is assumed to be at the tip vortex core centre, following a similar procedure to the work done by Haans *et. al* [66]. This method delivers a reliable position of the tip vortex locations that represent the edge of the wake downstream the rotor's plane. However, a problem arises when using phase-locked averages to study the vorticity, since wandering [72] is introduced.

To overcome this problem and to reduce vortex wander, individual images from the instantaneous vector fields were selected in which the vortex fell at the same location as the average field, following the same methodology employed by Grant and Parkin [25]. This was done for every camera location at every azimuth angle. Finally the fields from these selected images were stitched together to reproduce the entire vector field. As an example, the axial velocity field normalized by the free-stream velocity showing the intersection between the helical vortex tube and the 0° azimuth plane is shown in figure 4.10. Both axial and lateral coordinates have been normalized by the rotor radius; i.e. when $\varphi = 0^\circ$ the tip is located at $(0, 1)$. All the results, as

mentioned in section 4.5.4, are presented considering 1 operational condition with $U_\infty = 1.233 \text{ m/s}$ and $\lambda = 3.5$.

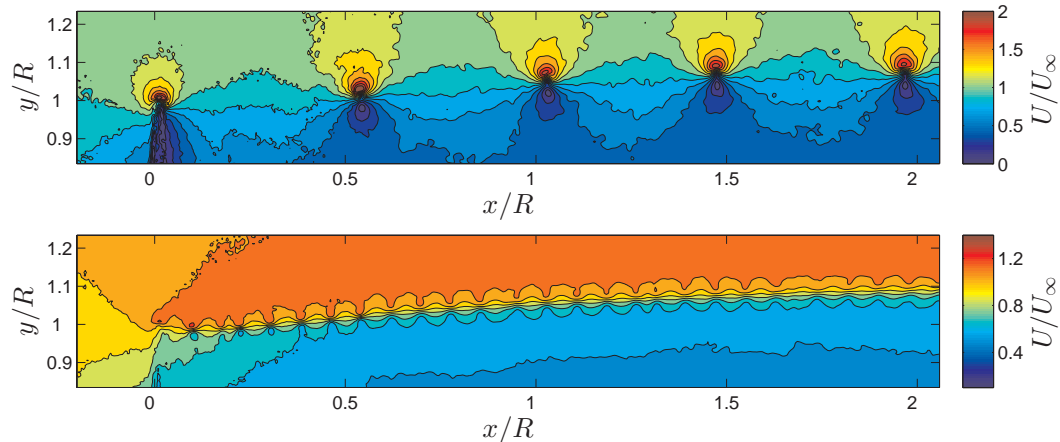


Figure 4.10: Contours of axial velocity at the blade tip when $\varphi = 0^\circ$ (top) and a phase-locked average of the wake considering all the azimuth planes (bottom)

Figure 4.10 shows the progression of the tip vortex downstream, given by the average over the entire range of azimuth planes, showing an increase in axial velocity right outside the near wake and a velocity deficit inside of it. These observations agree with the expected velocities that surround a vortex core. The high rate of rotation produced by the vortex creates a low pressure in its core, accelerating the fluid around it, which causes an increment in the tangential velocity. Immediately outside the wake the effect is observed as an increase in the total axial velocity, whereas inside the wake the flow is reversed contributing to the velocity deficit observed.

Vorticity plots are presented showing the progression of the vortex tubes that intersect the azimuth planes. The vorticity was normalized using the non-dimensional vorticity quantity employed by Sherry *et. al* [27] and given by $\overline{\omega}_z R / U_\infty$, where $\overline{\omega}_z$ is the phase-locked vorticity average, R is the rotor radius and U_∞ corresponds to the free-stream inlet velocity. Figure 4.11 presents the results of three azimuth planes corresponding to the first blade passing through the plane. The same analysis is presented in figure 4.12 that captures the same sequence but considering the second blade, since the blades are located 120° apart from each other. Similarly, figure 4.13 shows the results for the third blade.

The vorticity fields show initial evidence of a slight wake expansion given by the outward radial movement of the tip vortices. Also, a slight decay can be noticed of the tip vortex strength as it moves downstream. Figure 4.14 shows the location of every

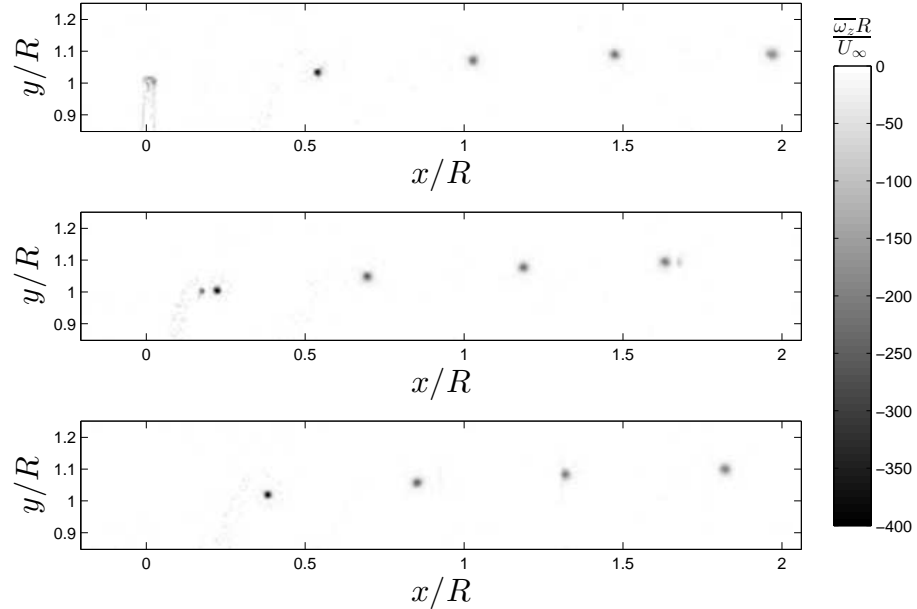


Figure 4.11: Vortical structures shed from the blade tip in the near wake at maximum power performance, showing contours of non-dimensional tangential vorticity for azimuth planes of $\varphi = 0^\circ$ (top), $\varphi = 40^\circ$ (middle) and $\varphi = 80^\circ$ (bottom)

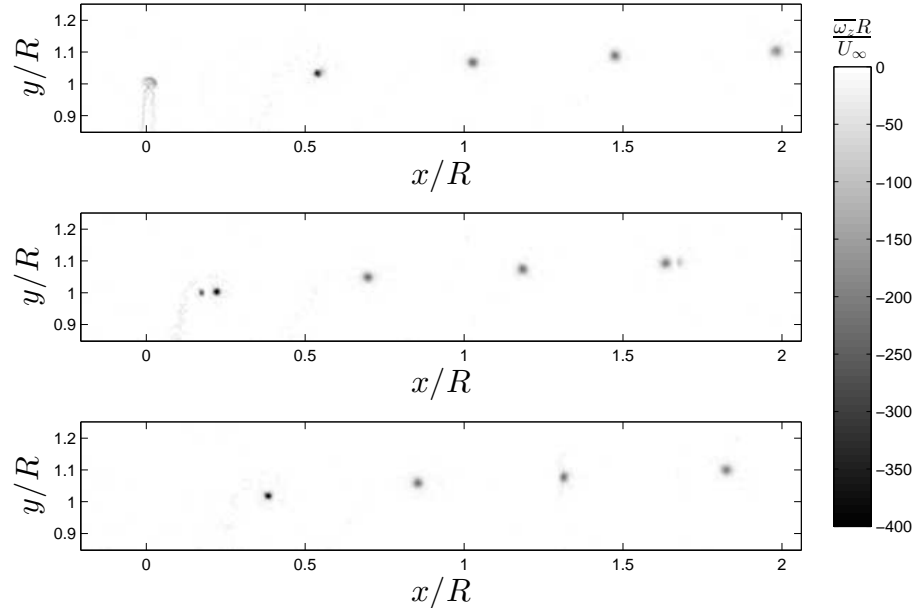


Figure 4.12: Vortical structures shed from the blade tip in the near wake, showing contours of non-dimensional tangential vorticity for azimuth planes of $\varphi = 120^\circ$ (top), $\varphi = 160^\circ$ (middle) and $\varphi = 200^\circ$ (bottom)

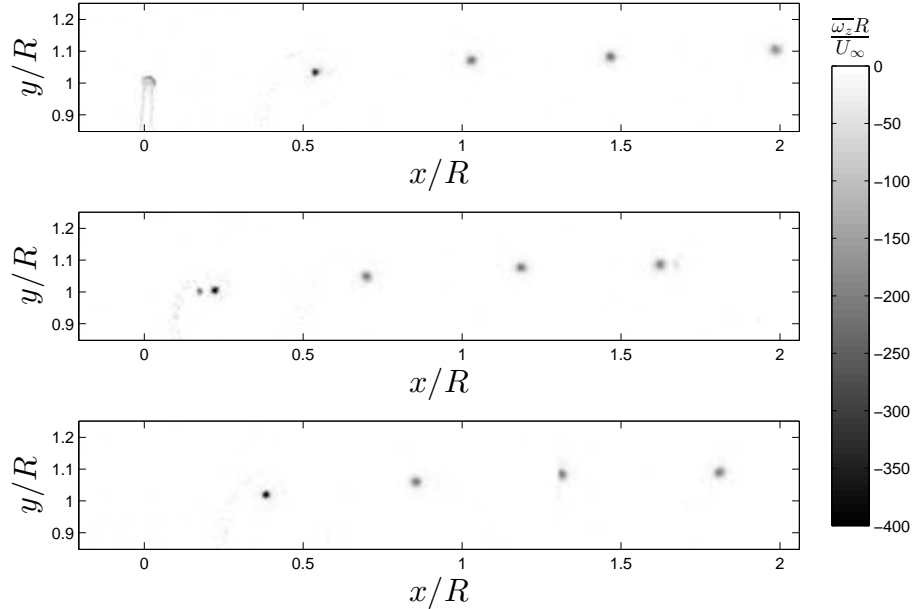


Figure 4.13: Vortical structures shed from the blade tip in the near wake, showing contours of non-dimensional tangential vorticity for azimuth planes of $\varphi = 240^\circ$ (top), $\varphi = 280^\circ$ (middle) and $\varphi = 320^\circ$ (bottom)

tip vortex found for every azimuth plane. It confirms the expected wake expansion, with a maximum radial distance of $1.1R$ located at a distance of $2R$ downstream. No evidence of vortex pairing was found in this work for the considered downstream distance evaluated, which is also consistent with McTavish [67] results for a high blockage case, where results showed evidence of reduced and delayed vortex pairing with increasing blockage.

It is also interesting to point out that after $x/R = 1.5$ a slight difference can be noticed regarding the radial distance of the vortex locations. The results show that the tip vortex captured at $\varphi = 60^\circ - 80^\circ - 100^\circ - 120^\circ - 140^\circ$ and $\varphi = 180^\circ - 200^\circ - 220^\circ - 240^\circ - 260^\circ$, which are the same azimuth planes corresponding to blade 1 and blade 2, exhibit a slightly higher trend when compared with the same azimuth planes for the third blade. This might indicate a decrease of the wake expansion rate. More images downstream are necessary to investigate this behavior. Since this difference is very small it could also be attributed to the experimental error when computing the vortex core location.

The results from figure 4.14 show how the wake expands considering a blockage of 19.7%. McTavish [24] found that as blockage increases, the downstream wake expansion narrows down artificially due to the proximity between the blade tips and

the solid wall. Further experiments will assess the blockage ratio and wake expansion for tidal turbines and it would be interesting to develop a correction method to predict wake expansion for the unbounded case.

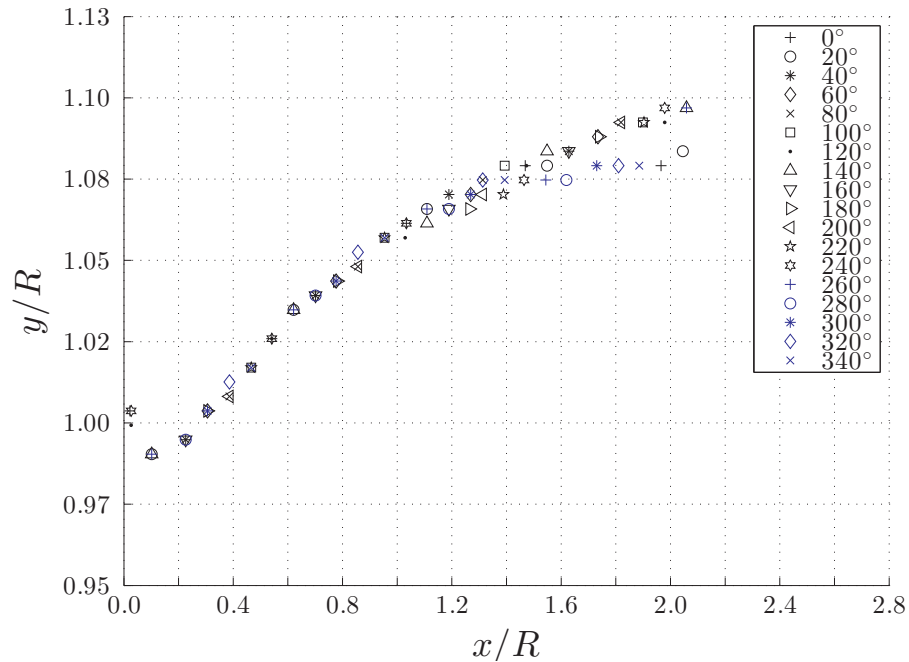


Figure 4.14: Tip vortex behind near wake region

Finally, the far-wake region result is presented in figure 4.15, where the axial velocity field has been normalized by the free-stream velocity calculated at the inlet. The inlet flow speed shows a uniform distribution and as the fluid approaches to the rotor plane it can be noticed a slight decrease in velocity. The rotor plane and horizontal sting have been masked out in order to avoid bad vector calculations. Looking downstream in the wake region, the velocity decays at most to about half of the free-stream inflow speed, persisting further than the test section allows to capture. By $x/R = 12$ the wake still exhibits a velocity deficit of approximately 20%. A longer test section is necessary in order to find the total distance where the velocity recovers over 90% of its initial magnitude, but it is out of the scope of this project. Further studies will also consider capturing the blade tip region until the solid wall, using more camera locations.

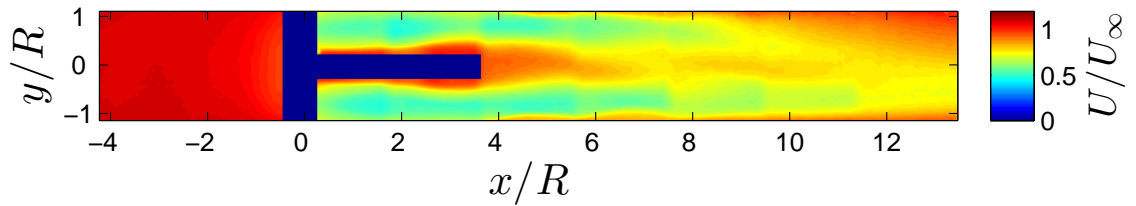


Figure 4.15: Normalized velocity field showing the wake development for the entire test section. The rotor plane and sting have been masked out.

4.7 Conclusions

Blade design, rotor performance and wake structure of a small scale horizontal axis tidal turbine were investigated at the Sustainable Systems Design Lab, using the fluids research facility located at the University of Victoria. The rotor was tested under three different free-stream velocities with a wall blockage of 19.7%, showing good agreement with BEM predictions. The optimal operational point for each case was found to be at $\lambda = 3.5$. At lower TSR the rotor blades experienced stall that produces a detached wake structure, which considerably impacts on the power extracted by the flow.

The near wake region, captured using phase-locked average PIV at different azimuth planes, shows the vortex structures shedding from the blade tips forming helical tip vortices that represent the edge of the wake in the near region. Evidence of wake expansion was also found following an increasing linear trend within the downstream distance considered in this study. No evidence of vortex pairing was found in this work. These results can be used to directly validate CFD and potential-flow simulation codes. The far wake region presents an 80% recovery at the very end of the water tunnel visualization section, that only allows to investigate the wake up to $12R$ downstream.

Chapter 5

Conclusions

Contributions to tidal turbine engineering were accomplished throughout this thesis. The main goal was to re-design and improve the test devices at the SSDL in order to provide reliable experimental results for research purposes. Regarding the specific studies presented here, valuable information was obtained which complements the current available literature.

An enhanced 3D axial rotor rig and 2D Foil test rig are now available for further research in this field. The study presented in chapter 3 developed and validated a method to experimentally obtain hydrofoil performance at low Re using the automated 2D foil test rig, PIV and a proper data reduction method. Moreover, using the experimental results it was found that by adding a trip on the suction side of the foils the overall predictions were greatly improve. This was successfully applied to foils found in literature and also to SSDL-optimized foil shapes, showing good agreement with expected performances based on a mixed viscid-inviscid prediction code.

Subsequently, these results were used as inputs to a BEM code in order to obtain a customized blade design that met structural and performance requirements. The final blade parameters served for experimental rotor performance testing, showing good agreement with CFD and BEM simulations predicting the TSR where C_P is maximized. The study also used PIV to capture tip vortex structures in the near wake region for different azimuth planes. Evidence of wake expansion was found following an increasing linear trend up to $x = 2R$ downstream. No vortex pairing was observed in the results and the tangential vorticity contour plots manifested a slow decrease in magnitude as the vortex moved downstream. The far-wake field was also captured using phase-locked time averaged PIV, showing a velocity deficit of 20% at the end of the observable test section ($x \approx 12R$). The information on wake structure

will significantly contribute in computational validation models, where the obtained results are applicable to both horizontal axis tidal and wind turbines.

Impacts of channel blockage on the rotor rig was compared to that of porous discs and theoretical values, leading to two main conclusions: *(i)* There is an increment in both thrust and power as the blockage ratio increased; *(ii)* the results from the actuator disc theory and porous discs likely represent an upper bound for real rotors, since the overall performance of the axial rotor was less affected compared with the theory and porous discs.

When a free surface is introduced into the experiments and simulations, there are certainly changes in the power extraction as the blockage ratio increases in magnitude. The study was unable to successfully compare experiments with simulations, since different definitions of blockage were employed during the experimental and computational executions, as explained in section 2.6. Experimental results agree with previous studies, where an improvement in performance is observed when free surface effects are present for relatively high blockage ratios. The investigation, however, did not consider different tip clearance distances and it is strongly recommended to follow up on this investigation.

Different foundations on turbine designs can have a significant impact on turbine performance, particularly at high blockage ratios. The monopole foundation showed negligible impact on power extraction compared to actuator disc theory and no foundation setup for the simulated BR range. However, if a different foundation is employed, in this particular case on the side of the rotor plane, the performance is enhanced considerably for high BR. Developing a correction factor to account for foundations is likely not possible due to the large number of foundation types and geometries.

5.1 Future Work

Several different investigation ideas came up after every experimental campaign. The free surface study yielded very valuable results but also new questions to be answered. The discrepancies between the experiments and CFD simulations when free surface effects were considered raised new ideas on how simulations should be oriented to isolate individual contributions. For instance, by running CFD simulations for a turbine in a very deep and wide channel but close to the surface, the blockage can be dismissed. Then running simulations changing the tip immersion distance would

help understanding how C_P is really affected by free surface and how the induced wave upstream behaves and impacts thrust and power. Then blockage effects can be introduced for a proper comparison.

In addition, several new experimental campaigns can be carried out with the fully functional rotor rig. The future rotor performance experiments can use PIV at the rotor plane for a range of TSR to experimentally obtain the axial induction factor, then using Lártiga's correction method [17] the C_P - λ curve can be corrected to unbounded conditions more accurately.

Following up on the rotor rig, a more comprehensive study on tip vortex behaviour can be performed (that was not covered here due to time constraints). For instance, the tip vortex results in the wake region could be expanded to include circulation calculations and also introducing different yaw angles. Moreover, CFD simulations can include different blockage ratios to study how the wake expansion is affected by a constricted channel, comparing near and far wake results to those from experiments to validate results. It would be also very interesting to introduce different turbulent intensities to the experiments, e.g. by using a fractal grid, and compare to previous results as turbulence increases.

Bibliography

- [1] P. M. Cox, R. A. Betts, C. D. Jones, S. A. Spall, and I. J. Totterdell, “Acceleration of global warming due to carbon-cycle feedbacks in a coupled climate model,” *Nature*, vol. 408, no. 6809, pp. 184–187, 2000.
- [2] T. L. Root, J. T. Price, K. R. Hall, S. H. Schneider, C. Rosenzweig, and J. A. Pounds, “Fingerprints of global warming on wild animals and plants,” *Nature*, vol. 421, no. 6918, pp. 57–60, 2003.
- [3] D. L. Hartmann, A. M. Klein Tank, M. Rusticucci, L. V. Alexander, S. Brönnimann, Y. A. R. Charabi, F. J. Dentener, E. J. Dlugokencky, D. R. Easterling, A. Kaplan, *et al.*, “Observations,” in *Cambridge University Press*, 2013.
- [4] R. Pelc and R. M. Fujita, “Renewable energy from the ocean,” *Marine Policy*, vol. 26, no. 6, pp. 471–479, 2002.
- [5] I. Bryden and G. Melville, “Choosing and evaluating sites for tidal current development,” *Proceedings of the Institution of Mechanical Engineers, Part A: Journal of Power and Energy*, vol. 218, no. 8, pp. 567–577, 2004.
- [6] R. Howell, N. Qin, J. Edwards, and N. Durrani, “Wind tunnel and numerical study of a small vertical axis wind turbine,” *Renewable energy*, vol. 35, no. 2, pp. 412–422, 2010.
- [7] H. Hirahara, M. Z. Hossain, M. Kawahashi, and Y. Nonomura, “Testing basic performance of a very small wind turbine designed for multi-purposes,” *Renewable energy*, vol. 30, no. 8, pp. 1279–1297, 2005.
- [8] K. Pope, I. Dincer, and G. Naterer, “Energy and exergy efficiency comparison of horizontal and vertical axis wind turbines,” *Renewable Energy*, vol. 35, no. 9, pp. 2102–2113, 2010.
- [9] S. Eriksson, H. Bernhoff, and M. Leijon, “Evaluation of different turbine concepts for wind power,” *Renewable and Sustainable Energy Reviews*, vol. 12, no. 5, pp. 1419–1434, 2008.
- [10] H. Glauert, *The elements of aerofoil and airscrew theory*. Cambridge University Press, 1983.
- [11] J. N. Sorensen, W. Z. Shen, and R. Mikkelsen, “Wall correction model for wind tunnels with open test section,” *AIAA journal*, vol. 44, no. 8, pp. 1890–1894, 2006.
- [12] A. Bahaj, A. Molland, J. Chaplin, and W. Batten, “Power and thrust measurements of marine current turbines under various hydrodynamic flow conditions in

- a cavitation tunnel and a towing tank,” *Renewable energy*, vol. 32, no. 3, pp. 407–426, 2007.
- [13] C. Lartiga and C. Crawford, “Water tunnel rotor testing with post processing based on piv measurements,” in *ASME 2010 International Mechanical Engineering Congress and Exposition*, American Society of Mechanical Engineers, 2010, pp. 1087–1095.
- [14] J. M. G. J. I. Whelan and J. Peiro, “A free-surface and blockage correction for tidal turbines,” *J. Fluid Mechanics*, vol. 624, pp. 281–291, 2009.
- [15] W. Batten, A. Bahaj, A. Molland, and J. Chaplin, “The prediction of the hydrodynamic performance of marine current turbines,” *Renewable energy*, vol. 33, no. 5, pp. 1085–1096, 2008.
- [16] C. Frid, E. Andonegi, J. Depestele, A. Judd, D. Rihan, S. I. Rogers, and E. Kenchington, “The environmental interactions of tidal and wave energy generation devices,” *Environmental Impact Assessment Review*, vol. 32, no. 1, pp. 133–139, 2012.
- [17] C. Lártiga, “Development of a rig and testing procedures for the experimental investigation of horizontal axis kinetic turbines,” Master’s thesis, University of Victoria, 2009.
- [18] P. Root, “Experimental investigation of airfoil characteristics using particle image velocimetry and potential flow analysis,” Master’s thesis, University of Victoria, 2012.
- [19] T. Nishino and R. H. Willden, “Effects of 3d channel blockage and turbulent wake mixing on the limit of power extraction by tidal turbines,” *International Journal of Heat and Fluid Flow*, vol. 37, pp. 123–135, 2012.
- [20] N. Kolekar and A. Banerjee, “Performance characterization and placement of a marine hydrokinetic turbine in a tidal channel under boundary proximity and blockage effects,” *Applied Energy*, vol. 148, pp. 121–133, 2015.
- [21] N. Marcangeli, “Development validation and use of a code based on momentum and circulation methods,” Master’s thesis, ENSTA Paris and University of Victoria, 2012.
- [22] M. Drela and H. Youngren. (2004). Xfoil: Subsonic airfoil development system, [Online]. Available: <http://web.mit.edu/drela/Public/web/xfoil/>.
- [23] C. Crawford, “Re-examining the precepts of the blade element momentum theory for coning rotors,” *Wind Energy*, vol. 9, no. 5, pp. 457–478, 2006.

- [24] S. McTavish, D. Feszty, and F. Nitzsche, “An experimental and computational assessment of blockage effects on wind turbine wake development,” *Wind Energy*, vol. 17, no. 10, pp. 1515–1529, 2014.
- [25] I. Grant and P. Parkin, “A dpiv study of the trailing vortex elements from the blades of a horizontal axis wind turbine in yaw,” *Experiments in Fluids*, vol. 28, no. 4, pp. 368–376, 2000.
- [26] F. Massouh and I. Dobrev, “Exploration of the vortex wake behind of wind turbine rotor,” in *Journal of Physics: Conference Series*, IOP Publishing, vol. 75, 2007, p. 012 036.
- [27] M. Sherry, J. Sheridan, and D. L. Jacono, “Characterisation of a horizontal axis wind turbine’s tip and root vortices,” *Experiments in fluids*, vol. 54, no. 3, pp. 1–19, 2013.
- [28] M. Drela, “Xfoil: an analysis and design system for low reynolds number airfoils,” *Springer Berlin Heidelberg*, pp. 1–12, 1989.
- [29] MAVI, C. Current, and U. of Victoria, “Impact of channel blockage, free surface proximity and foundations on the performance of tidal and river energy converters,” Tech. Rep., 2014.
- [30] T. Nishino and R. H. Willden, “The efficiency of an array of tidal turbines partially blocking a wide channel,” *J. Fluid Mechanics*, vol. 708, pp. 596–606, 2012.
- [31] I. Franchini, C. Crawford, and M. Shives, “Experimental campaign using a small scale horizontal axis tidal turbine to evaluate rotor performance and tip vortex in the near wake region,” 2016.
- [32] A. R. G. Anthony J. Wheeler, *Introduction to Engineering Experimentation*, Second. Prentice Hall, 2004.
- [33] Klaptocz, V., Wanug, T., Crawford, C., Shives, M., Hiles, C., Walters, R., “Cross-coupling between device-level cfd and oceanographic models applied to tiseas in minas passage and petit passage,” *Offshore Energy Research Association of Nova Scotia*, 2013.
- [34] F. R. Menter, “Two-equation eddy-viscosity turbulence models for engineering applications,” *AIAA journal*, vol. 32, no. 8, pp. 1598–1605, 1994.
- [35] M. Yaras and A. Grosvenor, “Evaluation of one-and two-equation low-re turbulence models. part i axisymmetric separating and swirling flows,” *International journal for numerical methods in fluids*, vol. 42, no. 12, pp. 1293–1319, 2003.

- [36] F. R. Menter, “Review of the shear-stress transport turbulence model experience from an industrial perspective,” *International Journal of Computational Fluid Dynamics*, vol. 23, no. 4, pp. 305–316, 2009.
- [37] R. Mikkelsen, “Actuator disc methods applied to wind turbines,” *Technical University of Denmark, MEK-FM-PHD*, vol. 2, 2003.
- [38] T. Burton, D. Sharpe, N. Jenkins, and E. Bossanyi, *Wind energy handbook*. John Wiley & Sons, 2001.
- [39] L. Myers and A. Bahaj, “Experimental analysis of the flow field around horizontal axis tidal turbines by use of scale mesh disk rotor simulators,” *Ocean Engineering*, vol. 37, no. 2, pp. 218–227, 2010.
- [40] A. Bahaj, L. Myers, R. Rawlinson-Smith, and M. Thomson, “The effect of boundary proximity upon the wake structure of horizontal axis marine current turbines,” *Journal of Offshore Mechanics and Arctic Engineering*, vol. 134, no. 2, p. 021104, 2012.
- [41] S. J. Adamski, “Numerical modeling of the effects of a free surface on the operating characteristics of marine hydrokinetic turbines,” PhD thesis, University of Washington, 2013.
- [42] L. Vermeer, J. N. Sørensen, and A. Crespo, “Wind turbine wake aerodynamics,” *Progress in aerospace sciences*, vol. 39, no. 6, pp. 467–510, 2003.
- [43] M. Harrison, W. Batten, L. Myers, and A. Bahaj, “Comparison between cfd simulations and experiments for predicting the far wake of horizontal axis tidal turbines,” *IET Renewable Power Generation*, vol. 4, no. 6, pp. 613–627, 2010.
- [44] I. H. Abbott, A. E. Von Doenhoff, and L. Stivers Jr, “Summary of airfoil data,” 1945.
- [45] M. S. Selig, *Summary of low speed airfoil data*. SoarTech, 1995, vol. 1.
- [46] D. A. Bourgoyne, C. Q. Judge, J. M. Hamel, S. L. Ceccio, and D. R. Dowling, “Hydrofoil testing at high reynolds number,” *CP, Department of Mechanical Engineering, University of Michigan, Michigan, USA*, 2001.
- [47] C. A. Lyon, *Summary of low-speed airfoil data*. 2001.
- [48] U. of Illinois at Urbana-Champaign (UIUC). Low-speed airfoil test program, [Online]. Available: <http://www.ae.illinois.edu/m-selig/pd.html>.
- [49] P. A. Katz Joseph, *Low-Speed Aerodynamics: From Wing Theory to Panel Methods*. McGraw-Hill, Inc., 1947.
- [50] P. Lissaman, “Low-reynolds-number airfoils,” *Annual Review of Fluid Mechanics*, vol. 15, no. 1, pp. 223–239, 1983.

- [51] A. Gopalarathnam, B. A. Broughton, B. D. McGranahan, and M. S. Selig, “Design of low reynolds number airfoils with trips,” *Journal of aircraft*, vol. 40, no. 4, pp. 768–775, 2003.
- [52] M. Drela and M. B. Giles, “Viscous-inviscid analysis of transonic and low reynolds number airfoils,” *AIAA journal*, vol. 25, no. 10, pp. 1347–1355, 1987.
- [53] D. ”Prosser. (2015). Xoptfoil: Airfoil optimization with xfoil, [Online]. Available: <http://sourceforge.net/projects/xoptfoil/>.
- [54] R. M. Hicks, E. M. Murman, and G. N. Vanderplaats, “An assessment of airfoil design by numerical optimization,” 1974.
- [55] R. M. Hicks and P. A. Henne, “Wing design by numerical optimization,” *Journal of Aircraft*, vol. 15, no. 7, pp. 407–412, 1978.
- [56] E. S. Tashnizi, A. A. Taheri, and M. H. Hekmat, “Investigation of the adjoint method in aerodynamic optimization using various shape parameterization techniques,” *Journal of the Brazilian Society of Mechanical Sciences and Engineering*, vol. 32, no. 2, pp. 176–186, 2010.
- [57] D. Ragni, A. Ashok, B. Van Oudheusden, and F. Scarano, “Surface pressure and aerodynamic loads determination of a transonic airfoil based on particle image velocimetry,” *Measurement Science and technology*, vol. 20, no. 7, p. 074 005, 2009.
- [58] J. J. Charonko, C. V. King, B. L. Smith, and P. P. Vlachos, “Assessment of pressure field calculations from particle image velocimetry measurements,” *Measurement Science and technology*, vol. 21, no. 10, p. 105 401, 2010.
- [59] T. Baur and J. Köngeter, “Piv with high temporal resolution for the determination of local pressure reductions from coherent turbulence phenomena,” in *International Workshop on PIV’99- Santa Barbara, 3 rd, Santa Barbara, CA*, 1999, pp. 101–106.
- [60] B. W. van Oudheusden, F. Scarano, E. W. Roosenboom, E. W. Casimiri, and L. J. Souverein, “Evaluation of integral forces and pressure fields from planar velocimetry data for incompressible and compressible flows,” *Experiments in Fluids*, vol. 43, no. 2-3, pp. 153–162, 2007.
- [61] E. Houghton and P. Carpenter, *Aerodynamics for Engineering Students*, Fourth. Edward Arnold, 1993, pp. 380–383.
- [62] M. Drela, “Implicit implementation of the full e^n transition criterion,” 2003.

- [63] A. Arena and T. Mueller, “Laminar separation, transition, and turbulent reattachment near the leading edge of airfoils,” *AIAA journal*, vol. 18, no. 7, pp. 747–753, 1980.
- [64] S. Srigrarom, D.-B. Wang, and Y.-H. Lim, “Classification of airfoils by abnormal behavior of lift curves at low reynolds number,” in *APS Division of Fluid Dynamics Meeting Abstracts*, 2005.
- [65] S. McTavish, D. Feszty, and F. Nitzsche, “Evaluating reynolds number effects in small-scale wind turbine experiments,” *Journal of Wind Engineering and Industrial Aerodynamics*, vol. 120, pp. 81–90, 2013.
- [66] W. Haans, T. Sant, G. van Kuik, and G. van Bussel, “Measurement of tip vortex paths in the wake of a hawt under yawed flow conditions,” *Journal of Solar Energy Engineering*, vol. 127, no. 4, pp. 456–463, 2005.
- [67] S. McTavish, “Identification of wind turbine testing practices and investigation of the performance benefits of closely-spaced lateral wind farm configurations,” PhD thesis, Carleton University Ottawa, 2013.
- [68] L. P. Chamorro, R. Arndt, and F. Sotiropoulos, “Reynolds number dependence of turbulence statistics in the wake of wind turbines,” *Wind Energy*, vol. 15, no. 5, pp. 733–742, 2012.
- [69] I. Franchini, C. Crawford, and M. Shives, “Obtaining experimental aerodynamic coefficients using a 2d airoil test rig in a recirculating flume tank,” 2016.
- [70] R. J. Adrian and J. Westerweel, *Particle image velocimetry*, 30. Cambridge University Press, 2011.
- [71] LaVision, *Davis 7.2*, version 7.2.2.474, Sep. 1, 2010.
- [72] W. J. Devenport, M. C. Rife, S. I. Liapis, and G. J. Follin, “The structure and development of a wing-tip vortex,” *Journal of Fluid Mechanics*, vol. 312, pp. 67–106, 1996.

Appendix A

Appendices

A.1 Rotor rig modifications

A large amount of work done during this study was dedicated to re-design and improvement of the existent rotor rig. Main modifications are listed below:

- Stepper motor replaced for an AKM23D servomotor (figure [A.1](#))
- Re-design top structure to fit new motor. Special concern was taking regarding shear load on the torque cell due to the new motor configuration ([A.1](#))
- Important new hub assembly design, allowing a reliable performance for fixed pitch angle of the blades (figure [A.2](#))
- New set of blades, which is explained in detail in chapters [3](#) and [4](#)
- Final rotor rig design, shown in figure [A.3](#)

A.2 Instrumentation Modifications

Motor Controller modifications and DAQ:

- NI cRIO RT controller with modules NI 9512 and NI 9237 + New NI 9514 in communication with AKD servo drive (figure [A.5](#))

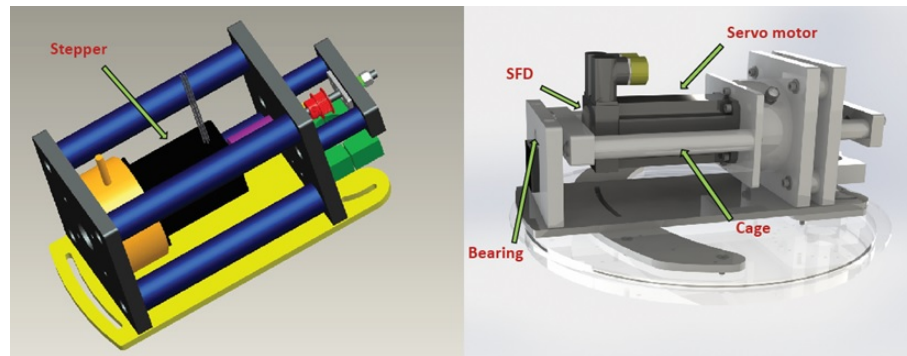


Figure A.1: Top assembly modifications. Original design (left) and new design (right)

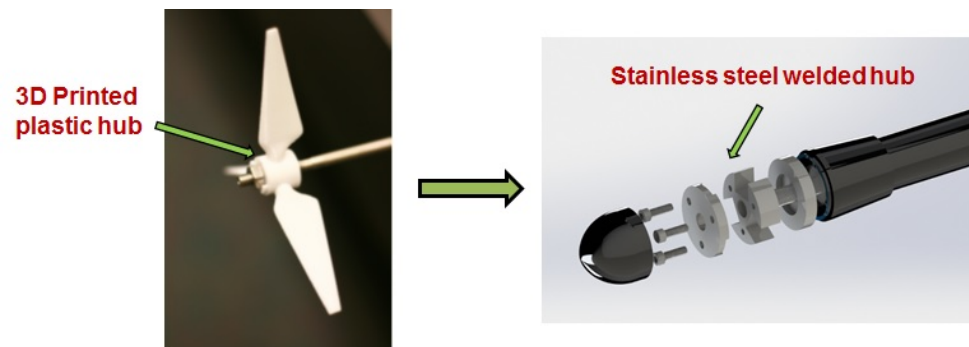


Figure A.2: Hub modifications. Original design (left) and new stainless steel welded hub design (right)

- Software implementation for Rotor Rig that allows speed control, torque data acquisition and triggering PIV system at any desired azimuthal angle of the blades. (figure [A.6](#))
- New software allows the user to control stepper position for 2D Airfoil test (figure [A.7](#))
- Additional software compliment to allow vortex capture using a linear actuator for camera position

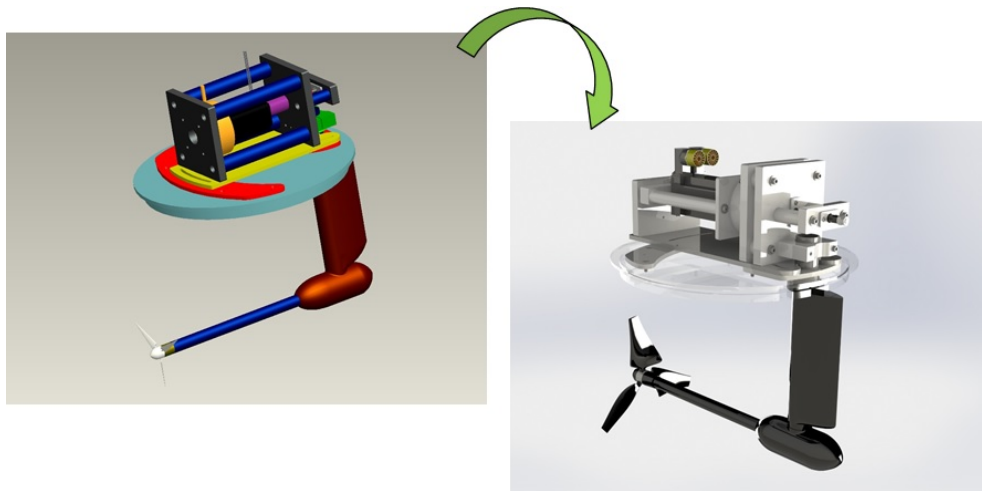


Figure A.3: Original axial rotor design (left) and full rotor rig new appearance (right)

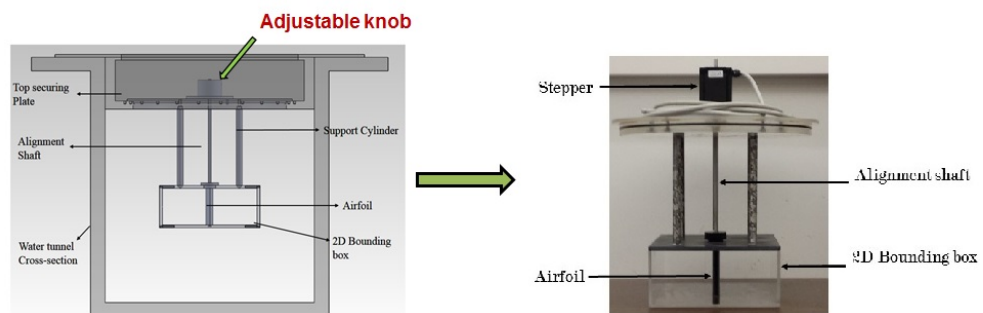


Figure A.4: Original 2D Hydrofoil test rig (left) and new design (right)

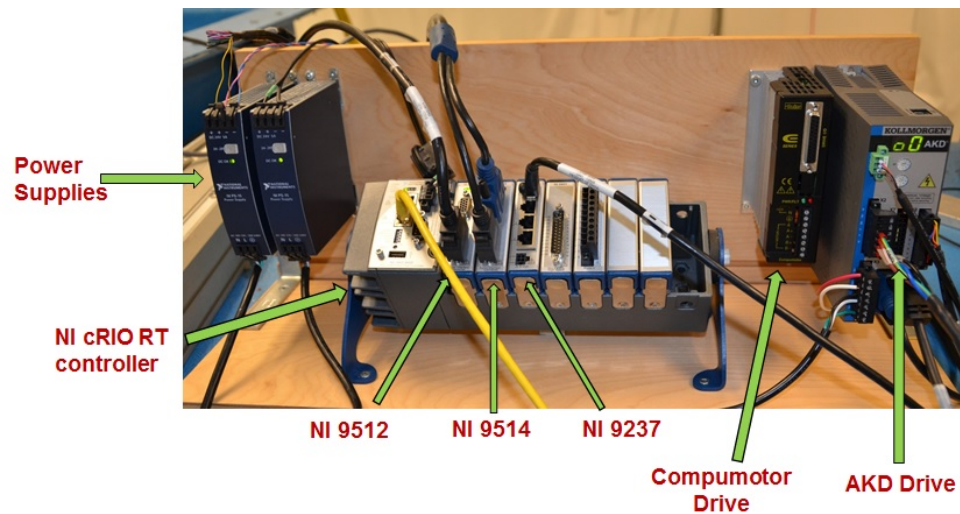


Figure A.5: New instrumentation panel appearance

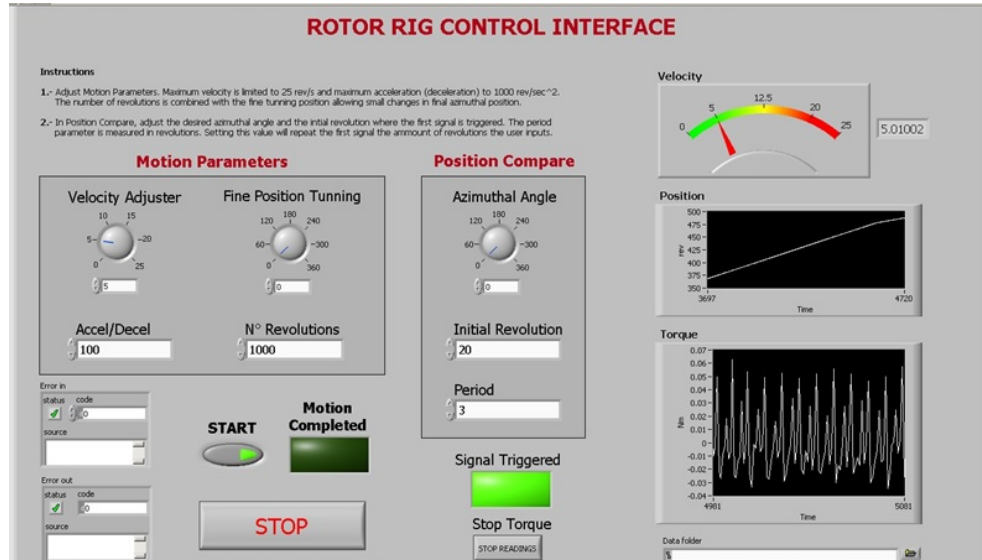


Figure A.6: Rotor rig control interface developed in LabView 2012

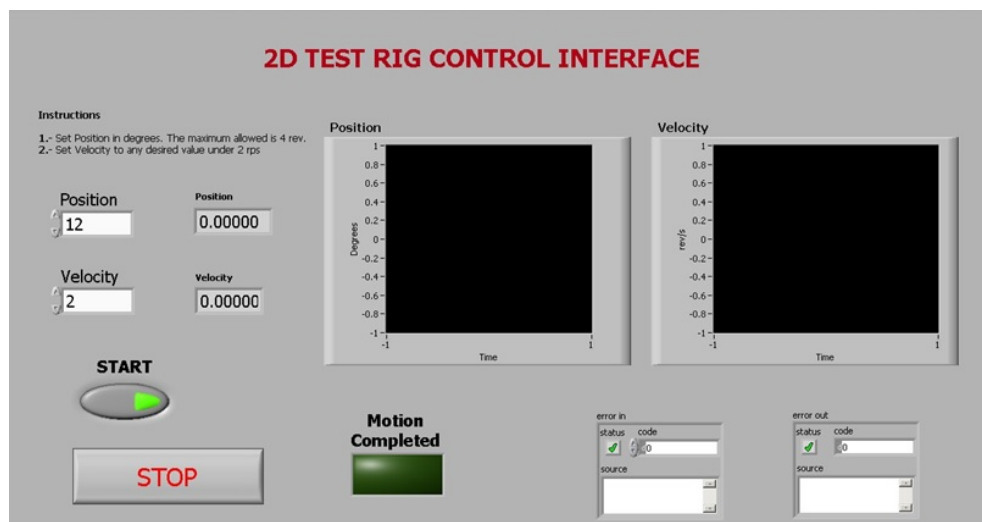


Figure A.7: 2D Hydrofoil test rig control interface developed in LabView 2012